EFFECTS OF ELECTRON EMISSION ON PLASMA SHEATHS

A Dissertation
Presented to
The Academic Faculty

by

Samuel Langendorf

In Partial Fulfillment
of the Requirements for the Degree
Doctor of Philosophy in the
Daniel Guggenheim School of Aerospace Engineering

Georgia Institute of Technology
December 2015

EFFECTS OF ELECTRON EMISSION ON PLASMA SHEATHS

Approved by:

Professor Mitchell L. R. Walker II,
Advisor
Daniel Guggenheim School of
Aerospace Engineering
Georgia Institute of Technology

Professor Carol Paty
School of Earth and Atmospheric
Sciences
Georgia Institute of Technology

Professor Wenting Sun
Daniel Guggenheim School of
Aerospace Engineering
Georgia Institute of Technology

Professor Michael Keidar
Department of Mechanical and
Aerospace Engineering
The George Washington University

Professor Suresh Menon
Daniel Guggenheim School of
Aerospace Engineering
Georgia Institute of Technology

Date Approved: August 19th, 2015

ACKNOWLEDGEMENTS

To future graduate students who have somehow found this document and are taking time to read the acknowledgments, I apologize in advance for the unnecessary explanations, omissions of critical information, and general confusion that you will doubtless encounter within. I tried to make it as good a read as I could, but what would grad school be without some mystery and frustration as you page through literature. Keep your head up! When you get to the end of the degree, you'll be happy and proud... or at least, it'll all be over and you can go out and make some money.

I want to take a decent amount of the acknowledgment real estate to say thank you to my advisor, Dr. Mitchell Walker. Thank you for introducing me to the fascinating world of EP research, finding funding for me for all these years, giving me time and freedom when I needed it, and guidance and a dose of reality when I needed that too. I don't know how you keep up with all of the demands they are putting on research professors these days (honestly I feel like it's like three jobs rolled into one,) but you always made time to meet with us students.

I would also like to thank my thesis committee, Dr. Suresh Menon, Dr. Wenting Sun, Dr. Carol Paty and Dr. Michael Keidar, thank you for taking time out of your equally busy schedules to listen to my presentations. I'd like to thank the other members of our collaborative research group. Dr. Thompson and Thomas Burton from University of Alabama, thank you for helping me (eventually) understand the importance of the surface and for procuring and preparing samples over the years. Dr. Ready and Dr. Wagner, at GTRI and Aaron Schinder of HPEPL, thank you for assisting with profilometry of wall material samples and getting me trained up on the SEM. To Dr. Keidar, Dr. Brieda, Dr. Schweigert, and Laura Rose at GWU,

thank you for your helpful correspondence and peerless plasma simulations. Taking care of the bottom line, I would like to thank Dr. Mitat Birkan at the Air Force Office of Scientific Research, for green-lighting the funding for this work through Grant FA9550-11-10160 throughout my years at Georgia Tech. I imagine it is not easy to invest in basic research like this – here's hoping this all leads to the next big breakthrough.

I want to thank and give some shout-outs to my friends at HPEPL. I always joked about how grad school was awesome and I never wanted to leave... well, that was true, and it was because of the wonderful companionship and friendship I found with you all throughout our time here. Logan and Gabe, thank you for your leadership of the lab and bringing us all together to play Diablo II, Mafia, and form a community that brought us such happiness. Alex, I could not keep up with your gigantic steps but thank you for writing such a useful paper about the LN2 system. Scott, thank you for your easygoing attitude and friendship – your intelligence and attention to detail showed me what it takes to engineer something that will really work. Lake, thank you for teaching me about vacuum technology on the Bell Jars, showing me the ins and outs of Dragon-Con, and opening my mind to the world of entrepreneurship (and look at you now, workin' for the man!) Cristian, thank you for fixing all of the things. Gabi, you are too good at Mafia, and I won't forget our epic adventure rocking out and calculating with license plate numbers on that 18-hour drive to Boston. Sebastiano, you showed me how to move heaven and earth to get your research done – thank you for taking mercy on me when I was delirious from quals-studying. Rafael, you introduced me to the joys of anodes when I was a wee first-year grad student – I've gotten to see some center-mount cathodes now and I have to hand it to you, they're pretty cool. Hoang, you taught me LabView, electronics, and how to climb around vacuum chambers – the conical beam dump is still standing proudly as a testament to your unmatched gifts to the lab. Aaron, I'll miss our discussions of quantum mechanics

and dystopian sci-fi universes, thank you for your friendship and challenging me to understand the world better. Jon, thank you for introducing me to the big-boy world of engineering and research with the MPD project – and keeping us from killing ourselves on the pulsed power! Jason, thank you for dragging CR2 into the 21st century (kicking and screaming) – I'm confident that the lab is in good hands with you in the upcoming years. Tom, thank you for your wisdom and experience in dealing with all things vacuum and plasma, and for a dose of professionalism amongst us ramblin' wrecks. Cheong, Tyler, and Connie, thanks for injecting some much-needed new blood and youthful enthusiasm into our group. I hope we haven't left you too many nasty surprises... And Natalie, thank you for going through the mess that is grad school with me and refraining from strangling me on account of my admittedly unreasonable optimism. The Lab sitcom has some gems that I won't forget (perhaps my favorite one is the saga of the bees or maybe Dr. Walker's infamous double-down moment!) and it has been a privilege to work with you for these years.

I would be remiss if I did not extend thanks to the undergrads, the unsung heroes of the lab. Those who got the fun independent research projects, and those who did the dirty jobs that even we grad students didn't want to tackle. Particularly Chase, Louis, Adam, Filipe, Mike, Marcellus, Martin, Matt, Shadrach, Jack, Phoebe, and Nathan, as well as all those I didn't work with directly. I'd also like to thank the aerospace admin group, for your support and assistance over the years.

I thank my parents, Sarah and Henry Langendorf, for the incredible gift of time, money and love you have given me, in raising me for two decades, paying for my college, and humoring my recent scholarly diversions. I love you both very much, and wherever I go in life I will always remember your love and light.

And most of all, thank you to my wonderful wife, Brenna. For putting up with me through these years of low income, intermittent surliness, late nights testing at the lab, the times when the chiller would call me at 2 A.M. You supported me through

everything while getting a Master's and holding a real job. I could never have gotten through it all without you. I love you very much, and I hope the future will only get brighter for us from here on out.

TABLE OF CONTENTS

LIST OF TABLES

LIST OF FIGURES

List of Acronyms

Symbol	Description
AEHF-1	Advanced Extremely High Frequency-1
BN	boron nitride
CL	Child-Langmuir
DC	direct current
DFT	discrete Fourier transform
EEDF	electron energy distribution function
EP	electric propulsion
GEO	Geosynchronous Earth Orbit
GT	Georgia Institute of Technology
GTRI	Georgia Tech Research Institute
GWU	The George Washington University
H&W	Hobbs and Wesson
HET	Hall effect thruster
IEDF	ion energy distribution function
LCIF	Laser-collisional-induced fluorescence
LEEM	low energy electron microscopy
LIF	Laser-induced fluorescence
MCC	Monte Carlo collisions
MPD	Magnetoplasmadynamic
NPLC	number of power line cycles
OML	orbital-motion-limited
PIC	particle-in-cell
RF	radio-frequency

Symbol	Description
SEE	secondary electron emission
UA	University of Alabama
US	United States
VDF	velocity distribution function
XIPS	Xenon Ion Propulsion System

Greek Symbols

Symbol	Description	Dimensions	Units
ΔV	Delta-V, propulsion requirement metric	L T^{-1}	m s^{-1}
λ_D	Debye length	L	m
λ_d	electron Debye length	L	m
ϵ_0	permittivity of free space	T^4 I^2 M^{-1} L^{-3}	F m^{-1}
ϕ	electrical potential	M L^2 I^{-1} T^{-3}	V
ϕ_p	plasma potential	M L^2 I^{-1} T^{-3}	V
Γ	particle flux	L^{-2} T^{-1}	m^{-2} s^{-1}
ν_c	collision frequency	T^{-1}	s^{-1}
ρ	charge density	I T L^{-3}	C m^{-3}
Ω	gyrofrequency	T^{-1}	s^{-1}
ω_{pe}	electron plasma frequency	T^{-1}	s^{-1}
ω_{pi}	ion plasma frequency	T^{-1}	s^{-1}

Roman Symbols

Symbol	Description	Dimensions	Units
A	area	L^2	m^2
A_G	material Richardson constant	$\mathrm{I\ L^{-2}\ \Theta^{-2}}$	eV
B	magnetic field	$\mathrm{M\ I^{-1}\ T^{-2}}$	T
d	sheath thickness	L	m
$\vec{E}$	electric field	$\mathrm{M\ L\ I^{-1}\ T^{-3}}$	$\mathrm{V\ m^{-1}}$
E	energy	$\mathrm{M\ L^2\ T^{-2}}$	J
F	view factor	-	-
f	distribution function	$\mathrm{T\ L^{-1}}$	$\mathrm{s\ m^{-1}}$
$\vec{F}_\mathrm{L}$	Lorentz force	$\mathrm{M\ L\ T^{-2}}$	N
g_0	Earth standard acceleration of gravity	$\mathrm{L\ T^{-2}}$	$\mathrm{m\ s^{-2}}$
h	height (groove)	L	m
I	current	I	A
I_D	discharge current	I	A
I_H	heating current	I	A
I_sp	specific impulse	T	s
J	current density	$\mathrm{I\ L^{-3}}$	$\mathrm{A\ m^{-3}}$
k_B	Boltzmann constant	$\mathrm{M\ L^2\ T^{-2}\Theta^{-1}}$	$\mathrm{J\ K^{-1}}$
L	length scale of system	L	m
$\dot{m}$	mass flow rate	$\mathrm{M\ T^{-1}}$	$\mathrm{kg\ s^{-1}}$
m_0	Pre-burn mass of rocket	M	kg
m_1	Post-burn mass of rocket	M	kg
m	mass	M	kg
n	number density	$\mathrm{L^{-3}}$	$\mathrm{m^{-3}}$

Symbol	Description	Dimensions	Units
Q	collisional integral	L^{-3}	m^{-3}
q	charqe of a particle	I T	A s
r	1D radial spatial coordinate	L	m
s	spacing (groove center-to-center)	L	m
T	thrust	M	kg
t	time	T	s
T	temperature	$\mathrm{M\ L^2\ T^{-2}}$	eV
u	velocity of a particle	$\mathrm{L\ T^{-1}}$	$\mathrm{m\ s^{-1}}$
u_{eff}	effective exhaust velocity	$\mathrm{L\ T^{-1}}$	$\mathrm{m\ s^{-1}}$
V	voltage	$\mathrm{M\ L^2\ I^{-1}\ T^{-3}}$	V
V_{D}	discharge voltage	$\mathrm{M\ L^2\ I^{-1}\ T^{-3}}$	V
V_{H}	heating voltage	$\mathrm{M\ L^2\ I^{-1}\ T^{-3}}$	V
W	work function	$\mathrm{M\ L^2\ T^{-2}}$	eV
w	width (groove)	L	m
x	1D planar spatial coordinate	L	m
Z	charge state	-	-

Subscripts

Symbol	Description
0	sheath edge
α	index over different plasma species
B	bottom (of groove)
c	critical
CL	Child-Langmuir
cp	cold plasma (electrons)
E	entrance / exit (of groove)
e	electrons
ee	emitted electrons
ei	isotropic energetic electrons
ep	plasma electrons
f	floating
hp	hot plasma (electrons)
i	ions
n	neutral molecules
p	plasma
ps	presheath
S	side (of groove)
w	wall

Dimensionless Numbers

Symbol	Description	Definition
α	energetic electron fraction	$\frac{n_{\mathrm{ei0}}}{n_{\mathrm{ep0}} + n_{\mathrm{ei0}}}$
α_{ps}	reduction in plasma density across presheath	$\frac{n_0}{n_{\mathrm{p}}}$
AR	aspect ratio (grooves)	$\frac{h}{w}$
C_1	constant in Child-Langmuir sheath	$\frac{\Phi(\xi)}{\xi^{\frac{4}{3}}} = \left(\frac{81}{32}\right)^{\frac{1}{3}} {\alpha_{\mathrm{ps}}}^{\frac{2}{3}}$
C_2	constant in Child-Langmuir sheath	$\frac{\xi(\Phi)}{\Phi^{\frac{3}{4}}} = \left(\frac{81}{32}\right)^{-\frac{1}{4}} {\alpha_{\mathrm{ps}}}^{-\frac{1}{2}}$
δ	energy flux	$\epsilon\Xi$
ϵ	energy	$\frac{E}{eT_{\mathrm{e}}}$
Φ	potential	$-\frac{e\phi}{k_{\mathrm{B}}T_{\mathrm{e}}}$
γ	electron yield	$\frac{\Gamma_{\mathrm{ee}}}{\Gamma_{\mathrm{ew}}}$
Θ	plasma / emitted T_{e} ratio	$\frac{T_{\mathrm{ep}}}{T_{\mathrm{ee}}}$
μ	ion / electron mass ratio	$\frac{m_{\mathrm{i}}}{m_{\mathrm{e}}}$
N	number density	$\frac{n}{n_0}$
N_{d}	number of particles in Debye sphere	$\frac{4}{3}\pi {\lambda_{\mathrm{D}}}^3$
Ξ	particle flux	$\frac{\Gamma}{\frac{1}{4}n_{\mathrm{e}}u_{\mathrm{e}}}$

Symbol	Description	Definition
SR	spacing ratio (grooves)	$\frac{w}{s}$
U	speed	$\frac{u}{u_\mathrm{B}} = \frac{u}{\sqrt{\frac{k_\mathrm{B} T_\mathrm{e}}{m_\mathrm{i}}}}$
ξ	distance	$\frac{x}{\lambda_\mathrm{D}}$

SUMMARY

Current state-of-the-art plasma thrusters are limited in power density and thrust density by power losses to plasma-facing walls and electrodes. In the case of Hall effect thrusters, power deposition to the discharge channel walls and anode negatively impact the efficiency of the thruster and limit the attainable power density and thrust density. The current work aims to recreate thruster-relevant wall-interaction physics in a quiescent plasma and investigate them using electrostatic probes, in order to inform the development of the next generation of high-power-density / high-thrust-density propulsion devices.

Thruster plasma-wall interactions are complicated by the occurrence of the plasma sheath, a thin boundary layer that forms between a plasma and its bounding wall where electrostatic forces dominate. Sheaths have been recognized since the seminal work of Langmuir in the early 1900's, and the theory of sheaths has been greatly developed to the present day. The theories are scalable across a wide range of plasma parameters, but due to the difficulty of obtaining experimental measurements of plasma properties in the sheath region, there is little experimental data available to directly support the theoretical development.

Sheaths are difficult to measure in situ in thrusters due to the small physical length scale of the sheath (order of micrometers in thruster plasmas) and the harsh plasma environment of the thruster. Any sufficiently small probe will melt, and available optical plasma diagnostics do not have the sensitivity and/or spatial resolution to resolve the sheath region.

The goal of the current work is to experimentally characterize plasma sheaths

in a low-density plasma that yields centimeter-thick sheath layers. By generating thick sheaths, spatially-resolved data can obtained using electrostatic probes. The investigation focuses on the effects of electron emission from the wall and several factors that influence it, including wall material, wall temperature, wall surface roughness and topology, as well as the scaling of sheaths from the low-density plasma environment towards thruster conditions.

The effects of electron emission and wall material are found to agree with classical fluid and kinetic theory extended from literature. In conditions of very strong emission from the wall, evidence is found for a full transition in sheath polarities rather than a non-monotonic structure. Wall temperature is observed to have no effect on the sheath over boron nitride walls independent of outgassing on initial heat-up, for sub-thermionic temperatures. Wall roughness is observed to postpone the effects of electron emission to higher plasma temperatures, indicating that the rough wall impairs the wall's overall capacity to emit electrons. Reductions in electron yield are not inconsistent with a diffuse-emission geometric trapping model. Collectively, the experimental data provide an improved grounding for thruster modeling and design.

CHAPTER I

INTRODUCTION

One of the difficulties of mankind's quest to expand beyond the planet Earth is the challenge of moving from point A to point B in space, which is the engineering problem of space propulsion. The absence of appreciable amounts of ambient matter in interplanetary space means that airbreathing methods of propulsion used on earth do not work. The most successful technology that we have used so far is the rocket, which produces thrust by ejecting a working mass from the spacecraft in the opposite direction from the desired acceleration. Simply put, rocket propulsion is a straightforward application of Newton's third law: "every action has an equal and opposite reaction."

The central difficulty in rocket propulsion for space travel is the need to carry the necessary reaction mass along with the spacecraft for the duration of the intended trip. This means that the mass of the rocket grows exponentially with the amount of propulsion required. The difficulty is seen in the Tsiolkovsky ideal rocket equation:

$$m_0 = m_1 \exp\left(\frac{\Delta V}{u_{\text{eff}}}\right) \tag{1.1}$$

where m_0 is the pre-burn mass of the rocket, m_1 is the post-burn mass, and the amount of propulsion required is quantified by ΔV. ΔV is a scalar quantity with units of speed, and is defined as the integral over the burn time of the thrust divided by the mass. In the absence of external forces, this is equal to the resulting change in speed of the vehicle. The required orbital speed to maintain low earth orbit is 7800 m/s, and losses due to drag, gravity and thrust vector alignment increase the needed ΔV to 9300 - 10000 m/s.

The effective exhaust velocity u_{eff} is the only other quantity besides ΔV present inside the exponential function in the rocket equation (1.1). It is the exhaust velocity

such that the thrust T can be related to the mass flow rate $\dot{m}$ by

$$T = \dot{m} u_{\text{eff}}. \tag{1.2}$$

u_{eff} may in general differ from the actual speed of the rocket exhaust if pressure or divergence effects are significant.

The effective exhaust velocity is often expressed as the specific impulse, which is the effective exhaust velocity divided by Earth's standard acceleration of gravity g_0:

$$I_{\text{sp}} = \frac{u_{\text{eff}}}{g_0} \tag{1.3}$$

I_{sp} is measured in units of seconds. Figure 1.1 shows the dependence of the required mass ratio on ΔV requirement for a given propulsion system I_{sp}.

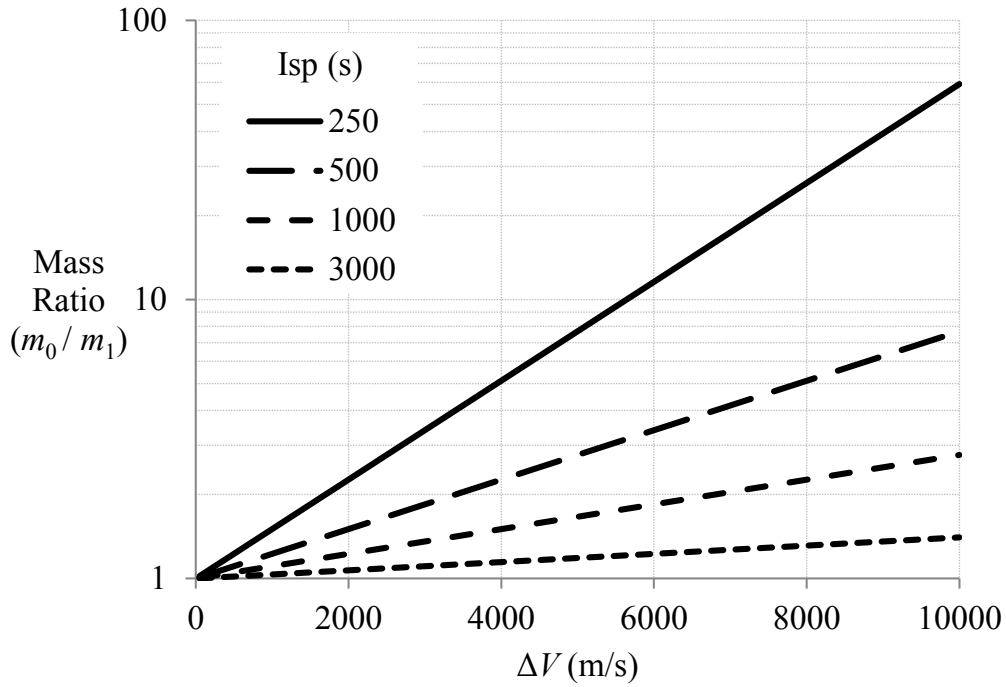

Figure 1.1: Ideal rocket equation, relation between propulsion system specific impulse and mass ratio / propellant mass required to perform a maneuver of given ΔV.

The maximum exhaust speed of a chemical rocket using known fuels is about 4,500 m/s. This means that the initial mass of a (one-stage) rocket departing earth must be at minimum approximately $\exp(10000/4500) = 9.2$ times greater than the mass of

the final spacecraft, close to the limit of what can be attained subject to engineering material limitations. Consequently, a single-stage-to-orbit rocket has remained beyond our capability. The exponential growth of mass ratio with ΔV is the "tyranny of the rocket equation" – for this reason, mass is at a premium on a rocket-propelled spacecraft.

The advantage of chemical rockets is that they have an abundance of energy available from the reacting fuel, and thus can produce tremendous power and thrust. Chemical rockets have been successfully used to launch exploratory craft and human astronauts beyond Earth's atmosphere. They are likely to remain the only method for doing so until unforeseen breakthroughs are achieved.

1.1 Electric Rocket Propulsion

Once orbit is attained, the urgency to apply thrust and overcome gravity present in the launch phase is decreased. In neglect of factors such as drag that cause low orbits to decay, the total energy of an orbiting object will remain constant. New possibilities indicated by the rocket equation become viable, namely, if the exhaust velocity of the rocket working mass can be increased, the amount of propellant needed for in-space maneuvering decays exponentially. This is the idea behind electric propulsion (electric propulsion (EP)) devices for spacecraft.

EP devices generate an ionized gas to use as a working fluid, which allows the user to add energy directly to the propellant ions by means of applied electric fields. EP devices can achieve very high exhaust velocities on the order of 10,000 - 50,000 m/s, which enables high ΔV maneuvers with minimal propellant expenditure. EP systems typically operate between 500 and 5,000 seconds I_{sp}, while chemical rockets operate from 150 - 450 seconds.

The downside of electric propulsion is the need to derive and supply the external power to the device. In contrast to chemical rockets, which have an abundant amount

of power available from combustion, EP devices must supply that power from an onboard power supply. Historically this has been photovoltaic panels capturing power radiated from the sun, but any power source could be used in principle. The total power supplied is low in comparison to chemical rockets – the Saturn V first stage liberated ~160 GW of power while firing, while the largest solar array in space to date (on the International Space Station) generates "only" ~100 kW [2].

The high exhaust velocity and low available power for EP devices mean that they are currently limited to only accelerating a relatively small number of particles at a time compared to a chemical rocket. This means that they produce a low thrust, typically on the order of 10's to 100's of mN. This level of thrust is similar to the weight of a sheet of paper. Consequently, EP systems are only useful in space; in the launch phase, the thrust would be insignificant compared to the vehicle's weight (or even the thruster's weight.) On orbit however, the thrust can be fired for months on end and a large net impulse can be delivered to the spacecraft.

1.1.1 Types of Electric Propulsion Devices

Many types of electric propulsion devices have been developed [48]. They can be categorized by the nature of their acceleration scheme, into categories of electrothermal, electrostatic, and electromagnetic thrusters.

Electrothermal EP

An electrothermal EP device uses input electrical power to heat the propellant gas and subsequently converts the thermal energy of the gas to directed kinetic energy by expanding / ejecting the heated exhaust. These thrusters often employ light propellant gases such as hydrogen or helium in order to boost the exhaust velocity and specific impulse attained for a given propellant temperature. Examples of this class of EP devices include resistojets [30], which heat the gas by contact with a heating element,

and arcjets [64], which heat the gas by sustaining an electrical arc discharge in the exhaust.

Electrostatic EP

Electrostatic EP devices accelerate charged particles directly using applied electric fields. The force on a charged particle in electric and magnetic fields is the Lorentz force $\vec{F_{\mathrm{L}}}$

$$\vec{F_{\mathrm{L}}} = q\left(\vec{E} + \vec{u} \times \vec{B}\right) \tag{1.4}$$

in which q and $\vec{u}$ are the charge and velocity of the particle and $\vec{E}$ and $\vec{B}$ are the electric and magnetic fields present at the particle's location. Electrostatic EP devices use the electric component of the Lorentz force, the first term in equation (1.4).

As will be discussed, plasmas act to screen out applied electric fields, so this type of acceleration is typically only effective in a near-wall sheath region. The classical example of this type of EP device is the gridded ion engine, which uses an applied electric field between closely-spaced accelerator grids to eject charged particles from the thruster.

Gridded Ion Engine The gridded ion engine consists of a self-contained plasma chamber bounded on one side by multiple accelerator grids and an external neutralizer cathode [100]. A diagram and photo of a gridded ion engine is shown in Figure 1.2. Plasma is generated in the chamber by injecting power in some way, such as by a direct current (DC) discharge or radio-frequency (RF) antenna. The grids are electrically biased to create an electric field between them, and ions that approach the grids are accelerated away from the vehicle to produce thrust. Only positively charged species are extracted by the grids, so an external neutralizer cathode supplies electrons to neutralize the exhaust plume and keep the spacecraft from charging. The most intimidating problem limiting the thrust density of ion engines is the very fact that

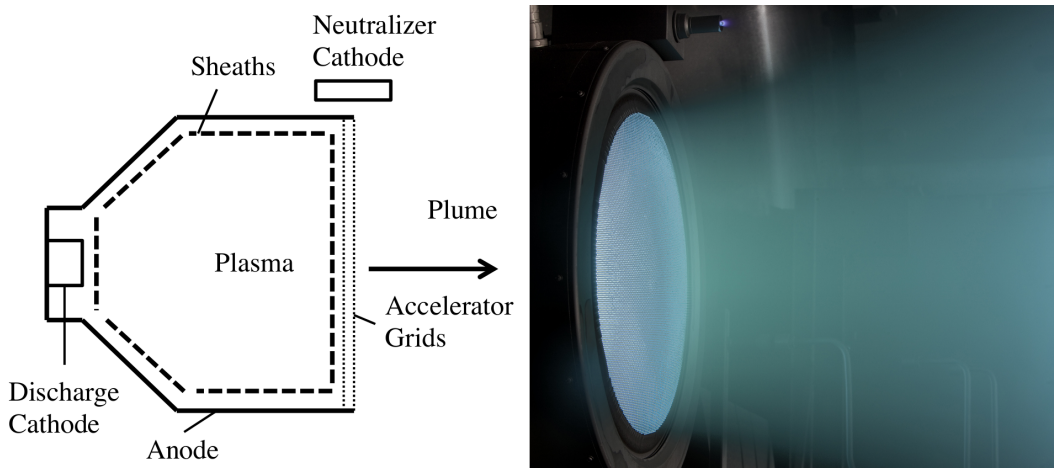

Figure 1.2: Simplified schematic and photo of DC discharge gridded ion engine. Internal magnetic field not shown. Photo credit: NASA GRC.

the ion engine accelerates a beam of positively charged ions through the grids: if there are enough ions, their mutual electrostatic repulsion acts to cancel the accelerating field of the grids. This is referred to as the "space charge limit" and represents a physical maximum to the thrust density achievable by an ion engine.

Electromagnetic EP

Electromagnetic EP devices employ the $\vec{u} \times \vec{B}$ component of the Lorentz force, the second term in equation (1.4). A pure example of this type of thruster is the Magnetoplasmadynamic (MPD) thruster, wherein a radial arc generates an azimuthal magnetic field and an axial magnetic Lorentz force on charged particles within the thruster plasma. MPD thrusters are a promising high-power architecture offering extremely high power densities [56], but are currently limited by the onset of discharge voltage oscillations and rapid erosion of the plasma-facing electrodes [57] [8].

Hall Effect Thruster The Hall effect thruster (HET) uses a magnetic field to trap electrons in a closed azimuthal $\vec{E} \times \vec{B}$ drift, thus increasing the plasma density and concentrating the electric field of a DC discharge [104]. HET's accelerate ions within an electrically neutral plasma region containing both ions and electrons and

the thrust density is not limited by space charge. Wall interactions are responsible for power losses in HET's and may also contribute to anomalously high levels of electron transport to the thruster anode [69], both of which decrease the attainable plasma density. A diagram and photo of a Hall effect thruster is shown in Figure 1.3.

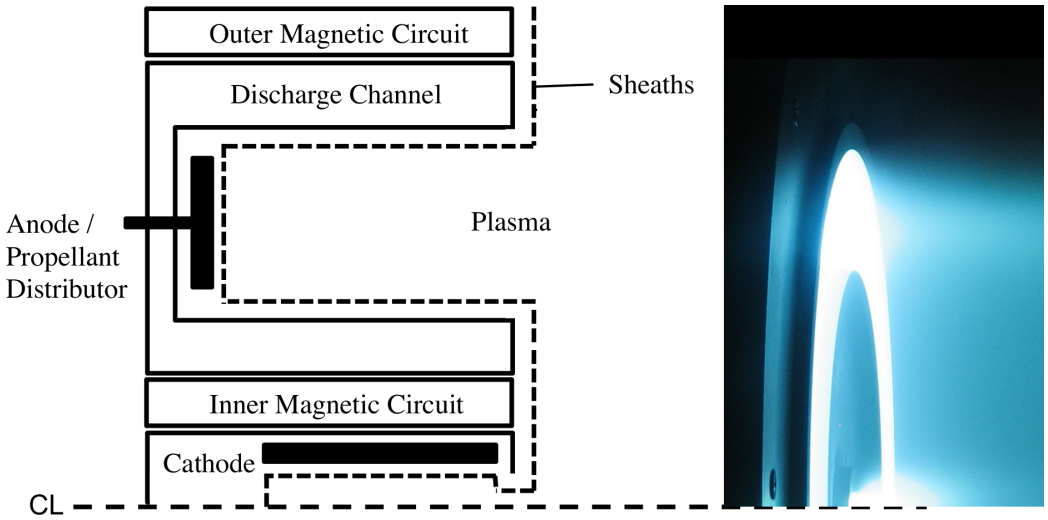

Figure 1.3: Simplified schematic and photo of Hall effect thruster cross section, shown with center-mounted cathode. Magnetic field not shown. Photo credit: NASA JPL.

The Hall effect thruster may be considered an electromagnetic thruster, since the force imparted to the ion exhaust is magnetically coupled back to the thruster magnetic circuit, however it could also be characterized as electrostatic since the electric field in the plasma is responsible for the acceleration of the ions.

1.1.2 Applications of Electric Propulsion

The classical application for EP devices has been for stationkeeping, which is to supply propulsion as needed to maintain a satellite's desired orbital parameters. In this application, the propulsion systems counteracts drags on the orbit of the satellite due to atmospheric drag, solar wind, and solar radiation pressure. Since these drags are typically not large forces, the low thrust of EP systems is not a problem, and the high specific impulse of EP systems means that this task can be accomplished with

minimal propellant expenditure. A consistent market (around 20 satellites per year [16]) has been commercial geosynchronous-class communications satellites, which have decade-long mission durations and carry kilowatts of onboard power with which to run electric thrusters. EP systems have also been successfully used for robotic deep-space exploration missions such as NASA's Deep Space 1 [75] and Dawn [14] missions.

Recently, a crisis-driven application of an EP system highlighted the technology's ability to perform more ambitious maneuvers in Earth's sphere of influence than solely stationkeeping. In 2010, the Advanced Extremely High Frequency-1 (AEHF-1) satellite suffered a failure of the bipropellant chemical rocket motor that was to circularize the satellite orbit. The decision was made to deploy the spacecraft solar panels earlier than planned and use an onboard electric thruster to raise and circularize the orbit. The plan worked, and the spacecraft reached its desired orbit (albeit much later than planned – 14 months after the launch [103].)

The successful rescue of AEHF-1 highlighted the utility of the high ΔV capabilities of EP systems, and may have aided or spurred parallel efforts in EP development. Boeing has developed an all-electric-propulsion variant of its 702 satellite bus termed the 702SP. The bus uses four Xenon Ion Propulsion System (XIPS) gridded ion engines to achieve both orbit insertion and stationkeeping. Two 702SP's have been launched and at the time of this writing (July 2015) are about four months into their low-thrust transit to geostationary orbit [23, 3]. The two satellites achieved launch masses of 1954 kg and 2205 kg, of which only 300-350 kg was the xenon propellant, compared to roughly 2000 kg that would have been required for chemical propellant. Airbus has also announced plans to deliver its own all-electric bus, using PPS5000 engines made by Snecma / SAFRAN group [39].

1.2 Motivation

1.2.1 Limitations of Electric Propulsion Systems

The low thrust of EP systems limits their capability: trip times are orders of magnitude longer than with chemical rockets. The rescue of AEHF-1 took 14 months, and the Boeing 702SP's are planned to take anywhere from 6 to 8 months to reach their desired orbits. These delays are not appealing for commercial satellite operators, who want the satellites to enter their planned orbits as fast as possible to begin generating revenue. In addition, improved thrust and acceleration capabilities are appealing to government space and military agencies as they enable an expanded range of missions and capabilities. Consequently, one of the well-funded goals in the continuing development of EP systems is to scale up to high power and high thrust architectures [32, 66].

Current EP systems are limited in thrust density by power losses to the thruster plasma-facing surfaces. In a study of the power loss mechanisms of the Aerojet-Rocketdyne BPT-4000 (now XR-5) Hall effect thruster, it was found that a major power loss mechanism was energy deposition to the plasma-facing walls and electrodes [26]. In order to achieve an increased thrust without thermal overload, the size of the EP device (and thus its mass) must grow hand in hand with the thrust. This mass growth (estimated at 10 kg/kW in [16]) detracts from the propellant mass savings that the EP system is designed to deliver. In the thruster plasma, the limitation manifests as the spatial number density of ions that can be sustained. This number density of ions is often called the plasma density n_p and is measured in m^{-3}.

Figure 1.4 shows the inverse relationship between attainable plasma density and required thruster size, for the case of a perfectly efficient thruster operating at 1500 seconds specific impulse. Current thrusters can attain plasma densities of 10^{18} m^{-3}. To implement higher power EP devices without incurring the mass penalty and structural burden of having a correspondingly massive thruster, it is necessary to

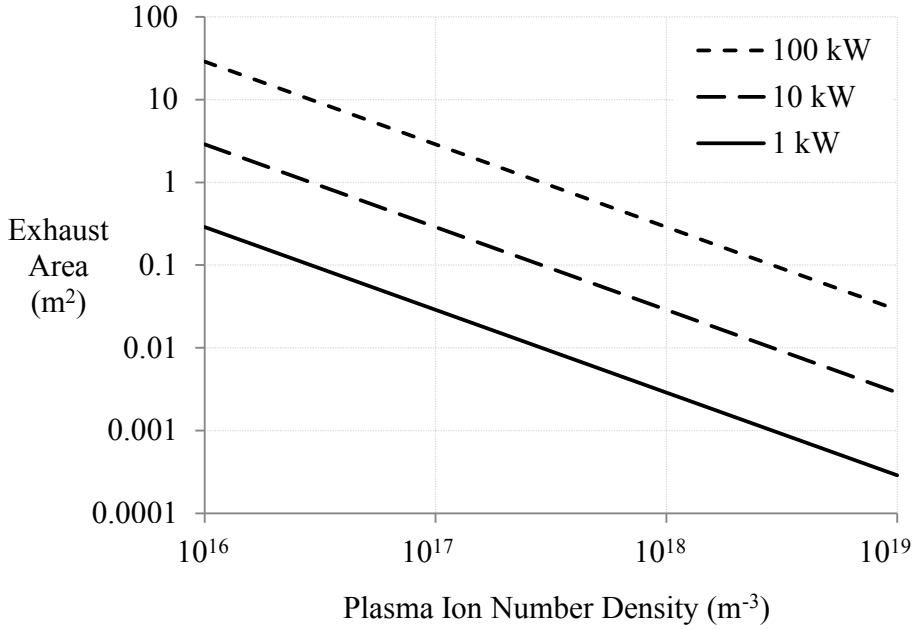

Figure 1.4: Ideal thruster exhaust area required vs. plasma density for different thruster power levels, $I_{sp} = 1500$ s, xenon

increase attainable plasma densities to the range of 10^{19} m^{-3} and higher. The plasma density limitation imposed by power losses to the thruster plasma-facing surfaces motivates us to study thruster-relevant plasma-wall interactions in more detail.

In additional to limiting plasma density, plasma-wall interaction have additional effects on thruster architectures. In Hall effect thrusters, secondary electrons ejected from the discharge channel are believed to play an important role in the controlling the plasma parameters of the main discharge. The space-charge-limit that limits ion engine thrust density occurs in the wall-interaction/sheath region at the accelerator grids. In MPD thrusters, the oscillating energy flux from the plasma manifests in the rapid erosion of the plasma-facing discharge electrodes. All of these occurrences indicate that an improved understanding of the plasma sheath region will give a clearer understanding of these mechanisms and losses, and perhaps reveal a way to mitigate them and increase the attainable plasma densities.

1.3 Thesis Overview

Due to the limitations on thrust density imposed by the plasma-wall interaction in current thruster architectures, this work will attempt to improve the basic understanding of the plasma-wall interaction in thrusters. The plasma-wall interaction is complicated by the occurrence of the plasma sheath, a thin layer of plasma adjacent to the wall where electrostatic forces become dominant.

The next chapter, Chapter II, provides background on the physics of plasma sheaths and discusses the current state of knowledge about sheaths. Chapter III describes the goals of the current research effort. Because the research is conducted as part of a collaborative research program between Georgia Institute of Technology (GT), Georgia Tech Research Institute (GTRI), University of Alabama (UA), and GWU, the team links and collaborative objectives are also described in Chapter III. Chapter IV describes the experimental apparatus used at GT to perform the experiments described in this thesis. Chapters V - IX describe the experiments conducted at GT, with some discussion of modeling done by GWU to simulate the experimental conditions. Chapter X summarizes the research outcomes and contributions and includes suggested directions for future investigations.

CHAPTER II

BACKGROUND

This chapter gives background on the physics of plasmas and plasma sheaths, and a literature review of some active research areas concerned with plasma-wall interactions.

2.1 Plasmas

Plasma is sometimes referred to as "the fourth state of matter" because it exhibits a range of behaviors that differ substantially from those of a solid, liquid, or gas. The particles in a plasma possess a high energy and freedom of motion relative to the other phases, often giving rise to fantastic visible glow phenomena and emissions across the electromagnetic spectrum. Some or all of the particles that make up a plasma are electrically charged, with the consequence that their motion generates electric and magnetic fields. The motion of the charged particles is in turn affected by the electric and magnetic fields, both self-generated and externally applied. Plasmas are relatively uncommon on Earth, but are the main constituent of stars and thus most of the rest of the mass of the observed universe. On Earth, plasmas can be seen in lightning bolts and the aurora. We can now also generate plasmas by technological means, as is done in electric propulsion devices. A picture of the aurora ionospheric plasma is shown in Figure 2.1, and an illustration is added to show the free charged particle populations.

2.1.1 Plasma Parameters

To describe plasmas in more detail, it is helpful to define several parameters. We already mentioned the plasma density n_{p}. We can be more specific and define the number density for each species in the plasma, for example the ion number density n_{i}, the electron number density n_{e} and the neutral number density n_{n}. If a given

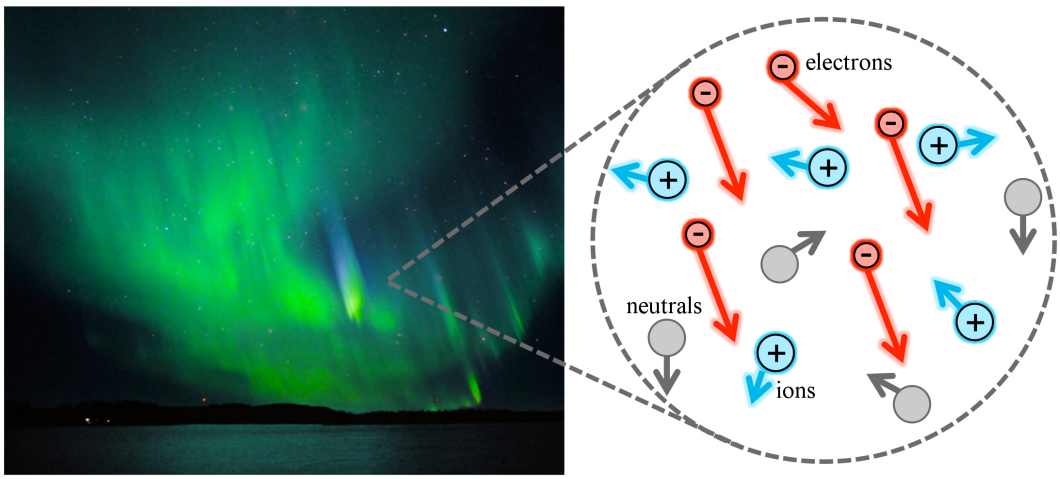

Figure 2.1: Photo of matter in the plasma phase (aurora ionospheric plasma) [76]. A plasma is composed of free charged particle populations and may also contain neutral particles.

species is in thermal equilibrium, and consequently its velocity distribution function is Maxwellian, the species can be assigned a temperature. In particular, the electron temperature T_e is often important. Electron temperatures can be very high compared to typical terrestrial temperatures, so they are often specified in units of electron Volts (eV):

$$(1 \text{ eV})\frac{e}{k_B} \approx 11604 \text{ K} \tag{2.1}$$

where e is the elementary charge and k_B is Boltzmann's constant. A plasma can often sustain an electron temperature substantially higher than the neutral and ionic populations because the rate of energy transfer between electrons and massive particles can be slow relative to other energy exchange processes due to the significant difference in mass, and the electrons often receive significant energy from ionization events and assorted electron heating mechanisms.

The number densities and temperatures describe the particles, but don't describe the collective behavior of the plasma. To describe collective behavior, it is helpful to define the Debye length and plasma frequency.

Debye Length

Consider a cylindrical electrode placed in a plasma and biased strongly negative. Positive charge carriers in the plasma will be attracted to the electrode and flow towards it. Negative charge carriers will be repelled and become depleted in the vicinity of the electrode. At an instant in time, there is a cloud of positive charge carriers near the electrode flowing to the electrode. From the point of view of a far away particle, the negative bias of the electrode is balanced by the positive charge of the surrounding cloud. In this way, the bulk plasma is "shielded" from the effect of the perturbing electrode. This process is referred to as Debye shielding, named after chemist Peter Debye who pioneered the effect in the study of ionic chemical solutions [27]. This shielding occurs on a length scale which is named the Debye length λ_{D}:

$$\lambda_{\mathrm{D}} = \sqrt{\epsilon_0 k_{\mathrm{B}} \sum_{\alpha=1}^{N_\alpha} \frac{T_\alpha}{q_\alpha^2 n_\alpha}} \tag{2.2}$$

A derivation of the Debye length is included in Appendix A.4. In equation (2.2), the subscript α varies over each of the charged species present in the plasma, which typically include electrons and ions of varying charge state. The number density of each species is n_α, the temperature of each species is T_α, and the charge of each species is q_α. The electron contribution is often dominant, and so the Debye length is often very nearly equal to the electron Debye length λ_{d}:

$$\lambda_{\mathrm{d}} = \sqrt{\frac{\epsilon_0 k_{\mathrm{B}} T_{\mathrm{e}}}{e^2 n_{\mathrm{e}}}} \tag{2.3}$$

The Debye length governs the size of the Debye shielding layer, which is termed the Debye sheath or plasma sheath and is often several Debye length in thickness. From Appendix A.4, it can be seen that an approximate solution for the potential includes a negative-exponential decay term in addition to the $1/r$ decay from electrostatics:

$$\phi(r) = \frac{q}{4\pi\epsilon_0 r} \exp\left(-\frac{r}{\lambda_{\mathrm{D}}}\right). \tag{2.4}$$

In equation (2.4), r is the radial spatial coordinate of distance from the electrode surface, q is the charge stored on the electrode, and ϕ is the electrical potential due to the surface charge. The negative-exponential term dominates the decay of the potential with increasing r, and thus we have the result that the potential due to the wall charge is almost completely zero at distances greater than a few Debye lengths from the wall. Thus we say that the plasma "shields" or "screens out" perturbing potentials over a few Debye lengths, although mathematically the potential never fully reaches zero except in the limit at $r = +\infty$.

The electron Debye length scales as the square root of the electron temperature and the inverse square root of the electron number density. Electron number densities typically vary over more orders of magnitude than electron temperature, so the electron Debye length is mainly dictated by the plasma density. For a typical Hall effect thruster plasma with $T_\mathrm{e} = 10$ eV and $n_\mathrm{e} = 10^{18}$ m^{-3}, the electron Debye length is roughly 20 µm.

Plasma Frequency

How quickly can the charged species in a plasma react to a perturbation? We can first state that the electrons will respond more rapidly than ions due to their low mass and high temperature. To define the plasma frequency, consider a volume of ions of number density n_i as stationary point charges of $+e$ and consider the motion of a nearby equal volume of electrons. The electrons are coulombically attracted to the ions and accelerate toward them. Because the ions are point charges, the electrons pass through the ion volume without collision and overshoot the ions. The electrons thus oscillate in the potential well of the ions. The frequency of this oscillation is the electron plasma frequency ω_pe:

$$\omega_\mathrm{pe} = \sqrt{\frac{n_\mathrm{e} e^2}{m_\mathrm{e} \epsilon_0}} \tag{2.5}$$

where m_e is the electron mass. A similar (lower) frequency can be defined for the plasma ions by reversing the roles of the particles. We can use the electron plasma frequency and Debye length to formalize the definition of a plasma.

2.1.2 Criteria for a Plasma

For a system of matter to be considered a plasma, it must meet three criteria:

1. The physical length scale of the system L must be much larger than the electron Debye length:
$$\frac{L}{\lambda_d} >> 1 \tag{2.6}$$

2. There must be a large number of charged particles N_d within a Debye sphere (a sphere with radius equal to the electron Debye length):
$$N_d = n_e \frac{4}{3}\pi {\lambda_d}^3 >> 1 \tag{2.7}$$

3. There must be enough charged particles that the electron plasma frequency is faster than the gaseous (collisional) timescale:
$$\frac{\omega_{pe}}{\nu_c} >> 1 \tag{2.8}$$

in which ν_c is the collision frequency. Criterion 1 can be satisfied for a plasma with any given density and temperature if the physical length scale L is sufficiently large. This criterion thus generally tells us that systems found by zooming in to consider atomic-scale lengths will not behave as plasmas. Criterion 2 scales with $T_e^{1.5}$ and with $n_e^{-0.5}$, so a system must carry enough electron temperature to regularly bring the electrons into close enough proximity to each other for electrostatic interaction. The plasma frequency ω_{pe} in criterion 3 scales with $n_e^{0.5}$ and the collision frequency ν_c scales with n_n, so it is necessary to have enough free electrons in proportion to neutrals in order for the plasma to behave primarily electrically rather than collisionally. Within

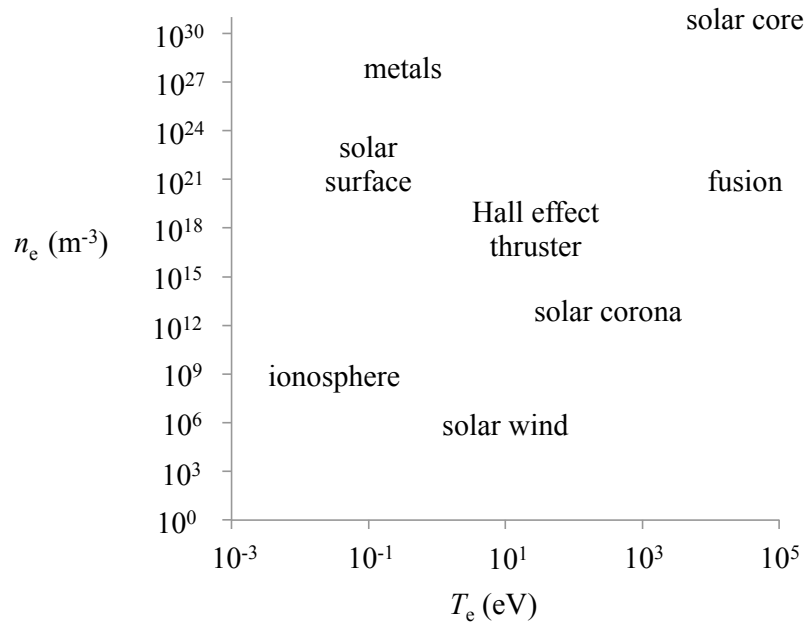

Figure 2.2: Wide parameter space of plasmas in electron number density n_e and electron temperature T_e, with nominal parameters of some different types of plasmas marked.

these criteria, the range of possible plasma number densities and temperatures still spans very many orders of magnitude as shown in Figure 2.2.

To completely analyze a plasma thus defined (neglecting complications due to the quantum-mechanical behavior of plasma electrons) one would have to integrate the equation of motion of every particle in the plasma, along with the electric and magnetic fields generated using the full set of Maxwell's equations. This task is intractable for all plasmas of interest with presently available computational power, and plasma analysis must proceed using some level of simplification.

2.1.3 Quasineutrality

One of the simplifications that a plasma as defined often permits is the assumption of quasineutrality. Quasineutrality holds that the net charge of a given plasma volume is zero, or that the given plasma volume is electrically neutral on average. This statement

can be mathematically expressed as:

$$\sum_{\alpha} n_{\alpha} q_{\alpha} = 0 \tag{2.9}$$

If we consider a plasma with only singly-charged positive ions and electrons, this means that the number density of ions and electrons are equal, and the term "plasma density" (n_{p}) can apply to either quantity.

$$n_{\mathrm{i}} = n_{\mathrm{e}} = n_{\mathrm{p}} \tag{2.10}$$

Quasineutrality is often a very good description of a plasma due to the aforementioned low mass and high mobility of plasma electrons. If an imbalance of the positive- and negative-charged species were to arise, the resulting electric field would rapidly drive electrons towards or away from the region and equalize the charge imbalance.

2.1.4 Discharges and Plasma Potential

Plasmas are electrically conductive due to their free charged particle populations, and as such it is possible to flow electric current through them. An example is a fluorescent light bulb or neon sign tube, where the plasma forms the conductive path in the circuit between the two electrodes at either end of the tube. These types of plasma circuits are typically called plasma discharges or alternatively gas discharges (though the ionization that occurs in the gas makes it a plasma when the discharge is being operated.) The current that is conducted between the discharge electrodes is called the discharge current (I_{D}), and the voltage applied to the electrodes is called the discharge voltage (V_{D}).

If a plasma can be used as a circuit element, it must be possible to define the voltage or electrical potential at points throughout the plasma. This electrical potential is often referred to as the "plasma potential" and assigned the symbol ϕ_{p} or V_{p}, or just ϕ. In general, the plasma potential can vary with time and with spatial location throughout the extent of the plasma. The spatial and temporal distribution of the

plasma potential throughout a plasma is nice to know from a diagnostic standpoint, as it gives insight into the electrostatic component of the Lorentz force that is felt by the charged particles – the electric field $\vec{E}$ can be obtained from the negative gradient of the potential (2.11).

$$\vec{E} = -\nabla\phi \tag{2.11}$$

Because plasmas are often highly conductive, sometimes it can be assumed that the changes in plasma potential throughout the spatial extent of the plasma are small and that a singular "plasma potential" can be applied to the whole of the plasma. In many situations however, particularly those involving discharge plasmas, this is not the case and the plasma potential varies significantly with both time and spatial position. The neon sign tube is an example: the electric field that is needed to sustain the discharge throughout the length of the tube is significant, perhaps it is order of 1-10 V/cm. Thus to supply a long tube of plasma to form words in a neon sign, a high-voltage transformer is needed to supply $\approx$ 10 kV voltage across the electrodes at the ends of the long tube. The plasma potential thus varies across kilovolts as a function of axial position in the tube, not unlike how voltage varies with position of a potentiometer tap in a circuit. Though useful, the analogy is limited: even in this relatively straightforward case, the plasma carries inductive and capacitive components in addition to DC resistance, and the sheath phenomena that occur at the plasma electrodes and boundaries introduce additional complications into the plasma potential structure. In the next section we will discuss these sheath phenomena in much more detail, as they are a central feature of the plasma-wall interaction which is the main target of this research.

2.2 Plasma Sheaths

The plasma sheath is the name given to the non-quasineutral layer that forms at the Debye-shielded boundary of a confined plasma. As the physical length scale of the

sheath is on the order of the Debye length, sheaths do not meet Criterion 1 for a plasma and so do not show typical plasma behavior. In general, sheaths will manifest in any plasma in contact with an external wall or surface to enforce the wall's electrical boundary condition. The timescale of sheath formation is the inverse ion plasma frequency [15]. The angular ion plasma frequency ω_{pi} is:

$$\omega_{\mathrm{pi}} = \sqrt{\frac{n_{\mathrm{i}} e^2}{\epsilon_0 m_{\mathrm{i}}}} \tag{2.12}$$

where m_{i} is the ion mass. So the inverse (with the conversion to units of seconds) is:

$$\tau_{\mathrm{pi}} = \frac{2\pi}{\sqrt{\frac{n_{\mathrm{i}} e^2}{\epsilon_0 m_{\mathrm{i}}}}} \tag{2.13}$$

For thruster plasmas, this sheath formation timescale (2.13) is on the order of microseconds.

Figure 2.3 shows a one-dimensional profile of the electrostatic potential within a typical sheath. Because the negative gradient of the electrostatic potential is the electric field (*c.f.* equation (2.11)), the potential profile tells you the forces imposed on the charged particles by the sheath electric field. Ions are accelerated down potential hill towards regions of low potential, while electrons are accelerated up the gradient towards regions of high potential.

There is an interesting analogy between the plasma sheath and the boundary layer phenomenon of viscous fluid flow. In the latter case, viscous forces are insignificant over the bulk of the flow, except at a critical layer at the wall where they become dominant and enforce the wall boundary condition (no-slip). In the case of the plasma sheath, it is the electrostatic forces that are insignificant over the bulk of the plasma (due to quasineutrality) except for the critical layer near the wall. Similar to the importance of boundary layers to the analysis of viscous flow over objects, sheaths are essential to the analysis of plasmas interacting with objects.

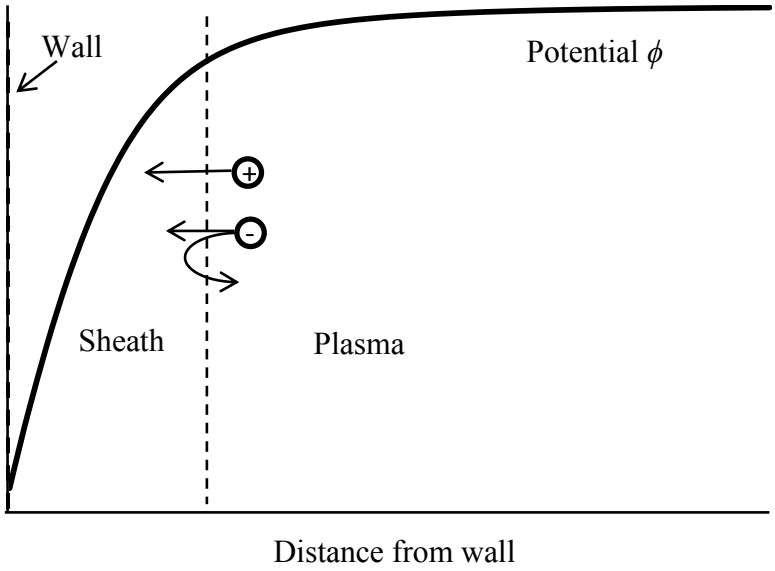

Figure 2.3: Electrical potential profile of a typical plasma sheath. Positively charged ions are accelerated from high potential regions towards low potential, while electrons are repelled from low potential regions.

2.2.1 Wall Boundary Conditions

The sheath arises in response to an external boundary condition, typically a solid wall such as an electrode or the bounding wall of the plasma discharge chamber. One can consider two main categories of wall boundary conditions: those in which the wall potential is externally enforced (as is the case for a powered electrode,) and those in which the wall is electrically isolated and allowed to 'float' to the potential which equalizes positive and negative charge fluxes to the wall. The latter case is called a "floating" boundary condition, and the potential attained is called the "floating potential" or ϕ_{f}. Since the charge fluxes to a floating wall are balanced, there is zero net current flow to a floating wall. This is the boundary condition for all insulator materials in contact with a plasma, because the insulator material is unable to flow current and enforce potentials other than the floating potential.

2.2.2 Child-Langmuir Sheaths

The most fundamental formulation of the plasma sheath is the famous Child-Langmuir sheath, first derived by Child in 1911 [21]. It contains many assumptions, but gives results about the sheath which are quantitatively accurate in a large number of plasmas of interest a century later. Beyond the assumptions and result which are given here, a full derivation is included in the Appendix A.5.

Consider a quasineutral plasma filling the one-dimensional space $x_{\mathrm{CL}} < 0$. The sheath begins at $x_{\mathrm{CL}} = 0$ and extends a finite length d, where a wall is located at $x_{\mathrm{CL}} = +d$. The distance d is the sheath thickness. Note that the definition of x_{CL} is reversed from our usual definition of the coordinate system in which x is the distance away from the wall; the two are related by:

$$x_{\mathrm{CL}} = d - x \tag{2.14}$$

The plasma is collisionless, unmagnetized, quiescent, contains only singly charged ions of negligible temperature and electrons. Plasma electrons are assumed to be fully repelled from the sheath region. Ions are assumed to enter the sheath at $x = 0$ with negligible velocity, and it is assumed that their space charge has shielded the wall potential to the point where the electric field at $x = 0$ is negligible. The wall absorbs all incident particles.

Applying conservation of mass and conservation of energy to the ion fluid under the forgoing assumptions and integrating the electrostatic Poisson equation, one arrives at the Child-Langmuir sheath:

$$\Phi(\xi_{\mathrm{CL}}) = \mathrm{C}_1 \; {\xi_{\mathrm{CL}}}^{\frac{4}{3}} \tag{2.15}$$

$$\xi_{\mathrm{CL}}(\Phi) = \mathrm{C}_2 \; \Phi^{\frac{3}{4}} \tag{2.16}$$

where C_1 and C_2 are constants related to the density of ions at the sheath edge and

$$\xi_{\mathrm{CL}} = \frac{x_{\mathrm{CL}}}{\lambda_{\mathrm{d}}} \tag{2.17}$$

$$\Phi = -\frac{e\phi}{k_{\mathrm{B}}T_{\mathrm{e}}} \tag{2.18}$$

If it is assumed that the density of ions at the sheath edge is equal to the bulk plasma density, or equivalently if the debye length is calculated using the plasma density at the sheath edge, it can be shown that $C_1 \approx 1.36$ and $C_2 \approx 0.793$ (*c.f.* Appendix A.5.)

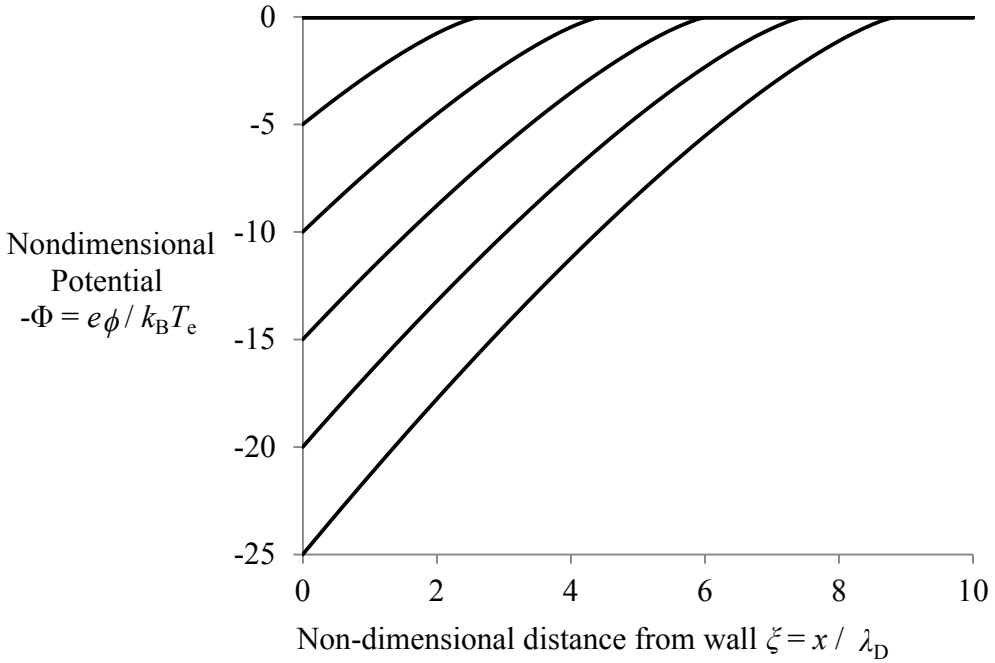

Figure 2.4: Non-dimensional potential profiles of Child-Langmuir sheaths. The sheath thickness expands as the 3/4 power of the wall voltage (2.16).

Figure 2.4 shows some potential profiles calculated using equation (2.15) and $C_1 = 1.36$, for wall potentials of 5 - 25 electron temperatures. The normal spatial scale is used such that the wall is at $x = 0$ and the sheath and plasma occupies $x > 0$. The behavior of the sheath can be seen: if the wall voltage with respect to the plasma is increased, the sheath expands as the 3/4 power of the applied voltage. Because the Child-Langmuir sheath neglects the effects of the plasma electrons, it is most accurate for cases when there are very few electrons present in the sheath, that is when the sheath voltage is very highly negative with respect to the plasma potential.

2.2.3 Presheaths and the Bohm Criterion

A shortcoming of the Child-Langmuir solution can be seen in the assumption of ions entering the sheath with zero velocity at a point of zero electric field strength. If the ions had zero velocity at a region of zero field strength, they would feel no impetus to move towards the wall. Therefore one can reason that the ions must enter the non-quasineutral sheath region at some finite velocity.

For a rigorous treatment of the plasma-sheath transition, it is necessary to consider the conditions of the quasineutral plasma as it approaches the wall. The current document follows the original derivation which proceeds only from the sheath side of the problem, which is much shorter than matching the plasma side with the sheath side but the result is less specific.

If we consider the normalized electrostatic Poisson equation in the non-quasineutral sheath region in 1D with only ion and electron species present, it is:

$$\frac{\mathrm{d}^2\Phi}{\mathrm{d}\xi^2} = N_\mathrm{i}(\Phi) - N_\mathrm{e}(\Phi) \tag{2.19}$$

where the normalizations (2.17) and (2.18) have been used and the number densities are normalized to the plasma density at the sheath edge n_0,

$$N_\mathrm{i} = \frac{n_\mathrm{i}}{n_0} \tag{2.20}$$

$$N_\mathrm{e} = \frac{n_\mathrm{e}}{n_0}. \tag{2.21}$$

We integrate the Poisson equation (2.19) once to obtain

$$\frac{1}{2}\left(\frac{\mathrm{d}\Phi}{\mathrm{d}\xi}\right)^2 = \int_0^\Phi (N_\mathrm{i} - N_\mathrm{e})\ \mathrm{d}\Phi'. \tag{2.22}$$

The left hand side of equation (2.22) is unconditionally positive, so the right-hand side must also be positive. If we expand the right hand side in Taylor series about the point $\phi = 0$, the first two terms are zero but the second order term is non-zero, giving the inequality

$$\frac{1}{2}\Phi^2 \left[\frac{\mathrm{d}N_\mathrm{i}}{\mathrm{d}\Phi}_{\Phi=0} - \frac{\mathrm{d}N_\mathrm{e}}{\mathrm{d}\Phi}_{\Phi=0}\right] \geq 0 \tag{2.23}$$

$$\frac{\mathrm{d}N_\mathrm{i}}{\mathrm{d}\Phi}_{\Phi=0} - \frac{\mathrm{d}N_\mathrm{e}}{\mathrm{d}\Phi}_{\Phi=0} \geq 0. \tag{2.24}$$

To use equation (2.24), we need to know how the number densities N_i and N_e depend on potential Φ. If we use the expression for the electron density from the Boltzmann relation (2.25) (*c.f.* Appendix A.2), normalizing with (2.21), and (2.18), we obtain

$$n_\mathrm{e} = n_0 \exp\left(\frac{e\phi}{k_\mathrm{B}T_\mathrm{e}}\right) \tag{2.25}$$

$$N_\mathrm{e} = \exp\left(-\Phi\right). \tag{2.26}$$

An equation for the ion density can be developed by considering the ions as a fluid, applying conservation of mass and energy, and assuming that they enter the sheath with a speed u_i0 but negligible temperature ($T_\mathrm{i} = 0$).

$$n_\mathrm{i}u_\mathrm{i} = n_0 u_\mathrm{i0} \tag{2.27}$$

$$\frac{1}{2}m_\mathrm{i}u_\mathrm{i}^2 = \frac{1}{2}m_\mathrm{i}u_\mathrm{i0}^2 - e\phi \tag{2.28}$$

We can combine (2.27) and (2.28) to get an expression for n_i,

$$\frac{n_\mathrm{i}}{n_0} = \frac{1}{\sqrt{1 - \frac{2e\phi}{m_\mathrm{i}u_\mathrm{i0}^2}}} \tag{2.29}$$

Introducing a normalization for the ion velocity entering the sheath u_i0, we can give a dimensionless expression for N_i.

$$U_\mathrm{i0} = \frac{u_\mathrm{i0}}{\sqrt{\frac{k_\mathrm{B}T_\mathrm{e}}{m_\mathrm{i}}}} \tag{2.30}$$

$$N_\mathrm{i} = \frac{1}{\sqrt{1 + \frac{2\Phi}{U_\mathrm{i0}^2}}} \tag{2.31}$$

Plugging (2.26) and (2.31) into (2.24), we can find a condition on U_i0,

$$\frac{\mathrm{d}}{\mathrm{d}\Phi}\left[\left(1 + \frac{2\Phi}{U_\mathrm{i0}^2}\right)^{-\frac{1}{2}}\right]_{\Phi=0} - \frac{\mathrm{d}}{\mathrm{d}\Phi}\left[\exp\left(-\Phi\right)\right]_{\Phi=0} \geq 0 \tag{2.32}$$

$$\left(-\frac{1}{{U_\mathrm{i0}}^2}\right) - (-1) \geq 0 \tag{2.33}$$

$$U_{\mathrm{i}0} \geq 1 \tag{2.34}$$

Or in dimensional form,

$$u_{\mathrm{i}0} \geq \sqrt{\frac{k_{\mathrm{B}} T_{\mathrm{e}}}{m_{\mathrm{i}}}} = u_{\mathrm{B}} \tag{2.35}$$

This result is the Bohm Criterion, named for David Bohm who first derived it [12]. It gives the striking result that the ions must attain the ion sound speed at the sheath edge. The ion sound speed is thus termed the Bohm speed u_{B} in this context. The equation (2.24) is a more general version of the Bohm Criterion, without specification of the number density dependence on potential.

The limitation inherent in that we have only considered the problem from the sheath side is that the result is an inequality rather than an equation. Considering also the plasma side, it can be shown that in nearly all cases, the relation (2.35) holds with equality, referred to as the marginal validity of the Bohm criterion [5].

In order to attain the Bohm speed, ions must arrive at the sheath edge with a directed energy of half the electron temperature. This energy is supplied by a potential drop occurring over a larger length scale, rather than the electrostatic length scale (Debye length) of the sheath. This region of more gradual potential fall leading up to the sheath is termed the "presheath". A nominal diagram of a presheath layer is shown in Figure 2.5 , adapted from reference [37].

The presheath potential fall can be found as the potential required to accelerate the ions to the Bohm speed:

$$e\phi_{\mathrm{ps}} = \frac{1}{2} m_{\mathrm{i}} u_{\mathrm{B}}^2 \tag{2.36}$$

$$\phi_{\mathrm{ps}} = -\frac{1}{2} \frac{k_{\mathrm{B}} T_{\mathrm{e}}}{e} \tag{2.37}$$

Unlike the sheath region, the presheath is quasineutral, so the plasma density will decrease over the course of the presheath as can be seen from the Boltzmann relation, equation (2.25). The plasma density at the sheath edge (the sheath-presheath

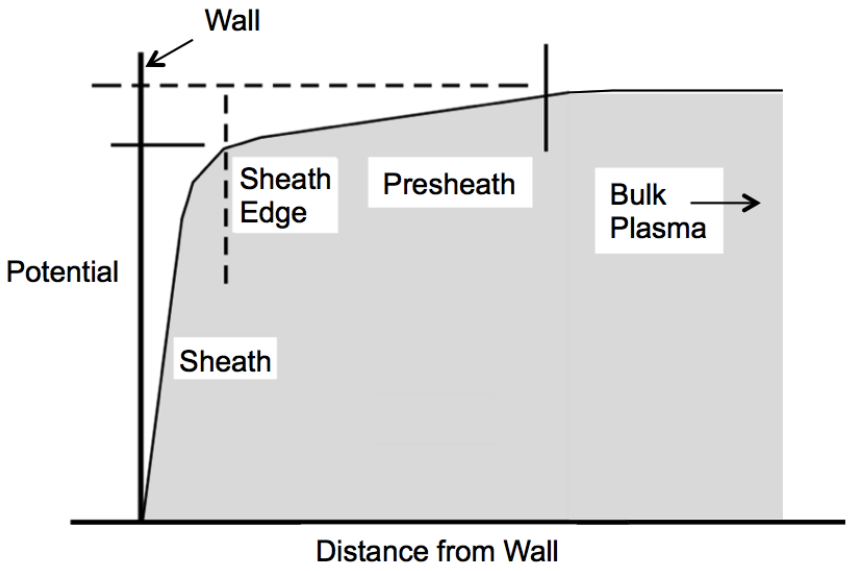

Figure 2.5: Schematic of sheath-presheath-plasma potential profile, adapted from Goebel-Katz [37]. Sheath thickness scales with Debye length, Presheath thickness varies depends on formation mechanism (ion mean free path, ionization length, plasma device length.)

boundary) is thus:

$$n_{e0} = \exp\left(-\frac{1}{2}\right) n_p \approx 0.6 n_p \approx \frac{n_p}{2} \tag{2.38}$$

When neutral collisions are present in the sheath, the presheath potential drop increases from this result [54, 72], so the presheath density drop is sometimes described by a variable parameter:

$$n_{e0} = \alpha_{ps} n_p \tag{2.39}$$

In reality the degree of quasineutrality decreases gradually, so the transition between plasma and sheath occurs smoothly and one can specify the "sheath thickness" in different ways, similar to the multiple definitions of boundary layer thickness in fluid mechanics. A number of detailed analyses of the presheath-sheath transition have been done in the literature, including those by Riemann [78, 79], Franklin [33], and Benilov [11]. It is shown that the presheath exists because of the wall boundary and the need to accelerate ions to the Bohm speed to establish the non-quasineutral sheath region. If the collisional mean free path is less than the plasma length scale, the presheath

must occur over a thickness of the mean free path, or else the ion acceleration will be disrupted by collisions. Likewise, presheaths can occur on ionization, magnetic, or geometric length scales, where the ultimate presheath length being the smallest of these length scales in a given situation. If the ions are given a directed flow velocity into the sheath greater than or equal to the Bohm velocity, for example if they have been accelerated by an electric propulsion device, one could argue that a presheath will not form because the Bohm criterion is already satisfied.

2.2.4 Sheath Floating Potential

With the results of the Child-Langmuir sheath and Bohm criterion, we can form an expression for the floating potential:

$$I_{\mathrm{e}} = I_{\mathrm{i}} \tag{2.40}$$

$$\frac{1}{4} n_{\mathrm{e}0} e A \sqrt{\frac{8 k_{\mathrm{B}} T_{\mathrm{e}}}{\pi m_{\mathrm{e}}}} \exp \frac{-e\phi_{\mathrm{f}}}{k_{\mathrm{B}} T_{\mathrm{e}}} = n_{\mathrm{i}0} e A \sqrt{\frac{k_{\mathrm{B}} T_{\mathrm{e}}}{m_{\mathrm{i}}}} \tag{2.41}$$

$$\phi_{\mathrm{f}} = \frac{k_{\mathrm{B}} T_{\mathrm{e}}}{e} \ln \left[\sqrt{\frac{m_{\mathrm{i}}}{2\pi m_{\mathrm{e}}}} \right] \tag{2.42}$$

The expression for electron current follows from the thermal flux from a maxwellian plasma and the Boltzmann relation. It is thus only the highest energy electrons of the maxwellian distribution that are able to pass through the potential barrier of the sheath and impact the wall. The expression for the ion current is due to the Bohm criterion. The subscript "0" on the number densities indicates that they refer to the "sheath edge" conditions (*c.f.* equation 2.38,) and they are equal given the assumption of a quasineutral presheath. The result shows that the floating potential scales directly with the electron temperature and is weakly dependent on the ion mass. Using the Child-Langmuir Law (2.15) to relate the floating potential (2.42) to sheath thickness, we can express the sheath thickness d for a given plasma over a floating wall.

$$\mathrm{C}_1 \xi^{\frac{4}{3}} = \ln \left[\sqrt{\frac{m_{\mathrm{i}}}{2\pi m_{\mathrm{e}}}} \right] \tag{2.43}$$

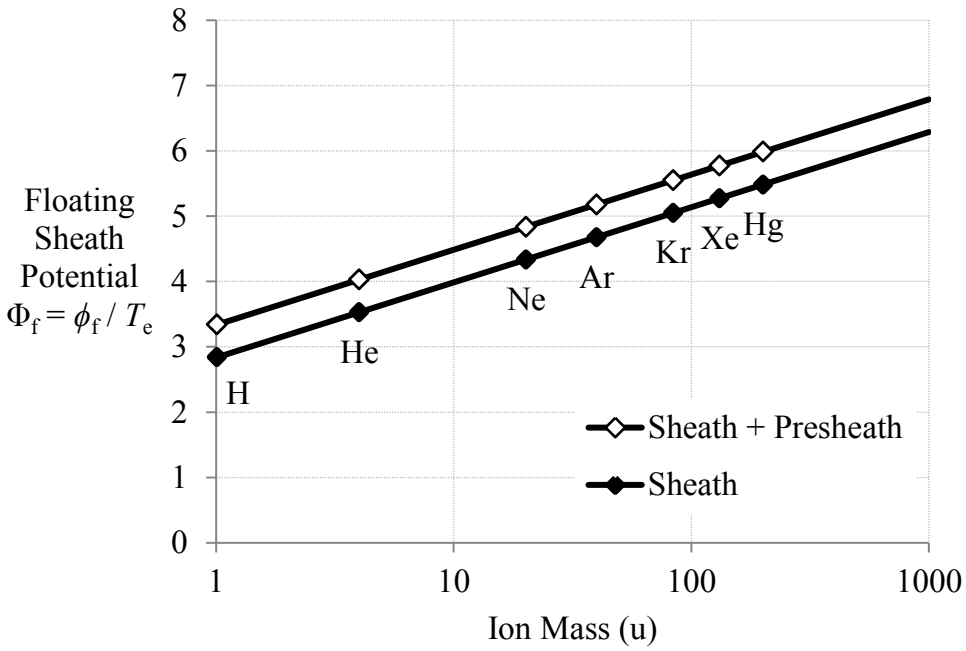

Figure 2.6: Sheath floating potential (units of T_e) vs. ion mass

$$\xi_d = \frac{d}{\lambda_d} = \left(\frac{1}{C_1} \ln \left[\sqrt{\frac{m_i}{2\pi m_e}} \right] \right)^{\frac{3}{4}} \tag{2.44}$$

Figure 2.7 shows that the sheath thickness grows logarithmically with ion mass. Note that this thickness is only valid for a floating wall, is subject to the assumptions of the Child-Langmuir law, and does not include presheath thickness.

2.2.5 Experimental Results

Measurements performed using laser-induced fluorescence (LIF) [38, 7] ion acoustic waves [59, 58] and emissive probes [72, 73] have provided measurements of the potential structure, ion density profile, and ion velocity profile in nearly collisionless ion sheaths. It is now confirmed that the Child-Langmuir potential profile and sheath width scaling are accurate in the near-wall sheath region, and that ions do indeed attain the Bohm velocity at the sheath edge. It is also shown that collisional presheaths scale with the collisional mean free path.

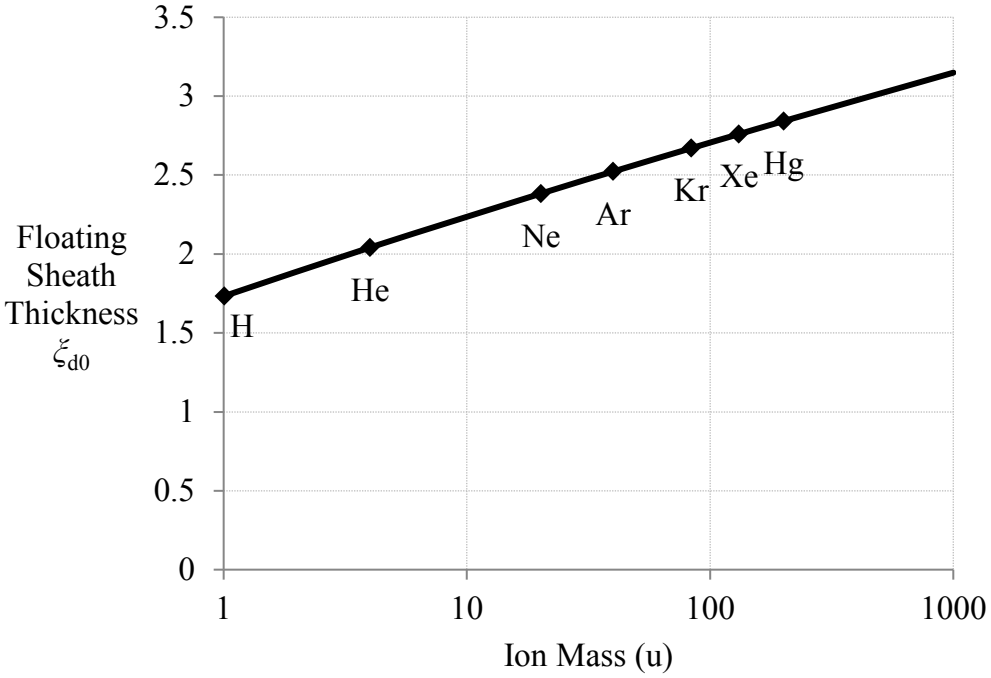

Figure 2.7: Thickness of Child-Langmuir sheaths over floating wall, $\xi_d = \frac{d}{\lambda_d}$

2.3 Influence of Electron Emission from the Wall

Electron emission from the wall complicates the Child-Langmuir picture of the sheath. Such emission is important in Hall effect thrusters, and it has been found experimentally that the thruster performance varies substantially with choice of discharge wall material [52, 9, 77]. This change in performance is thought to have much to do with the ability of the wall material to emit electrons into the plasma.

2.3.1 Electron Emission Processes

In the typical Child-Langmuir case of the sheath, particles from the plasma travel from the bulk plasma through the sheath and strike the wall, and are considered lost from the plasma to surface recombination. In general it is also possible that the wall may also emit particles back into the plasma. Electrons emitted in this way are quantified by the electron emission yield, γ:

$$\gamma = \frac{\text{number of electrons emitted from wall}}{\text{number of electrons incident on wall}} \tag{2.45}$$

The electron yield varies with conditions of the wall (wall material, grade, surface finish) and the plasma (incident energy distribution, incidence angle.) As defined, it is a "total" or "overall" yield, with the understanding that there are multiple mechanisms that can cause electrons to be emitted and that the properties of the emitted populations may be quite different. Broadly, electron emission from a wall can be classified as either thermionic emission, field emission, true secondary emission, or electron backscattering / elastic emission.

Thermionic emission

In thermionic emission, the wall temperature gives enough energy to the free electrons of the wall material for a fraction of them to overcome the material work function and escape the wall. Thermionic emission depends exponentially on wall temperature and work function, following Richardson's Law:

$$J = A_{\mathrm{G}} T_{\mathrm{w}}^2 \exp \frac{-W}{k_{\mathrm{B}} T_{\mathrm{w}}} \tag{2.46}$$

where A_{G} is a material-dependent constant, T_{w} is the wall temperature, and W is the material work function.

Field emission

Field emission requires very high electric fields (order of 10^7 - 10^8 V/m) to exist at the emission site, where they cause a quantum-mechanical effect that allows electrons to tunnel free from the wall material [36]. This mechanism is not likely to occur in plasmas unless the plasma density is extremely high and/or the wall is specifically shaped at the nanoscale to achieve the needed field concentration, so it can be neglected in most plasmas not specifically designed to achieve it. This may no longer hold if plasma density can be increased to the degree where sheath electric fields can cause field emission from adjacent walls.

True secondary emission

So-called "true" SEE results from the transfer of the incident kinetic energy from the plasma to near-surface free electrons, which then propagate to the surface and escape. This is distinct from thermionic emission in that it is a kinetic phenomenon and thus can be significant to the plasma-wall interaction even when wall temperatures are very much lower than the work function. The yield typically exhibits a maximum with incident energy due to the trade-off between delivered energy and penetration depth, with the maximum yield typically occurring in the 500 - 1500 eV range. Figure 2.8 shows a typical set of measured yield curves [88]. As noted in Figure 2.8 there is typically an increase in observed SEE when electrons of a given energy impact at an oblique angle, as it keeps the region of energy deposition closer to the surface so that the excited electrons can more easily escape. At typical thruster plasma electron energies of less than 100 eV, SEE yield increases monotonically (often linearly) with incident energy.

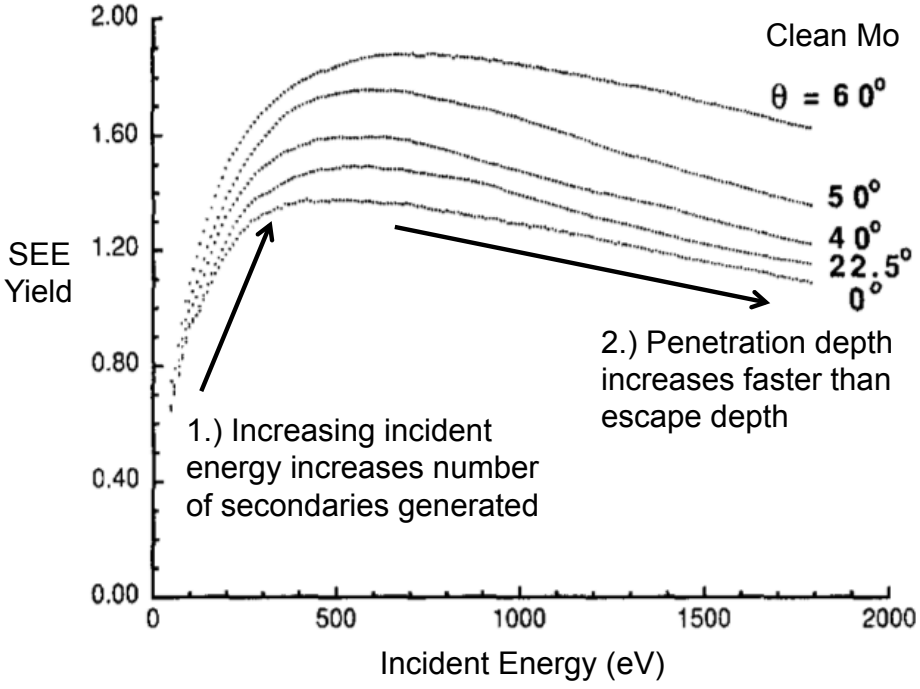

Figure 2.8: Annotated secondary electron emission (SEE) yield curves of molybdenum under electron bombardment. θ = incidence angle. Data from Shih *et al.* [88].

Backscatter emission

Backscattered electrons rebound from the surface into the plasma, carrying a significant fraction of their incident energy. At energies > 500 eV, the backscattering cross section monotonically increases with atomic weight of the surface molecules. At energies < 500 eV, the dependence of backscattering cross section becomes non-monotonic with atomic weight. Low energy electron microscopy (LEEM) devices exploit this phenomenon to achieve imaging of low molecular weight adsorbed gases on high molecular weight substrates [10].

2.3.2 Emitting-Wall Sheath Models

Ultimately, the electrons emitted from the wall are accelerated through the sheath into the plasma. Their presence as a charged species in the sheath modifies the potential profile. The canonical analysis of the sheath over an electron-emitting floating wall boundary is due to Hobbs and Wesson [42]. Their results have indicated the existence of a space-charge-limited regime for sheaths over a strongly emitting wall, in which there is a potential dip near to the wall but the wall remains at a lower potential than the bulk plasma.

The use of the term "space-charge-limited" to refer to the Hobbs-and-Wesson sheath results carries the possibility for confusion, due to the similar terminology applied to ion engine accelerator grids. In the Hobbs-Wesson sheath analysis, the number density of the negatively charged emitted electrons from the wall becomes high enough so that they repel additional emitted electrons back towards the emitting surface. In the ion engine accelerator grids, the positively charged ions forced through the sheaths at the grid apertures are subject to the Child-Langmuir physics and constitute a positive space charge. So the term "space-charge-limited" can apply to any situation where a non-neutral region of like-charged particles (space charge) builds up and establishes an electric field on the scale of the Debye length.

The potential dip structure that is proposed to reflect a portion of the emitted electrons back to the wall has also been referred to as a 'virtual cathode'. Recent simulations [19, 89, 20] and kinetic analysis [18] of sheaths over strongly emitting surfaces have proposed that further sheath regimes may exist beyond the limit of the Hobbs and Wesson sheath if electron emission from the wall increases, suggesting that the sheath potential profile over an electrically isolated ('floating') surface may flatten and even drive the wall to a higher potential than the plasma, referred to as an "inverse sheath". Figure 2.9 gives an illustration of the different sheath theories (the CL and H&W are quantitatively calculated, but the inverse and virtual cathode profiles are illustrative only.)

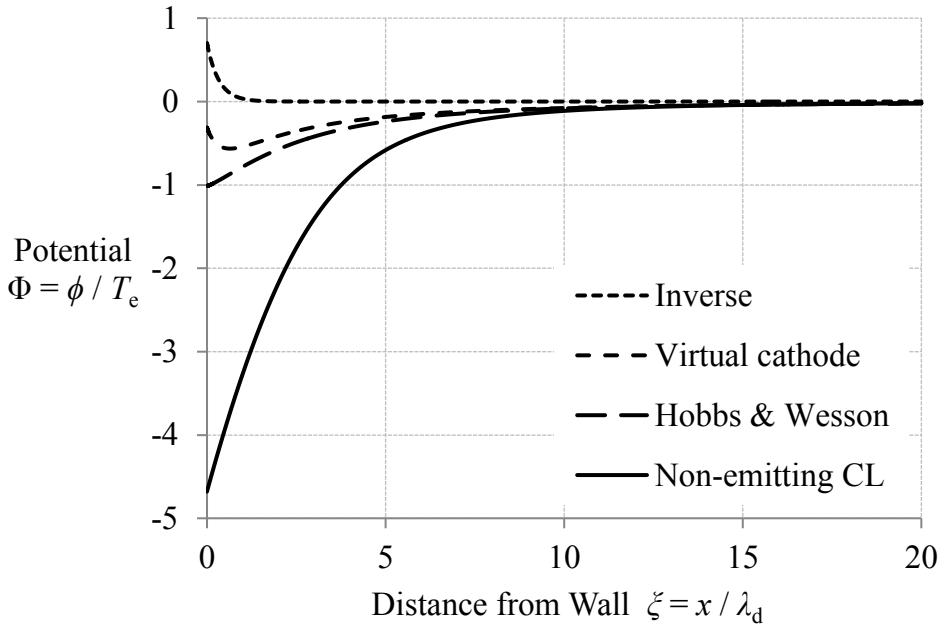

Figure 2.9: Illustration of range of possible sheaths for a floating electron-emitting wall (CL and H&W quantitatively calculated for argon, inverse and virtual cathode profiles illustrative only.)

2.3.3 Hobbs and Wesson Model

In the Hobbs and Wesson model, the energy of the emitted electrons is assumed to be zero when they are initially emitted from the wall. The emitted electrons

are accelerated through the sheath into the plasma. It is assumed that the emitted electrons stream past the plasma electrons with no interaction except through the jointly-determined electric field.

With these assumptions, a system of two equations can be formed to solve for the unknown wall potential ϕ_{w} and ion energy at the sheath edge E using the zero net current condition for the floating surface and the generalized Bohm criterion, modified to include the contribution of the emitted electrons:

$$\frac{1}{4}\sqrt{\frac{8k_{\mathrm{B}}T_{\mathrm{e}}}{\pi m_{\mathrm{e}}}}\left[1-\frac{\gamma}{1-\gamma}\sqrt{\frac{-Em_{\mathrm{e}}}{e\phi_{\mathrm{w}}m_{\mathrm{i}}}}\right]\exp\frac{e\phi_{\mathrm{w}}}{k_{\mathrm{B}}T_{\mathrm{e}}}=\frac{1}{1-\gamma}\sqrt{\frac{2E}{m_{\mathrm{i}}}} \tag{2.47}$$

$$E=\frac{k_{\mathrm{B}}T_{\mathrm{e}}}{2}+\frac{\gamma}{1-\gamma}\sqrt{\frac{m_{\mathrm{e}}}{m_{\mathrm{i}}}}\left(\frac{E}{e\phi_{\mathrm{w}}}\right)^{\frac{3}{2}}\left(\frac{k_{\mathrm{B}}T_{\mathrm{e}}}{2}-e\phi_{\mathrm{w}}\right) \tag{2.48}$$

At $\gamma = 0$, the Child-Langmuir solution for a fully absorbing floating wall is recovered, with $E = k_{\mathrm{B}}T_{\mathrm{e}}/2$ corresponding to the marginal validity of the Bohm criterion. As γ approaches a critical value near unity, the sheath potential decreases to the order of 1 T_{e} and the electric field at the wall becomes zero. The incoming ion energy increases somewhat above the Bohm value, but only to 0.58 $k_{\mathrm{B}}T_{\mathrm{e}}$. With the ϕ_{w} and E known, Poisson's equation can be integrated over the spatial coordinate from the wall into the plasma, giving the sheath potential profile.

The Hobbs and Wesson model stops when the electric field at the wall becomes zero, which is when the sheath potential has decreased to the order of 1 T_{e}. A comment in the original paper gives a description of what the authors expect will happen with still greater emission from the wall, which is that "the emission current would be limited by space charge." One could interpret this statement to mean that the minimum of the sheath potential will remain fixed at order of 1 T_{e} below the plasma potential: such an interpretation is implied in Figure 7-13 of the Goebel-Katz textbook [37].

2.3.4 Contemporary Theory

A full treatment of the emitting-wall sheath requires the removal of the assumption of negligible plasma electron loss to the wall and analysis of the electron populations kinetically rather than as fluids. Such an analysis has been accomplished in 2014 by Sheehan *et al.* [87]. He defines the emitted electron distribution as a half-Maxwellian with temperature T_{ee}, and finds that as that temperature increases, the sheath potential drops, becoming zero when T_{ee} is equal to the plasma electron temperature, T_{ep}. The model does not include sheath regions where the sheath potential reverses polarity to keep electrons towards the wall (virtual cathode and inverse sheath solutions), but if the model were extended to $T_{\mathrm{ee}} > T_{\mathrm{ep}}$, an inverse sheath would be the only solution to maintain the floating condition at the wall. This is the type of solution found in the fluid model of Campanell, who predicts the occurrence of an inverse sheath at high levels of electron emission [19].

2.3.5 Experimental Results

The new predictions of the inverse sheath regime have driven renewed research activity concerning the interaction of SEE and sheaths. Experiments using a thermionic emitting wall as an electron emission source were performed in the 1980's, and gave results qualitatively consistent with the Hobbs and Wesson theory [24, 47, 34].

Results of Intrator et al.

Intrator *et al.* performed a study in 1988 [47] to investigate the sheath over a grid of emitting tungsten wires. Their investigation found a system of two potential structures which the authors term a "virtual cathode" or a "transient double sheath". The system consists of a sheath structure on the normal length scale of a few Debye lengths, which goes from a normal electron-repelling sheath at no emission condition to an inverse electron-attracting sheath at the strong emission conditions. At strong emission

conditions, the second structure becomes active, which is a gradual electron-repelling slope over a much larger length scale (30-50 Debye lengths.)

The authors question how the two-sheath structure could be stable in steady state, reasoning that low-energy ions would become trapped in the potential well and their accumulated charge would repel incoming ions and eliminate the virtual cathode region. Their reasoning for the answer has to do with the way they heat the filaments. The authors employ 60 Hz half-wave rectified power pulses to heat the filaments and take data in the off-cycle when the filaments are a floating equipotential surface. However, during the on-state of the heating cycle, there is a voltage drop on the order of 20 V across the filament grid as it is heated, which the authors propose pumps slow ions out of the potential dip region (driving them parallel to the grid surface, along the direction of the voltage drop.) Through this ion pumping mechanism, they believe the double sheath structure is able to persist and show up in the measurement. To support this, they observe that as the neutral pressure is increased in the device, the potential dip structure decreases in magnitude until it has largely disappeared.

The recent dissertation of Sheehan [85] and a journal article by Li [63] have investigated virtual cathode structures forming as a result of SEE from the wall material. These structures raise new questions, as they occurred at much higher sheath potentials than predicted by the Hobbs and Wesson theory.

2.3.6 Effect of wall roughness

In thrusters, the conditions of the thruster wall evolve over the many thousands of hours of operation due to ion bombardment and prolonged plasma heating. As such it is of interest to learn how changes in the thruster wall surface and microstructure may impact the sheath, and thus the operation of the thruster over its lifetime.

The primary mode of coupling between the wall and plasma is believed to be through SEE. Given that the dependance of SEE yields on incidence angle generally

shows increased yield for non-normal incidence angles of 30° to 60°, it would seem that a roughened wall would have higher SEE yield than a smooth wall. On the other hand, it can be argued that a roughened wall will in general have lower secondary electron emission than a smooth wall, due to geometrical obstruction of emitted electrons by the peaks of the rough surface. In the extreme case, this mechanism holds true, as shown by yield measurements by Raitses *et al.* using carbon velvet materials that consist of "forests" of carbon nanotubes. The total electron yield of these materials was measured to remain quite low regardless of incident energy, never exceeding 0.1. It is unknown whether the geometric trapping mechanism used by the velvet will work in a material with a more macroscopic peaks-and-valleys type of surface profile. There is thus a need for experimental investigation of the effect of surface roughness on the sheath in conditions with significant secondary electron emission.

2.3.7 Effect of wall temperature

The energy stored in a solid wall material is largely contained in the lattice vibrations of the material, however some of the energy is stored in the internal "free" electrons that move throughout the material. When the work function is low, it is these electrons which have enough energy to escape the surface by thermionic emission as described by Richardson's Law (2.46). As discussed, this emission (which depends exponentially on wall temperature) can have a large effect on the plasma sheath. Even for materials with high work functions, there are several ways in which the wall temperature may have an indirect effect on the sheath:

- The wall temperature will govern the temperature of neutral gases colliding with the wall, so high wall temperatures will have the effect of decreasing the near-wall neutral density and making the sheath more collisionless.

- Wall temperature has been identified as a factor that effects the reproducibility of electron emission experiments, and electron emission is known to strongly effect

the sheath as previously discussed. Experiments seeking to measure electron emission from solid samples typically perform a heating / desorption procedure at the beginning of the experiment to free the surface of adsorbed gases and contaminants. The presence of adsorbed gases and contaminants increases the observed electron emission.

- Temperature affects electrical resistivity in solids, which may affect the generation rate of true secondary electrons. In metals, resistivity increases with increased temperature; in semiconductors and insulators, resistivity decreases with increased temperature.

- Depending on the temperature stability of the wall material, high wall temperatures may change the surface microstructure and thus couple with the effects of surface roughness.

Given these factors, there is a need for experimental investigation of the effect of wall temperature on the sheath potential profile. This author is unaware of any study yet that has done this.

2.4 Influence of Magnetic Field

Applied magnetic fields can give rise to a wide variety of plasma phenomena. At the level of the charged particles of the plasma, the effect in the plane perpendicular the field lines is to restrict charged particles to circular motion ("gyromotion") due to the $\vec{u} \times \vec{B}$ component of the Lorentz force. The radius of the trajectory of a given plasma species α is the species' Larmor radius or gyroradius:

$$r_{g\alpha} = \sqrt{\frac{m_\alpha u_{\perp\alpha}}{q_\alpha B}} \tag{2.49}$$

where $u_{\perp\alpha}$ is the speed of species α parallel to the magnetic field. It can be seen from equation (2.49) that electrons can be restricted by magnetic fields ("magnetized") with

much lower applied fields than ions due to their lower mass. The motion parallel to the field is not impeded, giving the trajectories of charged particles in magnetic fields a helical shape.

Due to gyromotion, magnetic fields in plasmas have the effect of hindering electron transport perpendicular to the field lines, but not parallel to them. Transport perpendicular to the field lines still occurs, due to collisions, plasma fluctuations, wall termination, or possibly other unidentified mechanisms – Hall effect thrusters rely on such mobility to sustain the discharge. Accurately predicting the cross-field electron mobility is one of the main limitations in current Hall effect thruster modeling codes.

Magnetic fields have been found to be highly useful for electric propulsion devices, for reducing power losses to the thruster wall and for limiting electron mobility from the discharge plasma to the anode. Magnetic cusp geometries are commonly used to decrease wall losses in ion engine discharge chambers. In Hall effect thrusters, the magnetic field has a strong radial portion near the exit plane of the thruster to trap electrons in the annular Hall current. The magnetic field can also be shaped to not intersect the discharge channel wall near the exit plane, the "magnetic shielding" configuration which avoids rapid erosion of the discharge channel wall [43]. All in all, the intersection of wall interactions and magnetic fields is of great interest for thruster development.

2.4.1 Sheath theories incorporating magnetic field

The fundamentals of the effects of a magnetic field with arbitrary orientation with respect to the wall on the plasma sheath are due to Chodura [22]. He concludes that the sheath will organize into a quasineutral "magnetic presheath" that scales with the length scale $u_{\mathrm{a}}/\Omega_{\mathrm{i}}$, where u_{a} is the ion acoustic speed (equal to the Bohm speed (2.35)) and Ω_{i} is the ion gyrofrequency.

The Chodura theory was extended by Ahedo [4] to join with the unmagnetized

presheath theories of Riemann and describe the transitions between the regimes. Ahedo also treats the case of a strong magnetic field, where the ion gyroradius and the plasma Debye length are of similar dimensions.

2.4.2 Experimental Results

Experiments in 1995 by Kim *et al.* [51] support the Chodura structure of the magnetized presheath potential profile. Experiments by Takamura *et al.* [90] show a significant decrease in sheath potential of gold and tungsten targets as the magnetic field is transitioned from normal- to grazing-incidence, although full measurements of the sheath potential profile were not obtained. To the author's knowledge, no experiments have tested the predictions of the strong magnetic field case of the Ahedo model, in which the effect of the magnetic field is predicted to extend from the presheath region into the actual sheath region.

2.5 Application of Sheath Theory

In the analysis of a bounded plasma, the sheath forms at all surfaces in contact with plasma and has important effects on the particle and energy transport between the plasma and the wall. In a typical floating wall sheath, the sheath assumes a thickness and electric field strength proportional to the plasma parameters. The wall potential floats negative with respect to the plasma potential and the sheath acts to accelerate ions into the wall and repel electrons from the wall. This gives the floating sheath an intrinsic role of thermal insulation for the wall, shielding the wall from the large heat flux it would otherwise receive from the energetic free electrons of the plasma. It does this at the expense of subjecting the wall to a more energetic ion bombardment than would otherwise be the case. In the first subsection we discuss some aspects of sheath scaling for different plasmas. We will analyze in more detail the particle and energy transport between the plasma and wall. Following that, we give some discussion of how sheath models are implemented in a common Hall effect thruster model.

2.5.1 Sheath Scaling

In all the sheath theories presented so far, the sheath potential has been nondimensionalized using the electron temperature and the spatial coordinate has been nondimensionalized using the Debye length. This is a powerful formulation in that it allows the sheath theory to be applied to a plasma of any given number density and temperature.

The Child-Langmuir sheath and collisional presheath thickness scaling has been verified at low plasma densities by Lee and Hershkowitz [72]. The EP community has thus far assumed that this scaling allows the sheath models to be used in thrusters without correction. However, the floating potentials predicted by the emitting wall theories of Sheehan, Campanell, and Ahedo have not been experimentally verified. This is particularly important for Hall effect thruster design in particular because the floating potential of the dielectric discharge channel influences power losses and attainable plasma density.

2.5.2 Particle and Energy Fluxes

The loss rates of particles and energy to the wall through the sheath are a part of the equilibrium condition of the plasma that determines its global temperature and number density, thus in general, plasma-wall interaction cannot be accurately analyzed separately from the overall plasma – the plasma-wall interaction and the bulk plasma equilibrium are coupled. However insight can be gained from considering a case where the two are decoupled.

Consider a flat plate electrode placed in an electron-ion plasma. We will say that the plasma is infinitely large and unperturbed by the bias and/or current collection of the electrode, and the SEE, thermionic electron emission, and ion reflection from the wall are low enough to be neglected. Thus the electrode acts as a fully absorbing wall and we can change the bias of the electrode with respect to the plasma potential,

which remains unperturbed.

For a given sheath theory it is feasible to predict the particle and energy transport for the varied bias of the electrode. We will assume a Child-Langmuir sheath with Bohm presheath, with a Maxwellian plasma of electron temperature T_e and negligible ion temperature. For working with energies and fluxes, we will define a non-dimensionalized energy, particle flux, and energy flux as follows

$$\epsilon_\alpha = \frac{E_\alpha}{eT_\mathrm{e}} \tag{2.50}$$

$$\Xi_\alpha = \frac{\Gamma_\alpha}{\frac{1}{4}n_0 u_\mathrm{e}} \tag{2.51}$$

$$\delta_\alpha = \Xi_\alpha \epsilon_\alpha \tag{2.52}$$

in which $\bar{u_\mathrm{e}} = \sqrt{\frac{8eT_\mathrm{e}}{\pi m_\mathrm{e}}}$ is the mean electron speed entering the sheath, the dimensionless energy ϵ is normalized to the plasma electron temperature, the dimensionless particle flux Ξ is normalized to the free electron thermal flux, and dimensionless energy flux δ is the product of the two.

First let's consider the case where the wall potential is biased below the plasma potential. The flux of ions to the wall is equal to the flux entering the sheath at the Bohm speed, which is

$$\Gamma_\mathrm{i} = n_0 u_\mathrm{B} \tag{2.53}$$

where n_0 is the ion density at the sheath edge. Normalized, it is

$$\Xi_\mathrm{i} = 4\frac{u_\mathrm{B}}{\bar{u_\mathrm{e}}} \tag{2.54}$$

The ratio of the Bohm speed to the mean electron speed can be expressed in terms of the mass ratio of the plasma ions to electrons $\mu = m_\mathrm{i}/m_\mathrm{e}$.

$$\frac{u_\mathrm{B}}{\bar{u_\mathrm{e}}} = \frac{\sqrt{\frac{eT_\mathrm{e}}{m_\mathrm{i}}}}{\sqrt{\frac{8eT_\mathrm{e}}{\pi m_\mathrm{e}}}} = \sqrt{\frac{\pi}{8\mu}} \tag{2.55}$$

$$\Xi_\mathrm{i} = \sqrt{\frac{2\pi}{\mu}} \tag{2.56}$$

The electron flux in this case is the thermal flux from the Maxwellian as repelled by the sheath potential

$$\Gamma_{\mathrm{e}} = \frac{1}{4} n_0 u_{\mathrm{e}} \exp\left(-\Phi\right) \tag{2.57}$$

or when normalized,

$$\Xi_{\mathrm{e}} = \exp\left(-\Phi\right) \tag{2.58}$$

where Φ is the sheath potential normalized by the electron temperature as defined in equation (2.18). The energy transferred by the ion and electron fluxes are their respective fluxes multiplied by the energy transferred per particle. The ions are accelerated in the sheath and gain energy, thus their ultimate energy is related to the sheath potential as

$$\epsilon_{\mathrm{i}} = (\frac{1}{2} + \Phi) \tag{2.59}$$

The constant term of $1/2$ in equation (2.59) is due to the energy possessed by the ions by virtue of entering the sheath at the Bohm speed. The energy deposited in the wall by the electrons that make it through the sheath varies from electron to electron. The plasma electrons are assumed to have a Maxwellian energy distribution defined by the temperature T_{e}, thus only the particles with sufficient energy to cross the sheath potential can make it to the wall. This is often the high-energy "tail" of the distribution. Integrating across the Maxwellian distribution, it can be shown that the electrons deposit on average an energy of twice the electron temperature in energy units (Goebel-Katz [37] appendix C.)

$$\epsilon_{\mathrm{e}} = 2 \tag{2.60}$$

We can thus calculate the energy flux from the plasma to the wall as a function of the bias potential Φ.

$$\delta = \delta_{\mathrm{e}} + \delta_{\mathrm{i}} = \epsilon_{\mathrm{e}} \Xi_{\mathrm{e}} + \epsilon_{\mathrm{i}} \Xi_{\mathrm{i}} = 2 \exp\left(-\Phi\right) + \sqrt{\frac{2\pi}{\mu}} \left(\frac{1}{2} + \Phi\right) \tag{2.61}$$

Figure 2.10 shows the dependence of the energy transfer coefficient δ on the wall electrode bias Φ below the plasma potential for several different ion species. The

dotted line in Figure 2.10 shows δ at the floating potential as a function of ion mass. A minimum occurs in the energy transfer δ near to the floating potential. This is one reason why the floating boundary condition is often attractive for plasma devices – it requires no active circuitry and yet ends up near to the minimum energy transfer in the nominal case.

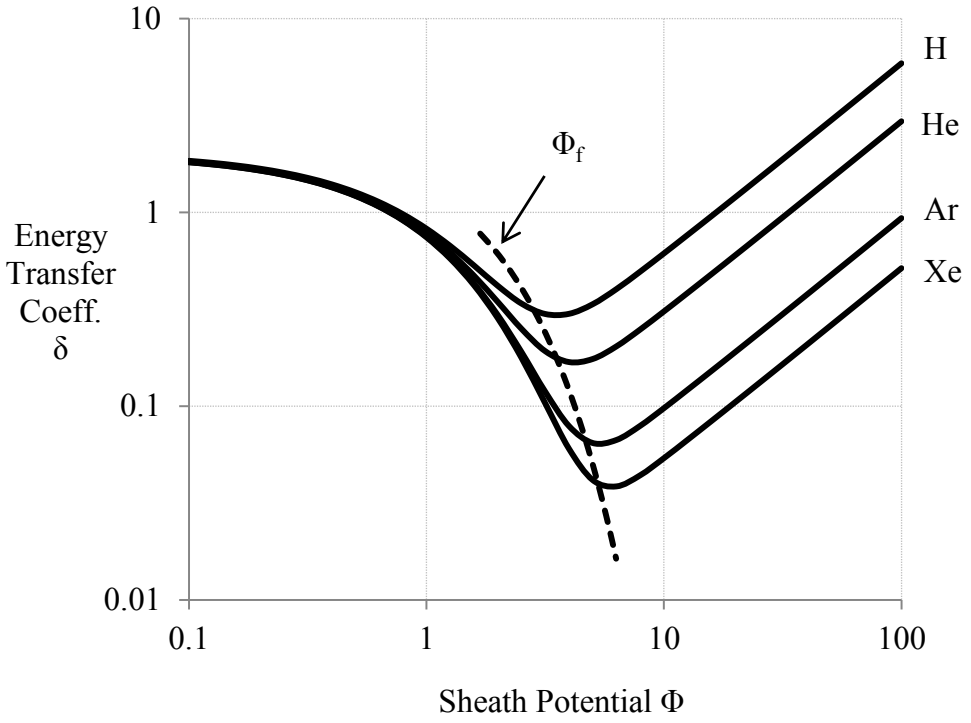

Figure 2.10: Dependence of energy transfer coefficient δ (equation 2.61) on the normalized sheath potential Φ below the plasma potential for plasmas of several different singly-charged ion species. Φ_f dashed line denotes the Child-Langmuir floating potential variation with ion mass/charge ratio.

As shown in Figure 2.10, plasmas formed with heavy ion species are in a sense intrinsically advantageous for minimizing energy transport to the wall. The reason is twofold. First, the large imbalance in mass between the electrons and ions will create a relative large floating sheath potential, which helps to repel the electrons from the wall and contain their energy within the plasma. Second, the Bohm speed decreases with the square root of the ion mass, which causes the total ion flux to the wall to decrease for heavier ions and thus in the floating condition causes the total electron

flux to the wall to decrease.

The ions can impart significant energy to the wall if the negative bias is large. If the wall is biased very strongly negative into the range of 100's of electron temperatures, the kinetic energy of the ions begins to equal or exceed what the electron thermal flux would have delivered. Also, because the ions probably have comparable mass to the atoms of the wall material, there may be significant atomic sputtering and erosion of the wall material at these high ion energy conditions.

Examining Figure 2.10 for the case of a xenon or argon plasma, it can be seen that if the sheath potential collapses from the Child-Langmuir floating potential to $\Phi \approx 1$ as predicted by the Hobbs-and-Wesson theory for an electron-emitting boundary, it will give rise to a significant increase in the energy flux to the wall. Some indication of this effect has also been observed experimentally: experiments by Takamura *et al.* with a tungsten surface showed an abrupt loss of sheath potential coupled with a significant increase in wall temperature [91]. The floating potential falls by about 30 V and the target wall temperature increases from 2500 K to 3100 K, indicating an increase in heat flux by at least a factor of 2.3 considering that the radiative heat transfer from the wall sample will vary as T^4 and neglecting any other heat transfer paths.

From the analysis in the section, we see that the sheath voltages that manifest at plasma boundaries can have a significant effect on particle and energy transport between the plasma and wall. The next section gives more detail about one of the most widely used Hall effect thruster models "HPHall" and its application of analytical sheath theory.

2.5.3 Modeling Example: HPHall

Analytical sheath theories are often used directly in modeling thruster plasmas. As previously mentioned, sheaths are very thin in thruster plasmas on the order of tens

of micrometers, so it is computationally expensive to generate a mesh on the order of the Debye length to resolve the sheath region. It is expedient to input an analytical sheath model as a boundary condition at the model edges representing the electrodes and discharge channel walls.

One of the first Hall effect thruster models to become widely used in the US was HPHall, written in 1990 by Fife and Martinez-Sanchez [31]. It represents the plasma electrons as a fluid and the plasma ions using the PIC method. In the PIC method, the particles are defined as a number of "macroparticles" each representing perhaps 10^7 real particles and forces are calculated by summing the contributions of neighboring cells of a predefined grid throughout the plasma. The method of only using PIC for the ions, called hybrid-PIC, saves computational effort in comparison to full-PIC (wherein the PIC method is used for both electron and ion populations.)

In HPHall, a sheath model is selected and implemented directly as the wall boundary condition for cells touching the wall. The original sheath model of Fife and Martinez-Sanchez was uncommon for its time, and greatly resembles the recent predictions of the inverse sheath of Campanell. The sheath model is of significant importance to the predictions of the model, because it mediates the loss rates of ions and electrons to the wall, the energy with which they strike, and the rate of secondary electron flux returning from the wall. These in turn influence the steady-state plasma density, electron temperature, and predicted wall erosion rate, which in turn strongly effect the predicted performance.

Several changes have been made to HPHall over the years, creating new variants HPHall2 [74], HPHall2-JPL [44]. Agreement remains semi-empirical, with parameters of the electron fluid requiring arbitrary adjustment to match experimental data. In one of the updates, the sheath model was changed from Fife's model to the Hobbs and Wesson model [45]. Now the new theories of Campbell and Sheehan raise the question if the theory should be changed again. This underscores the need for experimental

measurements of emitting-wall sheaths.

CHAPTER III

RESEARCH GOALS

In the previous chapter, we discussed the current state of knowledge about plasma sheaths in several areas, namely the scaling of sheaths, the presheath-sheath transition, electron emission from the wall, wall temperature, wall topology and surface roughness, and applied magnetic field. In this chapter, we discuss the selection of scope for the current work.

3.1 Experimental Approach

In order to ground some of the theoretical development of sheath theory, it is desired to obtain experimental measurements of sheaths. To do this *in situ* in thrusters poses a significant challenge: the plasma density is high in thrusters and sheaths are thin, on the order of micrometers. Due to the scalability and dimensionless formulation of the sheath theories, it is feasible to examine the physics in a nominal plasma environment with a lower plasma density. This is the approach taken in the current research.

While there is value in purely exploratory sheath measurements given the low amount of experimental data on sheaths, the space of possible investigations is broad and it is necessary to have some scope of things to study. Dr. Hershkowitz's group has done extensive work in illuminating the physics of Child-Lanmguir sheaths and the presheath-sheath transition / Bohm criterion, extending this investigation into multiple-species plasmas and examining the effect of ion-ion acoustic instabilities. In this work, we will primarily pursue the effect of electron emission from the wall, along with confounding influences that may be present such as wall roughness and wall temperature. This will allow us to address the thruster-relevant possibility for a large effect on the sheath potential and energy flux. The following are specific research

questions to be pursued:

3.1.1 Electron emission from the wall

- Is the Hobbs and Wesson theory an accurate description of the sheath over an electron-emitting wall? Should it be expanded/replaced in thruster models with the Campanell or Sheehan theory? Are more general theories needed?

3.1.2 Wall roughness

- What are the effects of wall roughness on the plasma sheath potential profile in conditions of significant electron emission?

3.1.3 Wall temperature

- What are the effects of wall temperature on the plasma sheath potential profile in conditions of significant electron emission?

Experiments were designed and attempted to determine the effect of applied magnetic field, but have not yet yielded useful results. Ultimately it became clear that the application of magnetic field introduced too many new experimental challenges, and thus it is not included in the scope of the present research.

CHAPTER IV

EXPERIMENTAL APPARATUS

4.1 Plasma Cell

The main difficulty in experimental measurement of sheath potential profiles is their small physical size (tens of micrometers for the thruster plasma.) In order to circumvent this difficulty, a low-density plasma cell has been designed and built to create plasma sheaths on a measurable scale. The device is based on an established design from literature, originally reported by Limpaecher and Mackenzie [65] in 1973. Studies done by Leung *et al.* investigated the effect of different configurations of the magnetic boundary [61, 62] and by Lang and Hershkowitz to assess achievable plasma densities [55]. The device has been widely used since, notably by Hershkowitz and collaborators. A schematic of the device as built and used in the present experiments is shown in Figure 4.1. Plasma is generated by collisional ionization of neutral gas from energetic electrons, which are emitted from heated tungsten filaments. The energetic electrons are confined using cusp magnetic fields at the plasma boundary which increases the uniformity of the plasma within the volume. The cusp magnetic fields decay rapidly (as $1/r^3$) away from the permanent magnet dipoles around the boundary, so the main plasma volume of the device is unmagnetized.

In the present work, the device is operated at low discharge current and plasma density together with high energetic electron fraction. Energetic electron populations can have a large effect on sheaths over floating walls even at fairly low fractions, due to the fact that only the highest energy electrons make it through an electron-repelling sheath to impact the wall. This operation at high electron energy leads to high SEE yields from the wall and enables the experimental study of the emitting wall sheath

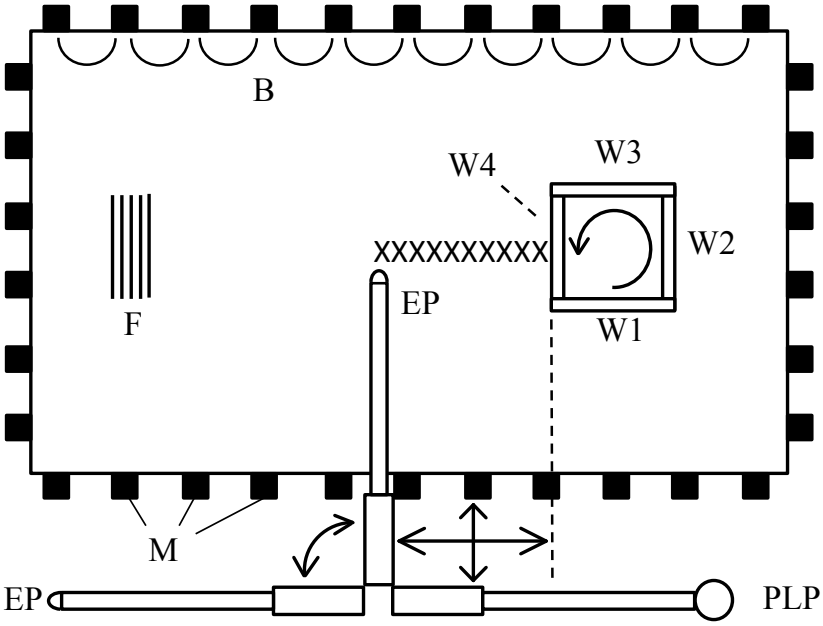

Figure 4.1: Diagram of plasma cell and diagnostics. F = filaments, M = magnets, B = nominal magnetic field, PLP = planar Langmuir probe, EP = emissive probe, W = wall material sample, X = nominal data measurement location. Emissive probe orientation rotated 90° in figure to show hairpin tip geometry. Not to scale.

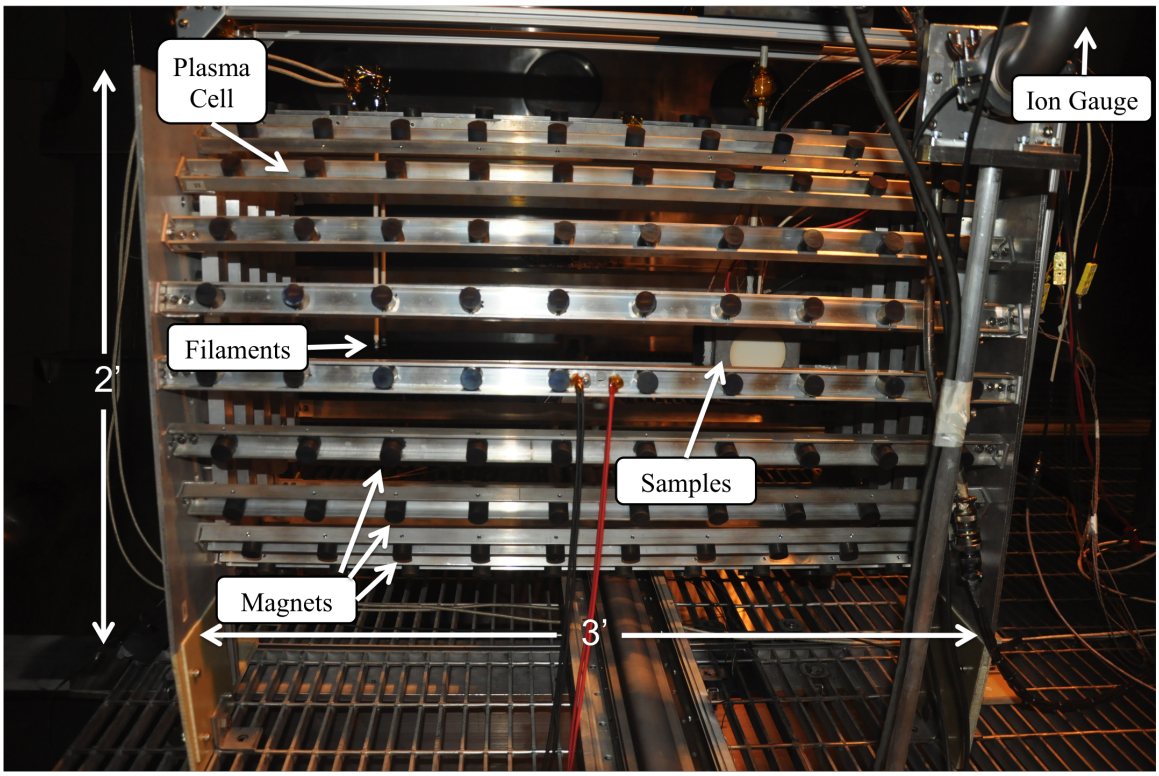

Figure 4.2: Photo of plasma cell installed in chamber.

regimes.

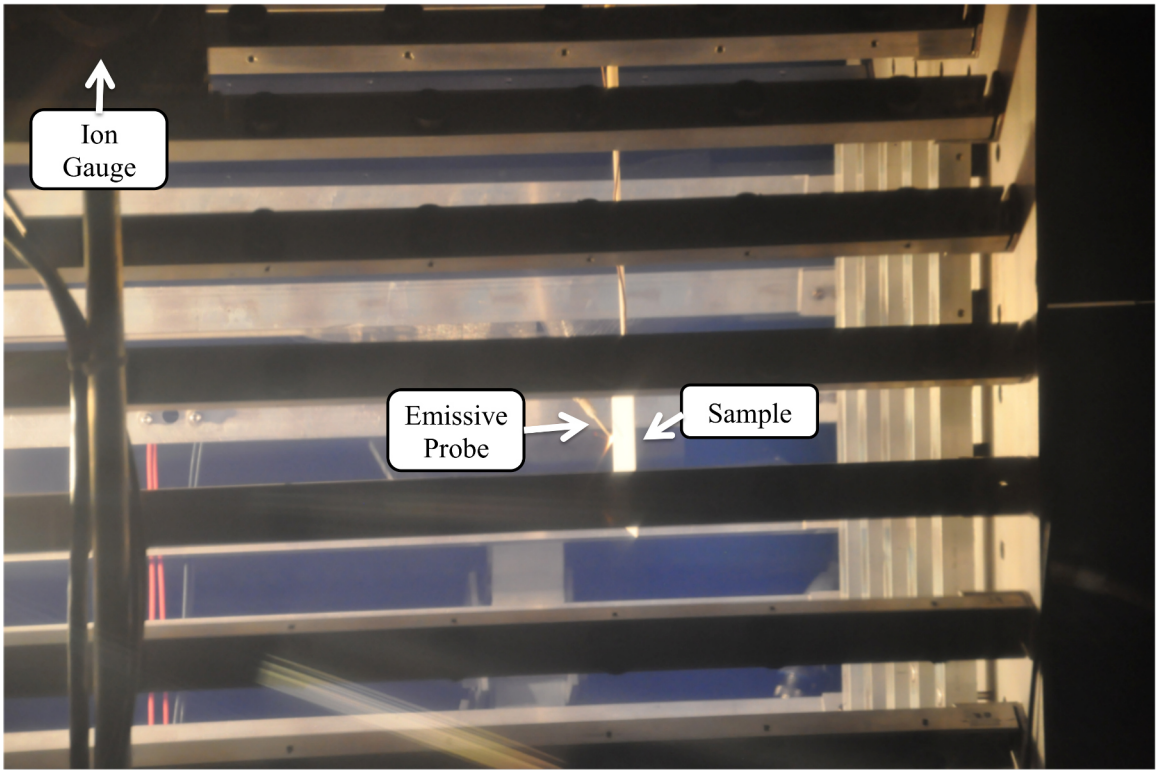

Figure 4.3: Plasma cell operating at 5 A discharge current to get a visible plasma. Most data is collected at lower discharge currents, where the plasma is not visible.

There are several aspects of multidipole device design that can be varied, with various effects on the plasma operation. In the following sections, those issues are discussed and the choices made in the device used for these experiments are noted.

4.1.1 Ionization Source

In theory, a multidipole plasma device can operate using any type of ionization source. The only necessity is to inject energized particles or plasma into the device, and allow them to diffuse throughout the confinement volume. Many sources in literature have used heated thoriated tungsten filaments, this is also the technique used in the present device and experiments. The filaments are heated to incandescence by passing electric current through them, and thermionic electrons are extracted and accelerated into the device by application of a separate discharge voltage between the filaments and

the device frame. The electrical schematic is shown in Figure 4.4.

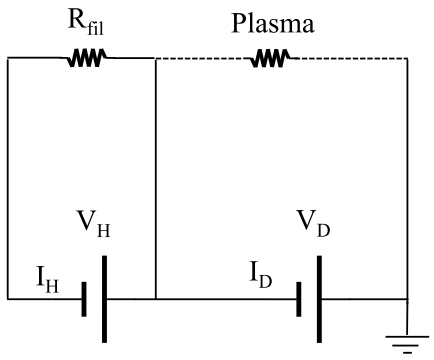

Figure 4.4: Electrical schematic of multidipole plasma cell operating with hot-filament ionization source.

The nomenclature in Figure 4.4 is the nomenclature that will be used for reporting the experimental data: the heating voltage and current V_{H} and I_{H} and the discharge voltage and current V_{D} and I_{D} are recorded using the analog monitoring interface from the respective power supplies.

The spatial position of the filaments also has an influence on the device operation. In particular, it matters whether the filaments are located near the device wall and within the boundary magnetic field, or if they are within the unmagnetized region in the middle of the device. If the filaments are positioned within the boundary magnetic field, the energetic electrons emitted from the filaments will be confined within the exterior magnetic field and be largely absent from the plasma resulting from ionization that diffuses into the center of the device. If the filaments are located in the unmagnetized region in the middle of the device, the energetic electrons will be reflected inside the plasma device, and will exist throughout the plasma volume along with the rest of the plasma resulting from ionization. For these experiments, the filaments are positioned inside the device in the unmagnetized region, which allows the energetic electrons to be present in the experimental plasmas and drive SEE from the wall material samples.

4.1.2 Vacuum Environment

Happily, a large vacuum chamber is available for performing the experiments with the plasma cell, so there is no requirement that the plasma cell constitute its own vacuum vessel. The vacuum chamber used is the Georgia Institute of Technology Vacuum Test Facility-2, which is 9.2 meters long, 4.9 meters in diameter and uses ten PHPK TM1200i cryopumps to achieve a base pressure of 2 x 10^{-9} Torr. Only two of the cryopumps are operated during the plasma cell experiments, in order to decrease pumping speed so that the desired experimental pressures can be obtained using a 500 sccm-N_2 range MKS 1179A01352CS1BV mass flow controller. This results in base pressure of 1 x 10^{-8} Torr obtained for these experiments. The mass flow controller is used to flow 99.999% argon into the chamber and control the operating pressure.

4.1.3 Neutral Flow and Operating Pressure

The pressure of neutral gas within the chamber and plasma device influences the achievable plasma density and the amount of electron-neutral collisions within the plasma. It is known that the molecular flow of low-pressure gases in vacuum chambers can establish significant differences in pressure at different locations throughout the chamber [99]. In these experiments the plasma cell is positioned in the center of the chamber, far (2-3 meters) from the gas inlet and active cryopumps, so as to be in a region of relatively uniform neutral pressure. The device is a series of rails supporting the magnets rather than an enclosed cylinder, in order to allow neutrals to readily diffuse into the interior of the plasma cell. The arrangement of the plasma cell and pumps / gas inlet is shown in Figure 4.5. The neutral pressure reported in these experiments is measured by a Bayard-Alpert 572 ionization gauge next to the plasma cell in the center of the chamber. Also available are measurements from a Bayard-Alpert 571 ionization gauge connected to the side of the chamber, which showed the same trends with pressure as the interior gauge but reported roughly 20%

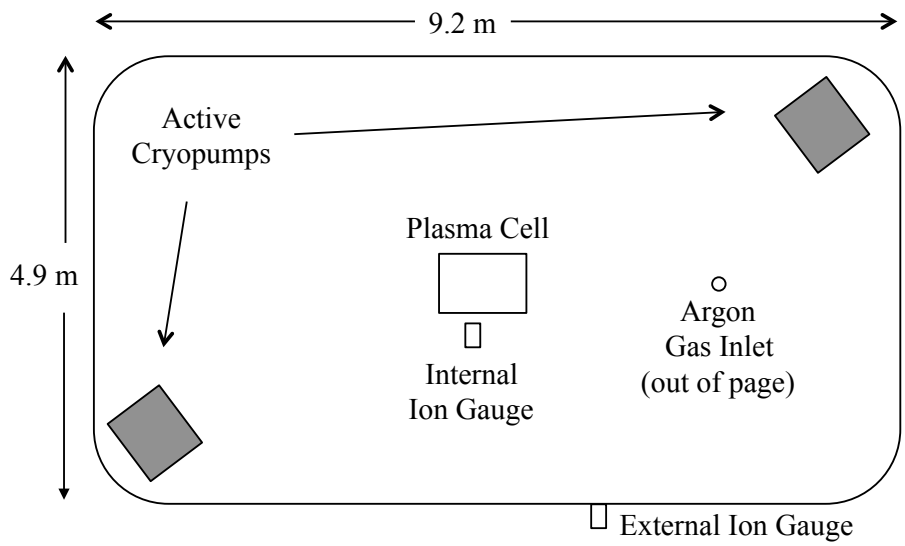

Figure 4.5: Arrangement of the plasma cell, pumps activated and gas inlet installed in GT HPEPL VTF-2.

lower pressure reading at any given flow rate. The disagreement could be due to pressure gradients in the chamber, but given that the accuracy of the gauges is ± 25% [94], it could also be due to measurement error of the gauges. For reporting the experimental data, the reading of the interior gauge next to the plasma cell is given as the nominal reading.

4.1.4 Construction Details

As built, the plasma cell cylindrical cage interior length is 36 inches and the interior diameter is 24 inches. There are 24 rails of 1/8-inch thick aluminum u-channel that form the exterior of the cylindrical cage, each lined with 11 Magnet Kingdom CM-0411 ceramic permanent magnets. The magnets are all oriented with the same polarity on each rail with adjacent rails assigned opposing polarities – the 'broken line cusp' configuration described by Leung *et al.* [61]. The magnets are equally spaced 3.5 inches apart on center along the rails. The end plates are 24 inch aluminum squares, 1/4 inch thick, with 1/2 inch holes drilled in a 1.725-by-3.175 inch grid to allow neutral gas flow into the plasma region. A grid of similarly spaced and polarized magnets is

held on the interior of the each of the end plates with u-channel.

Five 2% wt. thoriated tungsten filament lengths of 2.5 inch and diameter 0.006 inch are resistively heated in parallel to generate the electrons that create the plasma. The filament lengths are formed from a continuous length of filament wound between two 8-32 stainless steel threaded rods spaced 2.5 inches apart and clamped by small pattern stainless steel machine nuts, as shown in Figure 4.6. The threaded rods are

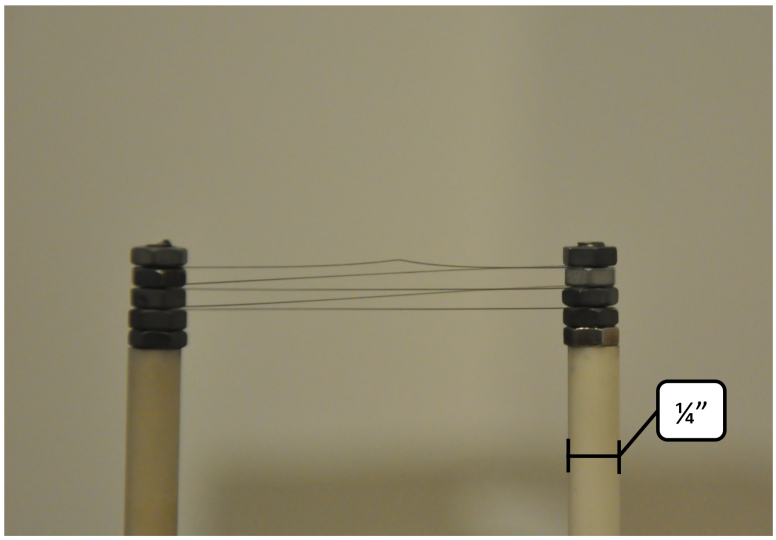

Figure 4.6: Photo of filament winding, threaded-rod supports and alumina tubing insulators.

electrically isolated from the rest of the plasma cell frame using 1/4 inch OD alumina tubing and used as both the filament electrical leads and structural supports.

4.1.5 Installation Details

When installed in VTF-2, the plasma cell sits on garolite G10 feet that elevate its base 6 inches above a stainless steel personnel grating supported by a central I-beam and two flanges on the sides of the chamber. The axis of the plasma cell cylinder is aligned with the chamber axis and the I-beam. In order to permit horizontal access for probe diagnostics, the plasma cell feet are cut to clock the plasma cell clockwise at a 7.5° angle.

4.2 Diagnostics

4.2.1 Diagnostic Selection: Optical vs. Probe Diagnostics

Plasma diagnostics can be broadly characterized as either physical probe-based diagnostics, optical diagnostics, or magnetic diagnostics. The latter category is not effective for unmagnetized plasmas, so the choice for the present experiments was mainly between probe-based diagnostics and optical diagnostics.

Physical probe-based diagnostics involve inserting an additional electrode into the plasma, and determining information about the plasma by the electrical response of the probe to various applied voltages and signals. The most straightforward example of a probe diagnostic is the Langmuir probe, which dates back to Langmuir's original research in the early 1900's. In theory, a Langmuir probe can measure almost all of the information of the plasma at the spatial location where it is positioned and swept. Standard interpretation of a Langmuir probe data returns the plasma ion number density, electron temperature, and plasma potential [40]. With further considerations and high-fidelity data, Langmuir probes can be used to measure the electron energy distribution function of the plasma in non-Maxwellian plasmas [6].

The downside of Langmuir probes is that the correct interpretation of the data is non-trivial and the selection of the proper interpretation theory depends on the plasma parameters to be measured [28]. To combat this difficulty, a large number of variant electrostatic probes have been developed for specific plasmas and applications, which generally do not measure as many plasma parameters as the Langmuir probe but deliver increased accuracy and robustness on the parameter that they do measure. A notable probe variant that has been used in sheath research is the emissive probe, which is able to deliver a robust measurement of plasma potential.

A disadvantage of physical probe-based diagnostics is that the very act of inserting another physical electrode into the plasma intrinsically perturbs the plasma. This introduces the concern that you may not measure the true system as it would exist

without the probe, you measure a different system that includes the probe. To apply probe diagnostics and obtain results of sufficient accuracy, the probe must represent a "small perturbation" to the plasma. Typically this can be achieved by miniaturizing the probe electrode and support with respect to the plasma size. In plasmas where the majority of the boundaries are insulating / electrically floating, the current collection by even a very small probe may constitute a large perturbation to the system! Physical probes are also difficult to apply in high-density plasmas, as the high heat fluxes from the plasma to the probe may cause the probe to melt or emit electrons thermionically.

To circumvent some of the difficulties of physical probe-based diagnostics, optical plasma diagnostics have been developed. These often involve application of lasers, spectroscopy, and/or interferometry. Notable examples include Laser-induced fluorescence (LIF) [83, 84], Laser-collisional-induced fluorescence (LCIF) [46], Rayleigh, Raman, or Thompson scattering [96], and Microwave/Terahertz interferometry [71, 49]. These techniques avoid the insertion of physical objects and electrodes into the plasma and thus are generally less intrusive and perturbative than physical probes.

After reviewing these diagnostic options, it was decided that most optical techniques would be very difficult to apply successfully in the plasma sheath region where charged particle number densities are low. There would be very low signal for spectroscopy or interferometry techniques, which are largely applicable to higher density plasmas. Therefore it was determined to use emissive and Langmuir probes, which would be relatively easy to apply in the low-density plasma cell and should return reliable data.

4.2.2 Langmuir Probe

The collection of particles by a Langmuir probe depends on the probe tip geometry. The three most-studied tip geometries are the spherical probe, planar disc probe, and cylindrical probe. As discussed by Demidov *et al.* [28], a critical parameter is the ratio of the probe diffusion length scale to the plasma Debye length / sheath length

scale. The probe diffusion length is close to the probe physical dimension, which is the sphere radius, disc radius, or cylinder radius respectively.

Cylindrical Probe

The cylindrical probe was first selected to use for measurements of plasma density and electron temperature in the bulk plasma. The probe radius was 0.0025 inches, much less than the plasma Debye length, so it was thought that the orbital-motion-limited (OML) theory would be easily applicable, as this theory assumes large sheath thickness relative to the probe radius. However as shown in Figures 4.7 and 4.8, the ion current characteristics collected showed a linear dependence on V, rather than $\sqrt{V}$ as predicted by OML theory.

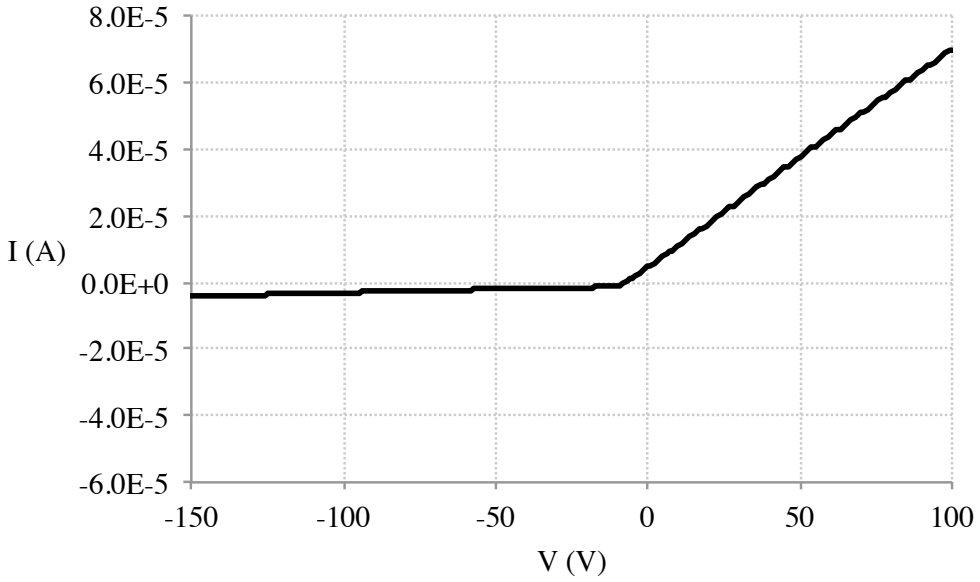

Figure 4.7: Sample data from cylindrical Langmuir probe in plasma cell at 10 mA discharge current.

Attempts to interpret the cylindrical Langmuir probe data gave reasonable electron temperatures (which should not depend on the probe geometry) but inaccurate number densities. On further reading and analysis, it was determined that the likely cause of the inaccuracy in number density is insufficient axial length of the probe, which is

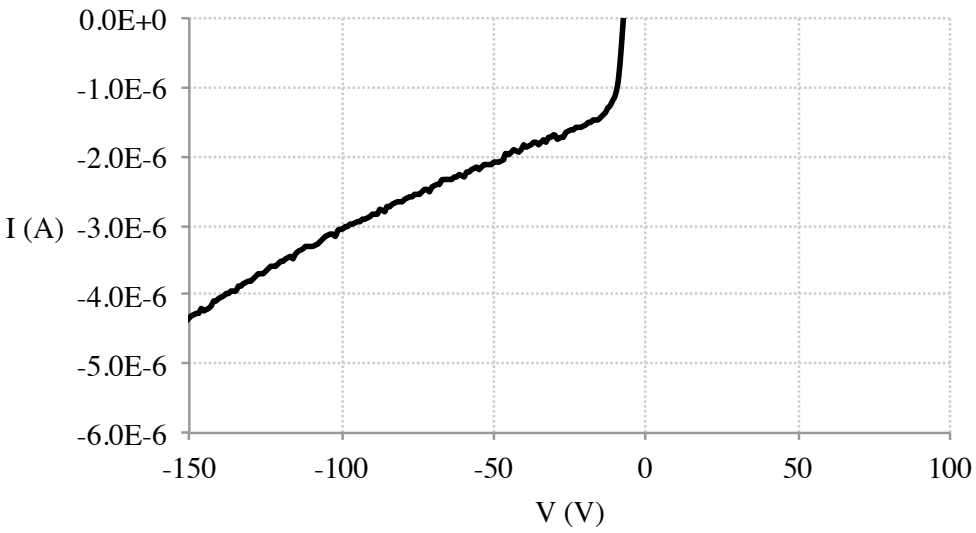

Figure 4.8: Sample data from cylindrical Langmuir probe in plasma cell at 10 mA discharge current (magnified to show ion current collection.)

required to be large compared to the Debye length. Instead of a lengthened cylindrical probe, it was determined to switch to a planar disc probe for better resolution of high-energy electron populations.

Planar Disc Probe

Planar disc probes are often used to determine an "ion saturation current" to the planar probe, from which the density can be determined using the conclusion from presheath theory that ions enter the planar sheath of the probe at the Bohm speed. The term "ion saturation current" is not precise, because the ion current continues to increase as the probe is biased negative, due to edge effects in the (Child-Langmuir) sheath expansion.

The planar geometry has the advantage of acting as a predominantly-1D energy discriminator for electrons and ions. Theory established by Knapmiller *et al.* [53] and Hershkowitz *et al.* [41] allows for relatively straightforward determination of electron energy distribution characteristics. The latter theory is particularly applicable to multidipole plasmas, showing how a linear characteristic in the electron-repelling

ion-collecting region corresponds to collection of isotropic energetic electrons. Such electrons can be present in multidipole plasmas due to energetic electrons emitted from the filament that make multiple bounces off the magnet cusps, and thus retain their energy from the cathode sheath but have effectively lost their directionality.

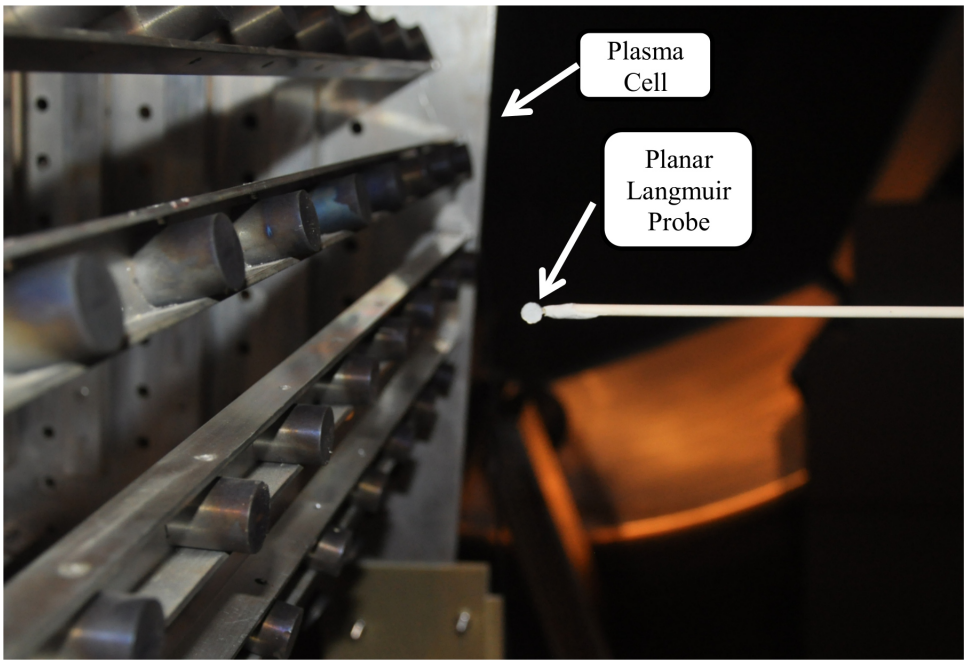

Figure 4.9: Photo of planar disc Langmuir probe as built, mounted to linear motion stage for insertion into the plasma cell.

Langmuir Probe Operation

The Langmuir probes used in this work are biased with a Keithley 2410 Sourcemeter. The Sourcemeter also measures the current emitted and collected by the probe. Linear stair-step voltage sweeps are configured on the Sourcemeter with the number of power line cycles (NPLC) for the dwell time of the sweep set to 1, so the dwell time is 13 ms for the 60 Hz power cycle. The resistance of the coaxial cable connecting the probe tip to the Sourcemeter is about 1.2 Ω and the current collected is in the range of microamps to milliamps, so the difference between the probe tip voltage and bias voltage is microvolts to millivolts and is ignored in processing. The sweep voltage

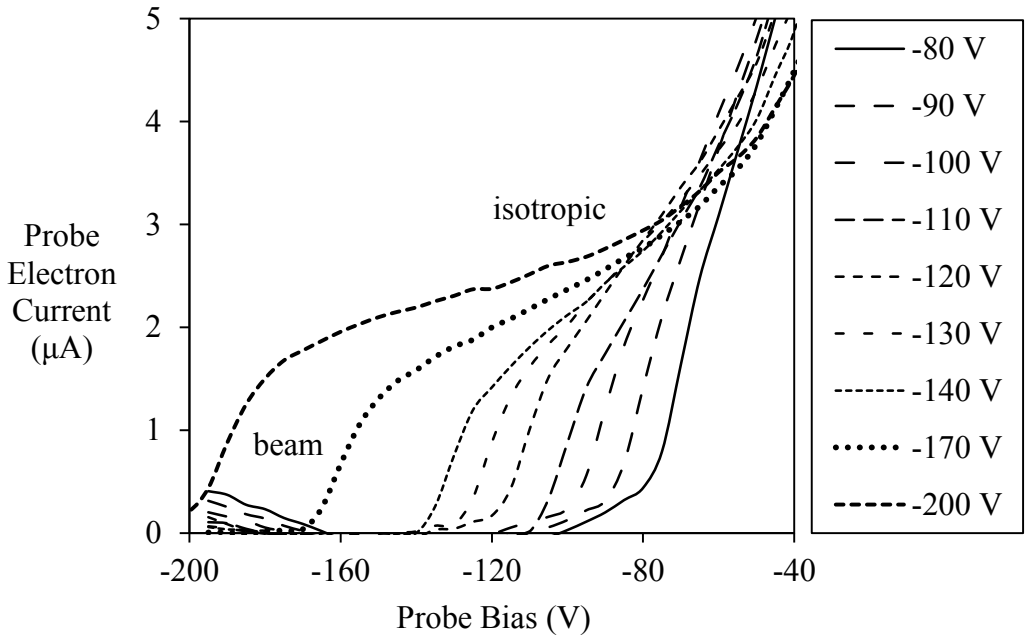

Figure 4.10: Sample electron current from planar Langmuir probe in plasma cell in electron-repelling, ion-collecting region at 10 mA discharge current, varied discharge voltage.

spacing is typically 0.2 V. Because the sweeps are much slower than plasma ion and electron response timescales, the measurements are considered time-averaged and do not give any information about oscillatory phenomena in the plasma.

Langmuir Probe Uncertainty

While Langmuir probes in theory give a large amount of information about the plasma at their location, in practice the measurements are subject to potential sources of uncertainty. A useful enumeration of many possible sources of error is given in the review by Demidov *et al.* [28]. These include influence of the probe holder, uncleaned probe tip surface, uneven work function over the probe surface, plasma potential oscillations, plasma potential perturbation induced by the probe sweep, and instrumental functions of the measurement electronics. Other factors include the effect of SEE from the probe tip due to electron and ion impacts, selection of the correct interpretation theory, and the accuracy of knowledge of the probe collection area.

One of the most significant observed errors is the effect of an uncleaned probe surface, so in this work probe cleaning techniques are used. Removal of surface contaminants and adsorbed gases can be accomplished by biasing the probe tip strongly negative to clean it by ion sputtering or positive to clean it by electron heating to incandescence. For the tungsten planar Langmuir probe used, an initial significant effect of cleaning by ion sputtering at -500 V was observed. The probe was periodically biased to -500 V to continue the cleaning, but no strong effect was observed after the initial cleaning.

The repeatability in determining the fits in the various ion and electron regions of the probe characteristics was about ± 10%, which dominated the repeatability in determining the measured number densities and electron temperatures. This relative repeatability gives confidence that the measured trends in the plasma parameters are accurate. The absolute uncertainty in the measured number densities and temperatures due to the host of other possible systematic errors is difficult to bound, but given the agreement between Debye lengths and measured sheath thicknesses the measurements are almost certainly within an order of magnitude of the true values. Given the simplicity and stability of the multidipole plasma, many of the possible effects should not be significant (plasma potential oscillations / perturbation induced by the probe sweep.) The author estimates that the measured number densities and temperatures are within a factor of 2-4 of the true values.

The measured energy of the primary electrons shows up sharply in the curves and tracks well with the plasma cell discharge voltage as stands to reason, so there is negligible uncertainty in its determination.

4.2.3 Emissive Probe

An emissive probe is similar to a Langmuir probe, but is configured such that it can be heated to the point of thermionic electron emission. The probes used in these

experiments are configured with a "hairpin" tip following the design used by Xu [101], as shown in Figure 4.11.

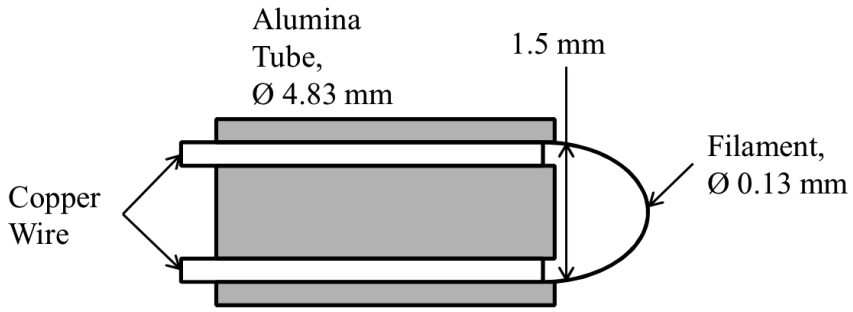

Figure 4.11: Schematic of emissive probe tips used, design of Xu [101].

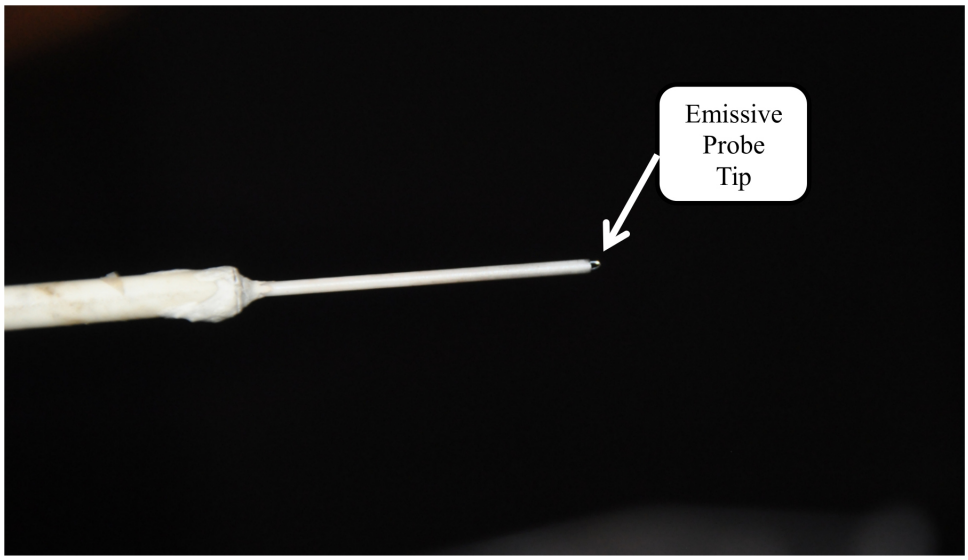

Figure 4.12: Photo of an emissive probe tip as built.

The probe is oriented so that the plane of the half-loop is parallel to the wall material sample plane to maximize spatial resolution. One could argue that the spatial resolution of the probe is thus the diameter of the tip filament, however in practice it was often necessary to angle the probe slightly in order not to impact the wall with the probe support. Consequently, the spatial resolution of the probe is estimated at 1 mm.

The connection between the emitting thoriated-tungsten filament and the copper

wires interior to the probe is done by a mechanical press-fit. This connection method proved troublesome in practice, and several probes developed loose connections in vacuum resulting in unsteady heating and emission current levels. For future work it is recommended to use a micro-spot-weld connection between the tungsten and interior wire.

The heating applied to an emissive probe allows for multiple strategies to determine the plasma potential. A review of emissive probe methods and techniques is given in a review by Sheehan [86]. One method is the so-called "floating probe" method, in which the probe is heated to strong emission to neutralize the probe sheath, such that the floating potential of the probe is roughly equivalent to the plasma potential. This method has the advantage of real-time readout of the measured potential, but clearly depends on some of the sheath phenomena under investigation.

If a real-time measurement is not required, a more reliable method is to heat the probe less, to achieve emission only comparable to a few times the ion saturation current, and then to perform multiple voltage sweeps of the probes with varying levels of heat / electron emission. The point at which electrons are able to be emitted from the probe corresponds to the plasma potential – when the probe is biased below the local plasma or sheath potential, the electrons will be forced up the potential gradient and escape from the probe, while if the probe is biased above the local potential, the electrons will be contained by the potential gradient and return to the probe tip. In the former condition, the emission will be measured, in the latter condition it will not, allowing the deduction of the plasma potential from multiple sweeps extrapolating to the condition of zero emission. This method is used for the measurements in this work.

Emissive Probe Operation

The emissive probe is heated with constant DC current from a Xantrex XPD 60-9 instrumentation power supply and biased with a Keithley 2410 Sourcemeter. The Sourcemeter also simultaneously measures the current emitted and collected by the probe. Since the probe is heated with DC current, there exists a steady-state voltage drop across the two legs of the probe circuit and the probe tip while in operation. The sourcemeter voltage sweep bias is always applied to the low-voltage leg of the heating circuit, so the voltage data of the collected I-V curves is offset by half of the DC heating voltage to more closely reflect the true bias potential of the probe tip. The cold resistance of the center conductor of the RG-58 coaxial cables that are used to connect the emissive probe are measured to be on average 1.2 Ω, and the probe has a cold resistance of about 0.6 Ω. The heating voltage was usually about 6 V, so the voltage drop across the probe was about 1.2 V, and across the probe tip about 1 V. This voltage drop is incorporated into the experimental uncertainty section.

An interactive script was made to plot the derivative of the collected I-V traces from the emissive probe and allow the user to select the inflection point. The script was initially designed to automatically select the inflection point without input from the user, but this method was not successful in the presheath for low probe emission currents. Examples of interpretation in the sheath, presheath, and bulk plasma regions are shown in Figures 4.13 - 4.18.

Figure 4.14 shows the numerical derivative of an emissive probe I-V trace obtained with the probe well within the sheath region, where the bulk of the plasma electrons are repelled from the wall by the sheath and thus are not collected by the probe. The dominant feature of the trace is the peak in the derivative corresponding to the thermionic emission of the electrons from the probe when biased below the local potential, making it easy to pick out the peak and process the data.

Figure 4.16 shows the numerical derivative of an emissive probe I-V trace obtained

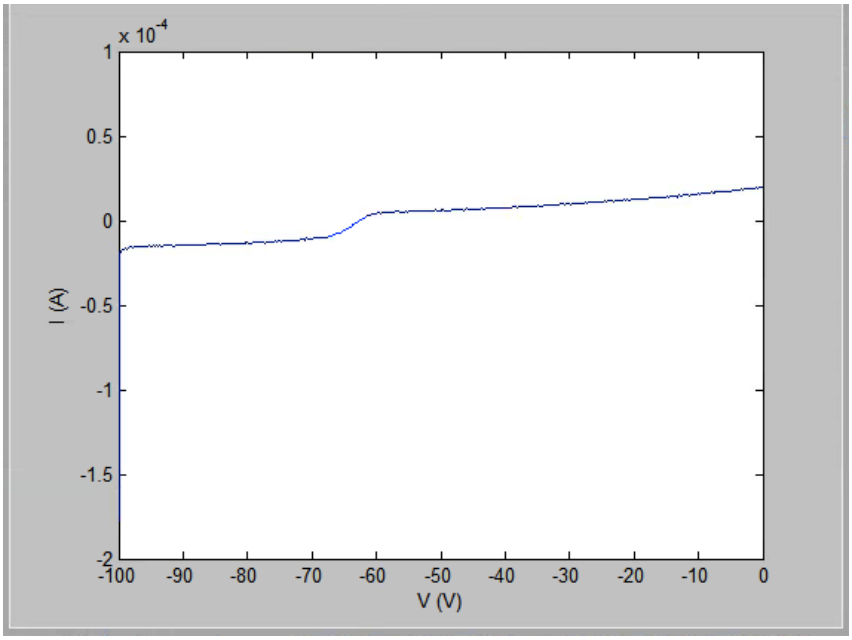

Figure 4.13: Raw emissive probe I-V trace obtained with the probe well within the sheath region.

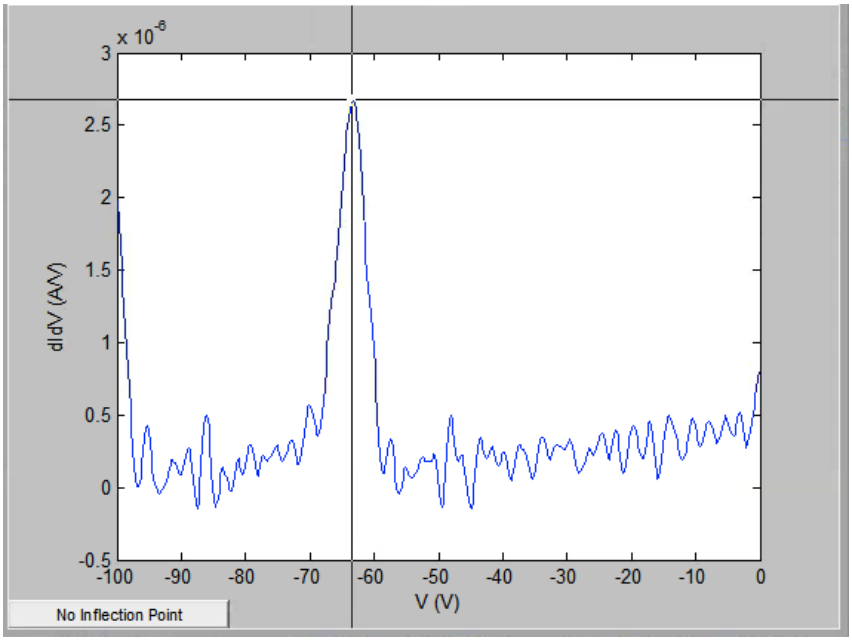

Figure 4.14: Numerical derivative of an emissive probe I-V trace obtained with the probe well within the sheath region. Plasma electrons are not collected and inflection point is clearly visible.

with the probe on the border between bulk plasma and sheath regions. Plasma electrons are plentiful and the emissive probe peak is not the tallest in the scan. For this reason, an automated processing script to simply select the tallest peak in the trace often yielded incorrect results in the transition region between plasma and sheath. This difficulty can be overcome by increasing the emission from the probe, however that increases the perturbation introduced by the probe. Ultimately it was decided that it was more effective to digitally select the appropriate inflection points manually – the crosshairs in Figures 4.14 - 4.18 show the user cursor positioned to select and record the inflection point. A promising method for automated processing may be to subtract a "background" trace obtained with the probe heat decreased to the point of no emission.

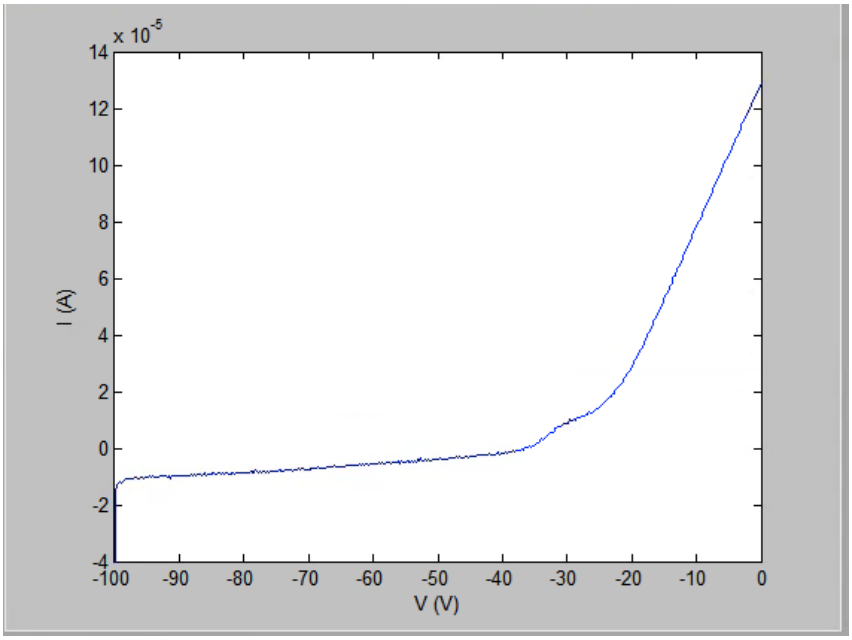

Figure 4.15: Raw emissive probe I-V trace obtained with the probe on the border between bulk plasma and sheath regions.

Figure 4.18 shows the numerical derivative of an emissive probe I-V trace obtained with the probe positioned within the bulk plasma. The emissive probe peak lines up with collection of the plasma electrons and is the tallest peak in the trace, facilitating easy data processing.

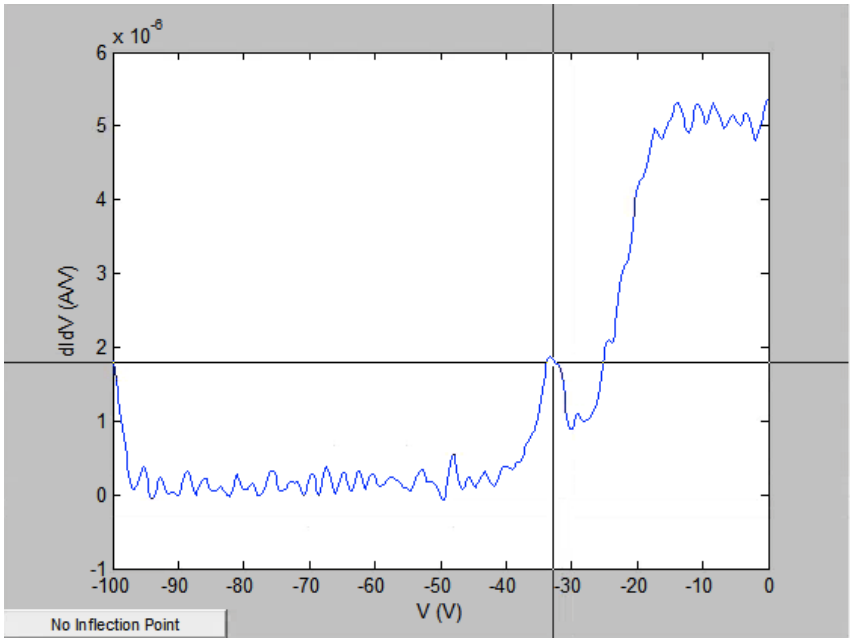

Figure 4.16: Numerical derivative of an emissive probe I-V trace obtained with the probe on the border between bulk plasma and sheath regions. Plasma electrons are plentiful and the emissive probe peak is not the tallest in the scan, complicating automated data processing.

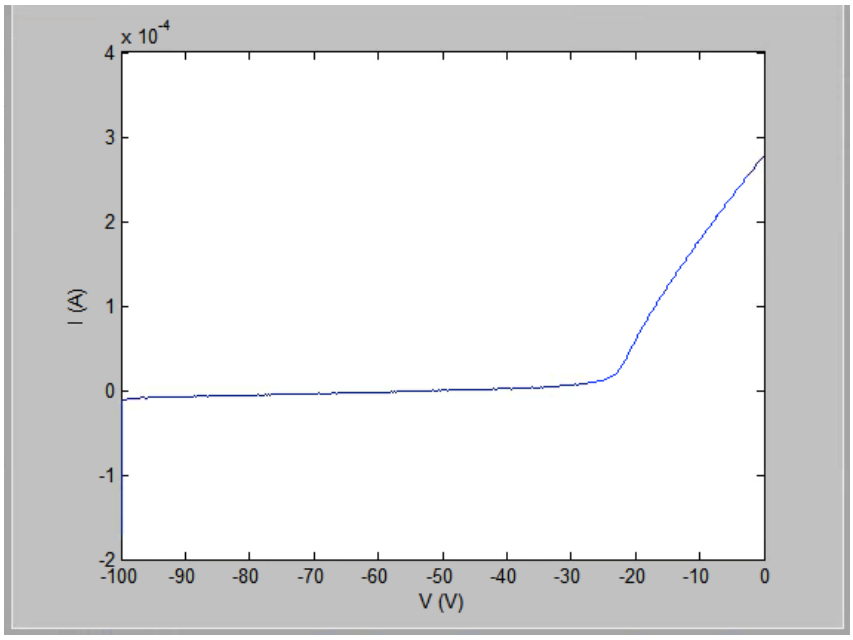

Figure 4.17: Raw emissive probe I-V trace obtained with probe in bulk plasma.

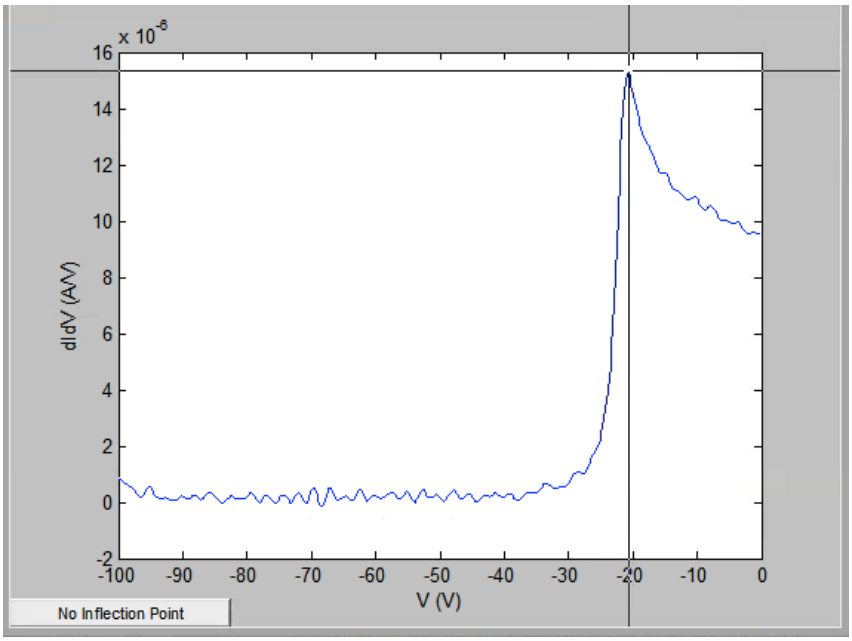

Figure 4.18: Numerical derivative of an emissive probe I-V trace obtained with probe in bulk plasma. The emissive probe peak lines up with collection of the plasma electrons and is the tallest peak in the trace.

The emission current for a given trace can be determined by averaging the emitted electron current (subtracting the ion current from a non-emitting trace) in the region biased more negatively than the inflection point / plasma potential. With multiple levels of probe heating / emission, it is possible to extrapolate back to a condition of no emission, as shown in Figure 4.19.

Emissive Probe Measurement Uncertainty

The intrinsic uncertainty of the extrapolated inflection point method should theoretically be quite low, on the order of (T_e / 10) [86]. For the plasma measured in practice, the bulk T_e was often 5 eV or less, which would give an uncertainty of 0.5 V ($\pm$ 0.25 V) in the plasma potential determination. The voltage of the probe was swept in a stair-step sweep pattern at lower voltage increments, typically 0.1 or 0.2 V, in order to try to preserve this uncertainty level. However, the DC voltage drop across the probe tip of 1 V (the uncertainty in the tip voltage $\pm$ 0.5 V) was often greater

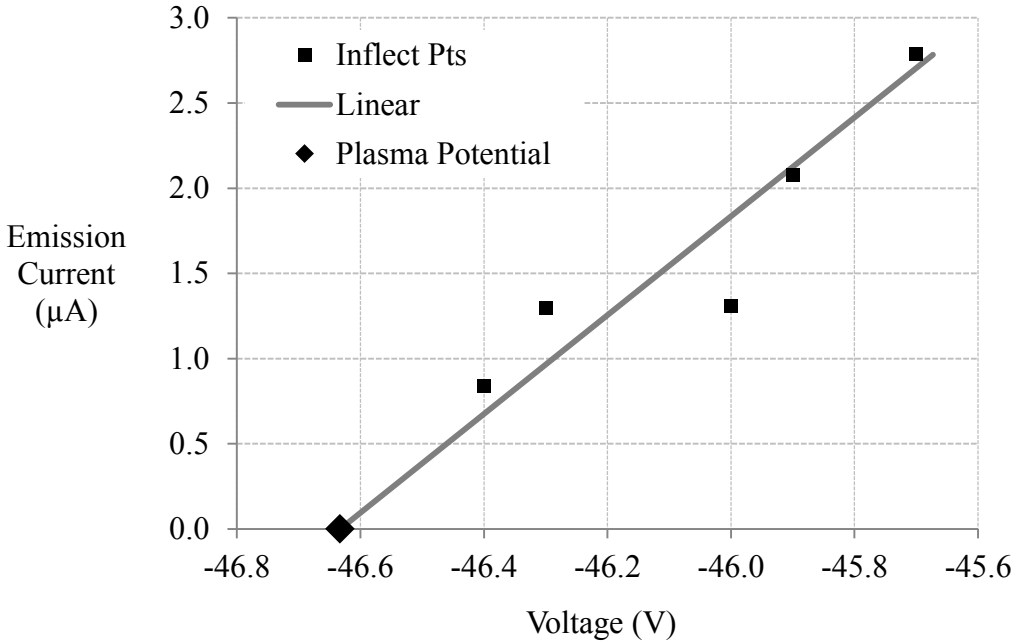

Figure 4.19: Extrapolation of inflection points at different levels of heating / emission to condition of zero emission.

than the method uncertainty, giving a propagated error of ± 0.56 V. In many data graphs, the sheath potential varies across order of 50 V, so error bars are not visible and are omitted in those graphs.

In some experiments to follow, only 1-3 emissive probe scans were collected at each point, too few to perform a rigorous extrapolation using the inflection points. In these cases, the probe emission current was minimized to make the individually-measured inflection points as close to the plasma potential as possible, and the plasma potential was taken as the mean of the measured inflection points. Since the order of variation in inflection points at various locations often did not exceed 1 V, the uncertainty ascribed to these measurements was doubled to 1 V (± 0.5 V), and thus the propagated error to ± 0.7 V. In the text, it is noted for each dataset which method is used to calculate the final potential measurement.

CHAPTER V

VALIDATION EXPERIMENTS

Experiments were conducted with both conductive and insulating wall material samples in order to validate the emissive probe sheath measurement technique. With a conductive wall material sample, it is possible to directly measure and/or set the wall potential using a voltmeter or power supply. The sheath measurements should show the potential changing across the sheath and terminating at the wall potential; thus, having a conductive wall provides a useful check on the validity of the sheath measurements. The measurements over the insulating sample confirm that the measurement technique can also be applied in that situation.

5.1 Experimental Setup

This experiment was run with two different setups, one including only the insulating wall sample and one including only the conductive sample. The insulating wall material sample used was a 4-inch diameter, 1/4 inch thick disc of hexagonal AX05-grade BN. This sample was positioned on centerline in the plasma cell using alumina tubing inserted into a small radial hole drilled in the thickness of the sample and affixed with Aremco 571 Ceramabond. The conductive wall sample used in this experiment was a 2.75-inch stainless steel disc of 0.5 inch thickness. The disc was drilled and tapped radially, and suspended on centerline in the plasma cell using a length of 10-32 stainless steel threaded rod. The conductive support threaded rod also served as path for the disc electrical connection. The support threaded rod was insulated from the plasma and the plasma cell frame using alumina tubing.

The plasma cell was configured as shown in Figure 4.4, using a Kepco BHK 2000-0.1MG as the discharge power supply and a TDK-Lambda Genesys 60V-25A as the

filament heating supply. Different from most experiments to follow, the experiments with the BN sample were run at varying neutral pressures in the vacuum chamber, ranging from 5 x 10^{-5} to 1 x 10^{-4} Torr. The metal wall sample experiments were run at 1 x 10^{-4} Torr.

5.2 Results

Operation of the discharge voltage at 60 V and discharge current 10 mA yielded a low-density plasma: discharge current was observed, but there was no glow of argon visible within the plasma device. The chief visual feature of the device in operation was the glow of the hot filaments.

Diagnostic measurements were obtained using a cylindrical Langmuir probe and an emissive probe. The cylindrical probe data did not exhibit a well-defined "knee" as is normally expected for the geometry. In retrospect, this was due to the large sheath size in the low-density plasma: the collecting sheath of the probe became spherical in shape as it exceeded the dimensions of the cylindrical probe. The current collection increased linearly with voltage, as expected from spherical probe theory [70].

Initial attempts to interpret the Langmuir probe using cylindrical probe theory yielded plasma number densities on the order of 5 x 10^{13} - 2 x 10^{14} m^{-3}. In light of later measurements, these values are believed to be incorrectly high by about an order of magnitude.

Emissive probe measurements were more successful. Thick sheath structures were measured at pressures of 5 x 10^{-5}, 7.5 x 10^{-5}, and 1.0 x 10^{-4} Torr-Ar. The measured sheath profiles are shown in Figures 5.2 and 5.1.

5.3 Discussion

Inspecting the measured sheath potential profiles over the stainless steel wall sample in Figure 5.1, it can be seen that a linear extrapolation to the wall potential yields good agreement with the measured wall potentials (open symbols in Figure 5.1.) While a

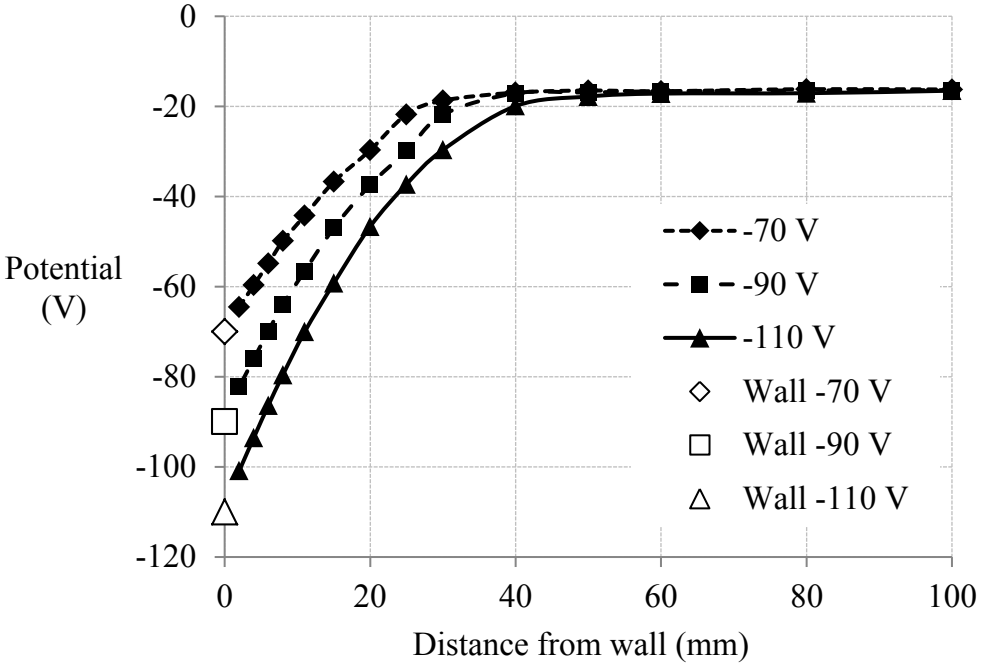

Figure 5.1: Sheath potential profiles measured using emissive probe over stainless steel wall at varied wall bias. Profiles extrapolate to agree with voltmeter-measured wall floating potential. Argon plasma, mean method, pressure 1 x 10^{-4} Torr-Ar, discharge current 10 mA.

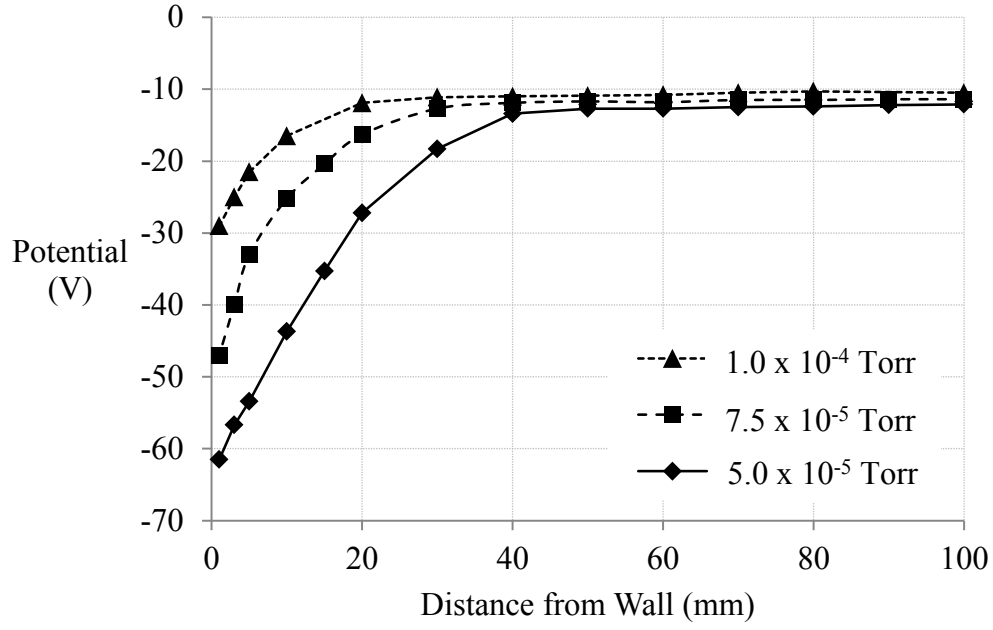

Figure 5.2: Sheath potential profiles measured using emissive probe over BN wall in low density plasma at varied neutral pressure (uncorrected). Argon plasma, extrapolated method, discharge voltage 87 V, discharge current 9.5 mA.

linear extrapolation may not be appropriate in situations with increased secondary electron emission, *e.g.* if there is a virtual cathode, this experiment does confirm that the swept emissive probe technique is reliably measuring the potential. The sheath profiles also exhibit a large sheath thickness ranging from 20-40 mm, so the experiment confirms that the plasma cell is able to achieve low enough plasma densities to form large-scale sheaths.

The trend in sheath thickness with pressure of Figure 5.2 agrees with expectation: as the neutral pressure becomes higher in the device, there is more energy exchange between the plasma electrons and neutrals and more ionization, so the sheath potential and thickness decreases. The large magnitude of the sheath potential drop ($\approx$ 50 V) at 5 x 10^{-5} Torr pressure was initially surprising, as the measured electron temperature was order of 2 eV so the predicted sheath potential for argon would be about 10 V, *c.f.* equation (2.42) / Figure 2.6. In light of measurements from future investigations, it is now clear that the reason for the high sheath potentials was the relative abundance of isotropic energetic electrons emitted from the filament.

5.4 Comparison with GWU Simulation

Having obtained some first measurements of sheath potential profiles, we provided the data to our collaborators at GWU. They were able to run a computation to solve the Poisson equation throughout the sheath profile and generate theoretical potential profiles to compare to experiments. In the next sections we give a quick overview of their method, for more details the interested reader may refer to [13].

5.4.1 Setup

The elctrostatic Poisson equation proceeds from Gauss's Law and Faraday's Law in the case of a linear, isotropic, homogeneous medium in the absence of a time-varying magnetic field.

$$\nabla^2\phi = -\frac{e}{\epsilon_0}\left(Z_{\mathrm{i}} n_{\mathrm{i}} - n_{\mathrm{e}}\right) \tag{5.1}$$

In order to solve this equation for the potential profile $\phi(x)$, it is necessary to express n_i and n_e as functions of known quantities such as the plasma conditions at the sheath edge. Neglecting electron loss to the wall, we can write the electron density n_e in terms of the potential, which is the Boltzmann relation (*c.f.* Appendix A.2):

$$n_\mathrm{e} = n_0 \exp\left(\frac{e\phi}{k_\mathrm{B}T_\mathrm{e}}\right) \tag{5.2}$$

Plugging this into the Poisson equation, we have:

$$\nabla^2\phi = -\frac{e}{\epsilon_0}\left(Z_\mathrm{i}n_\mathrm{i} - n_0 \exp\left(\frac{e\phi}{k_\mathrm{B}T_\mathrm{e}}\right)\right) \tag{5.3}$$

If we assume constant values for the plasma and ion density, it becomes possible to solve for the plasma potential using a finite-difference division of the sheath domain and a non-linear Newton iteration. The scheme as run is not fully predictive, as it is necessary to specify the start and end points of the sheath potential as well as the plasma properties. Nevertheless the computation is able to investigate how well the data conforms to theoretical expectation for an electrostatic potential structure, and what plasma parameters are expected given the potential measurements.

5.4.2 Results

The results of the Poisson computation are shown below in Figure 5.3.

5.4.3 Discussion

As shown in Figure 5.3, the computation is able to find good agreement with the measured experimental data with an input plasma density in the 3.3 x 10^{12} m^{-3} range. This computation, together with the linear slope of the Langmuir probe characteristic, convinced us that the Langmuir probe data from the cylindrical probe was not being interpreted correctly in this plasma, and that the reported densities in the 10^{14} m^{-3} range must be erroneously high. Nevertheless, the promising agreement to the shape of the potential profile gave confidence that the emissive probe data was reliable.

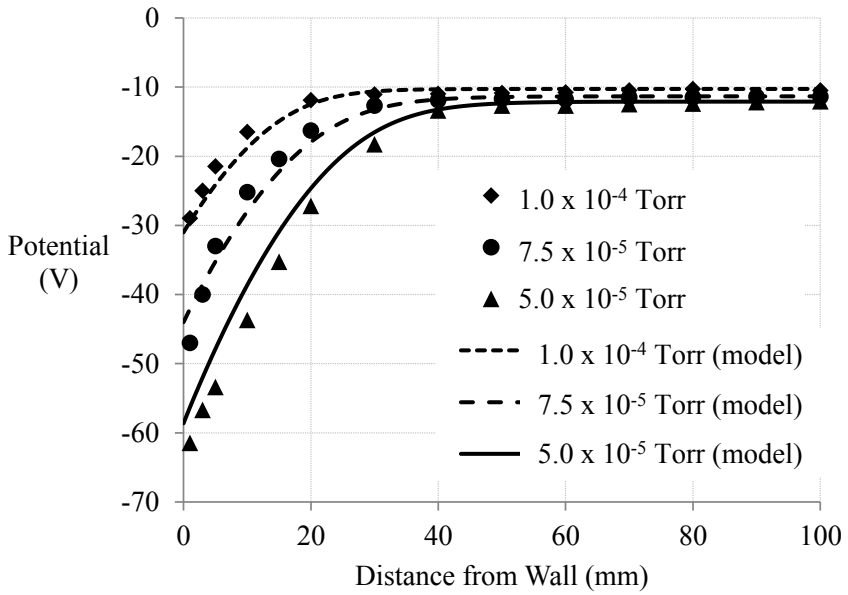

Figure 5.3: Measured sheath profiles of Figure 5.2 compared to GWU Poisson solver with $n_0 = 3.3$ x 10^{12} m^{-3}.

CHAPTER VI

INFLUENCE OF ELECTRON EMISSION FROM THE WALL

6.1 Experiment Ia: BN Wall

6.1.1 Experimental Setup

Experiments were performed in the plasma cell to characterize sheaths over smooth and rough boron nitride (BN) ceramic wall material samples. BN was chosen because it is the current state-of-the-art material for Hall effect thruster discharge channels.

Wall material samples were procured and prepared by our collaborators at University of Alabama (UA). The differences between rough and smooth samples will be discussed in depth in Chapter 9, the current discussion will focus on the smooth BN. The samples are grade-AX05 (pure) hexagonal BN, 3-inch diameter, 0.25-inch thick discs. The smooth samples are polished using a Buehler Metaserv 250 grinder-polisher at 300 rpm, and the rough samples are abraded with 120 grit SiC polishing paper.

The resulting surface finish is characterized by our collaborators at GTRI using a LEXT OLS4000 profilometer. The smooth surface had no roughness that could be observed within the profilometer resolution of 0.2 µm.

The plasma cell is operated with argon gas at pressure 10^{-4} Torr-Ar. The ion-neutral mean free path is 0.8 m, so the sheath is largely collisionless. The plasma cell is operated with 10 mA discharge current and varied discharge voltage from 50 - 200 V.

6.1.2 Results

Figures 6.1 and 6.2 show the measurement results from the planar Lanmguir probe (*c.f.* section 4.2.2) function of the bias voltage applied to the plasma cell discharge filament. The Langmuir probe is positioned 100 mm from the wall, where the primary electrons have already traversed most of the plasma device. Electron number densities are on the order of 3 x 10^{12} m^{-3}, detecting similar amounts of hot (3.6 - 6.4 eV) and cold (0.3 - 1.3 eV) Maxwellian electrons. As shown in Figure 6.2, the energetic electron populations gain energy directly through the increase of the filament bias. The changes in temperature of the hot and cold Maxwellian populations are on a lower order of magnitude, but show an increase when the filament is biased below 100 V. Figure 6.1 shows that changing the filament bias does not result in a drastic change in the overall number densities or temperatures of the Maxwellian hot and cold electron populations. However, the number densities of the energetic electron populations decrease steadily. A portion of this decrease in number density is due to continuity, as the discharge current is held fixed. Additionally, this could be a result of increased energy exchange of the primary electrons with the plasma and contribute to the resurgence of the hot electron population, or it could be due to primary electrons increasingly escaping the magnetic cusps. The loss rate agrees with literature that states that the loss half-width for energetic electrons through magnetic cusps scales directly with the primary electron gyroradius [60], leading to the loss area scaling with electron energy.

Figure 6.3 shows the experimentally measured potential profiles over the smooth BN wall material sample for a range of filament biases. The profiles are given with respect to the bulk plasma potential (defined as the plasma potential measured 100 mm from the wall in each case.) The sheath thickness is roughly 40 mm. The sheath thickness does not scale directly with the wall potential as it would for a Child-Langmuir sheath, rather showing the gradual type of collapse predicted by the

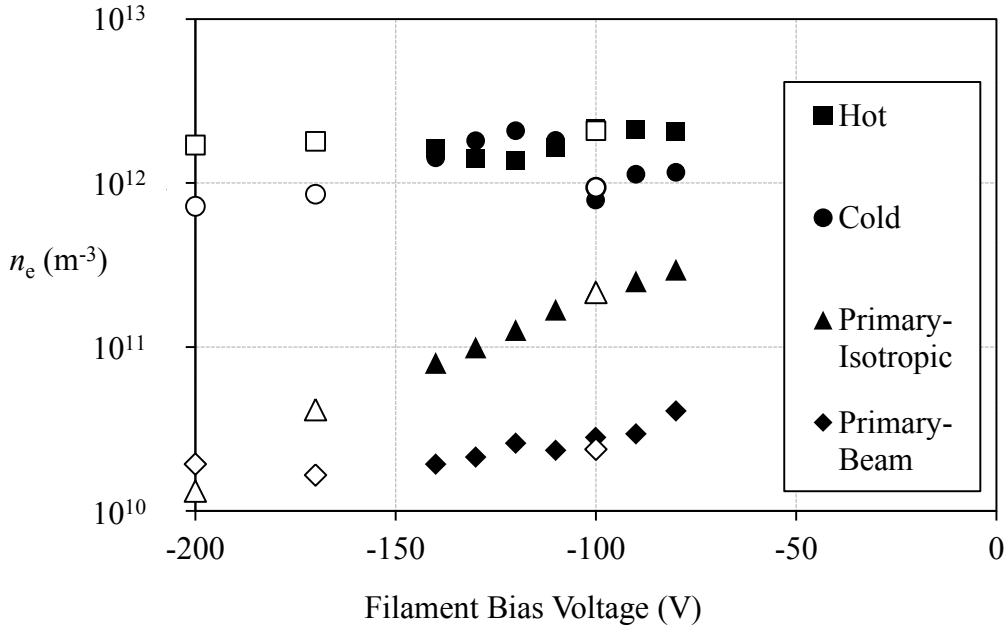

Figure 6.1: Number densities of cold plasma electrons, hot plasma electrons, and energetic plasma electrons measured by planar Langmuir probe. Argon plasma, pressure 1 x 10^{-4} Torr-Ar, discharge current 10 mA. Filled symbols are taken with smooth BN sample facing the discharge filament, open symbols with rough BN sample.

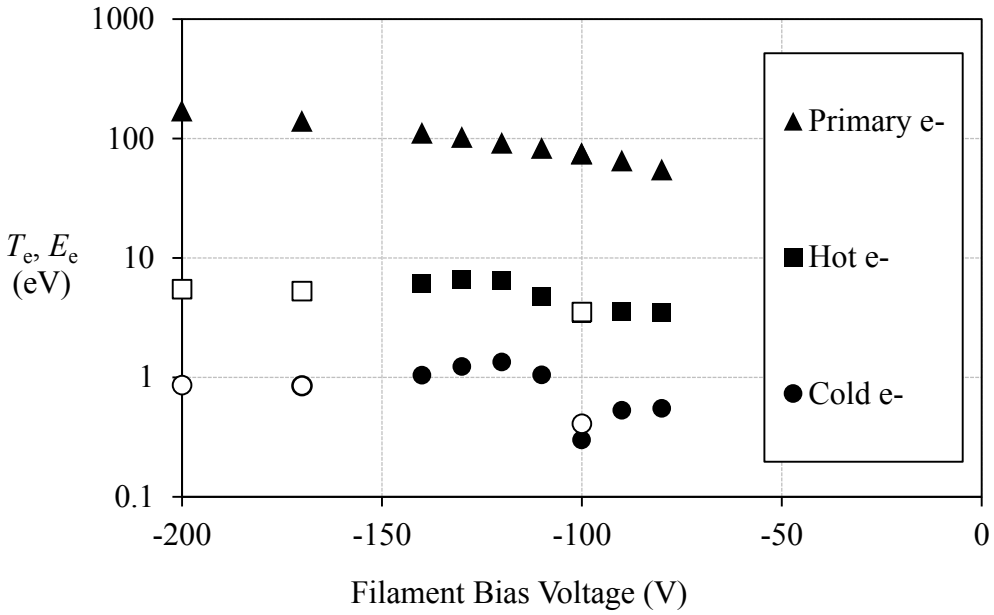

Figure 6.2: Temperatures / energies of cold plasma electrons, hot plasma electrons, and energetic plasma electrons as measured by planar Langmuir probe. Argon plasma, pressure 1 x 10^{-4} Torr-Ar, discharge current 10 mA. Filled symbols are taken with smooth BN sample facing the discharge filament, open symbols with rough BN sample.

emitting wall theories.

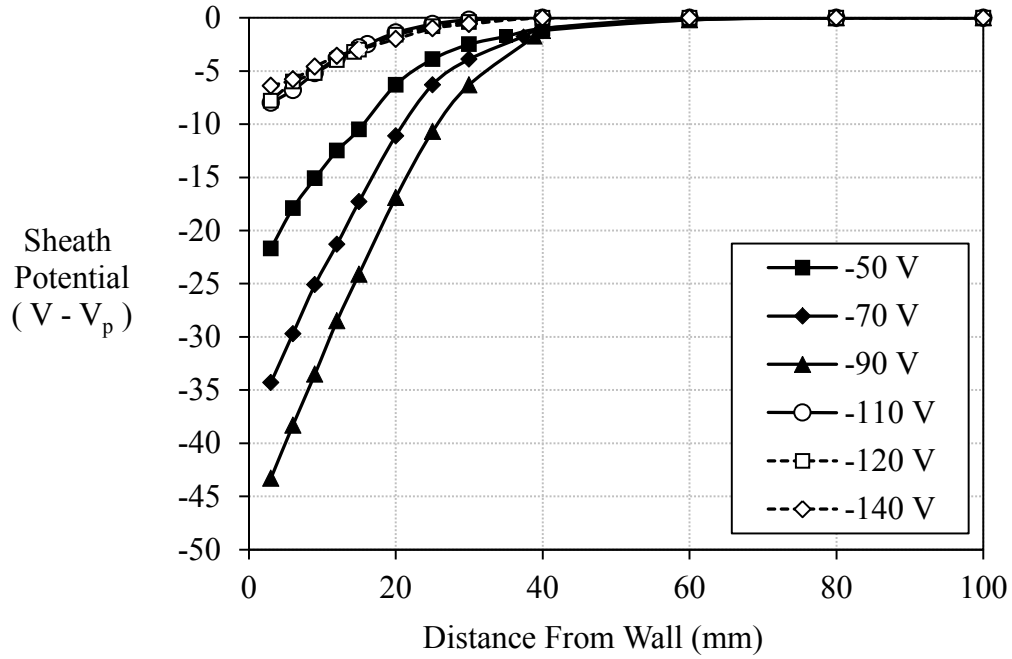

Figure 6.3: Measured sheath potential profiles over smooth BN wall for varied values of the primary electron accelerating voltage. Argon plasma, extrapolated method, pressure 1 x 10^{-4} Torr-Ar, discharge current 10 mA.

Initially, as filament bias is driven more negative, the sheath potential fall increases in order to repel enough off-normal isotropic primary electrons to enforce zero net current to the electrically isolated wall. However, once the filament bias passes a certain threshold, the SEE from the wall becomes too great to sustain the same level of potential fall. The SEE yield of BN increases approximately linearly with energy in this range. The transition between increasing and decreasing potential fall is sharp, occurring fully within 20 V. The sheath potential fall becomes the order of the electron temperature of the hot secondary electron population.

6.2 Experiment Ib: Alumina Wall

6.2.1 Experimental Setup

Additional measurements were taken with a 4.5x4.5-inch-square 0.040-inch-thick alumina wall material sample, which in theory should have a higher SEE yield than

boron nitride [1].

6.2.2 Results

The measured sheaths are shown in Figure 6.4 - Figure 6.7.

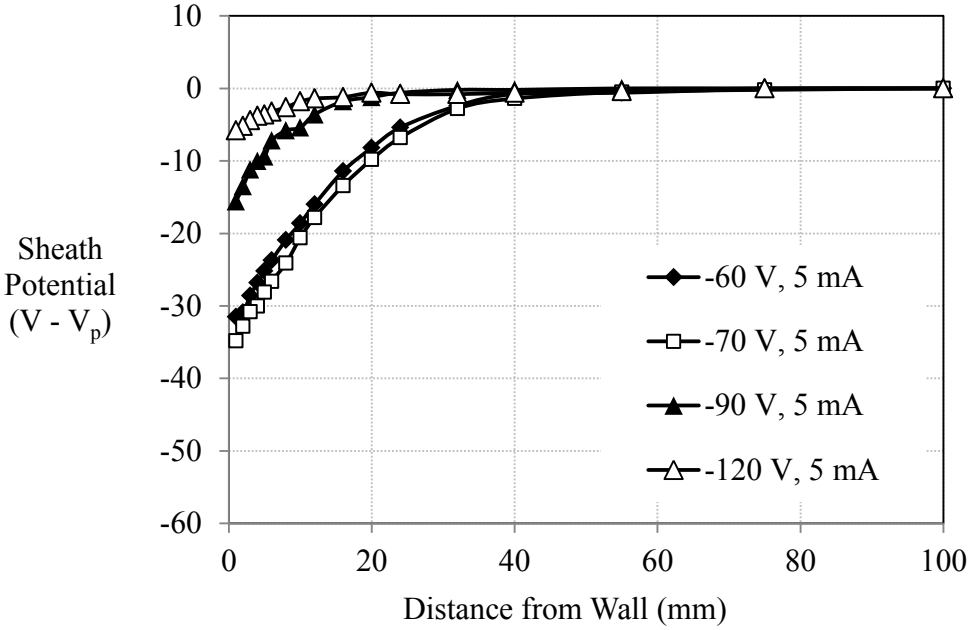

Figure 6.4: Measured sheath profiles over alumina wall at 5 mA discharge current. Argon plasma, extrapolation method, pressure 1 x 10^{-4} Torr-Ar.

Figures 6.8 - 6.10 show the bulk plasma potential, electron density, and electron temperature of the varied plasma populations as measured with the planar Langmuir probe.

Additional measurements are taken at high discharge filament bias / bombarding electron energy in effort to drive the secondary electron emission from the wall as high as possible. These results are shown in Figure 6.11.

6.3 Experiment Ic: Thermionically Emitting Wall

This experiment seeks to investigate the sheath behavior in conditions of strong emission by interrogating an alumina surface lined with powered thoriated-tungsten filaments.

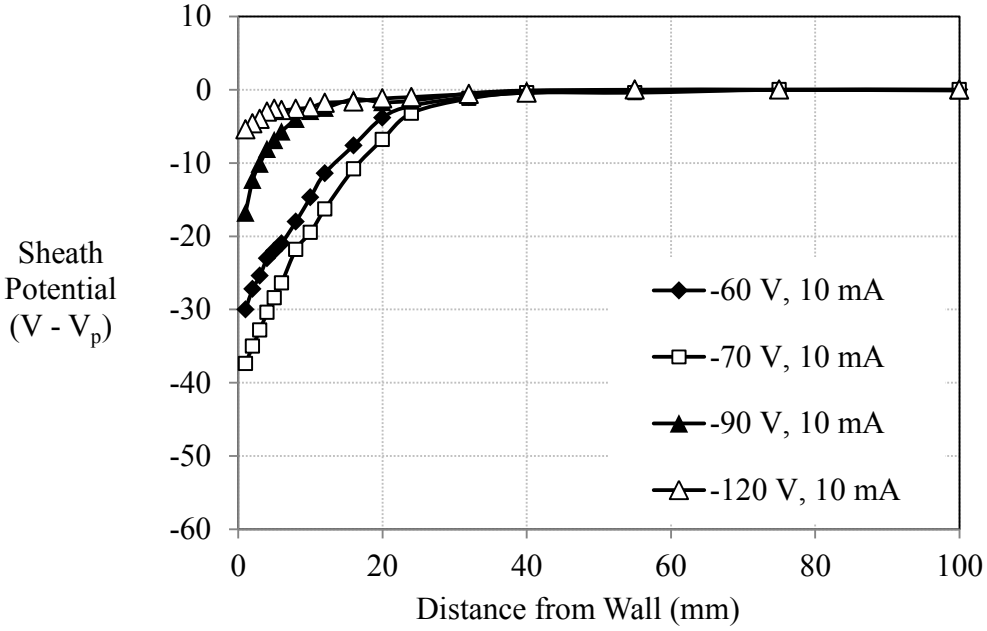

Figure 6.5: Measured sheath profiles over alumina wall at 10 mA discharge current. Argon plasma, extrapolation method, pressure 1 x 10^{-4} Torr-Ar.

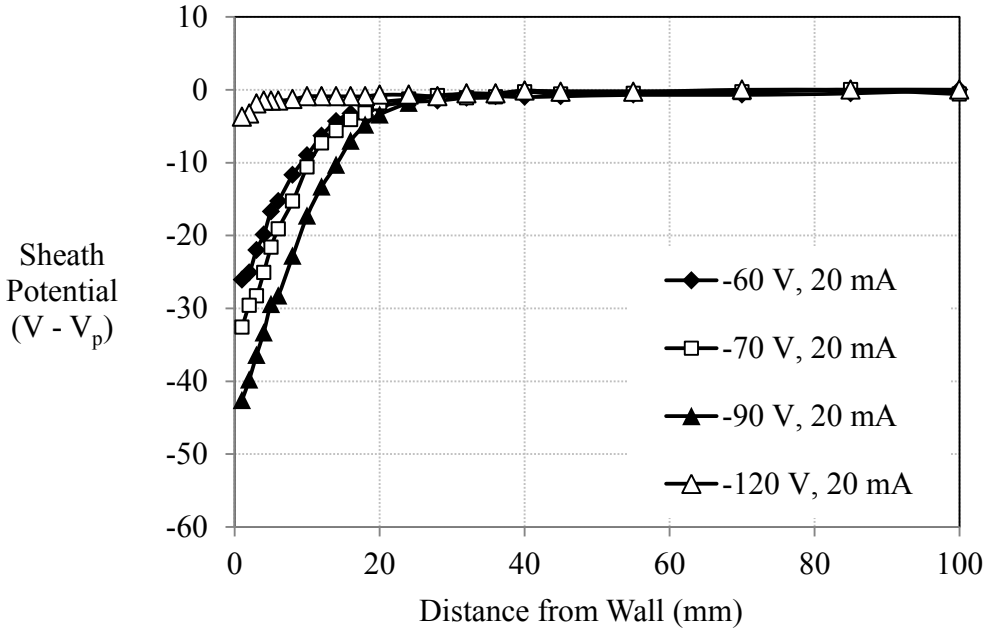

Figure 6.6: Measured sheath profiles over alumina wall at 20 mA discharge current. Argon plasma, extrapolation method, pressure 1 x 10^{-4} Torr-Ar.

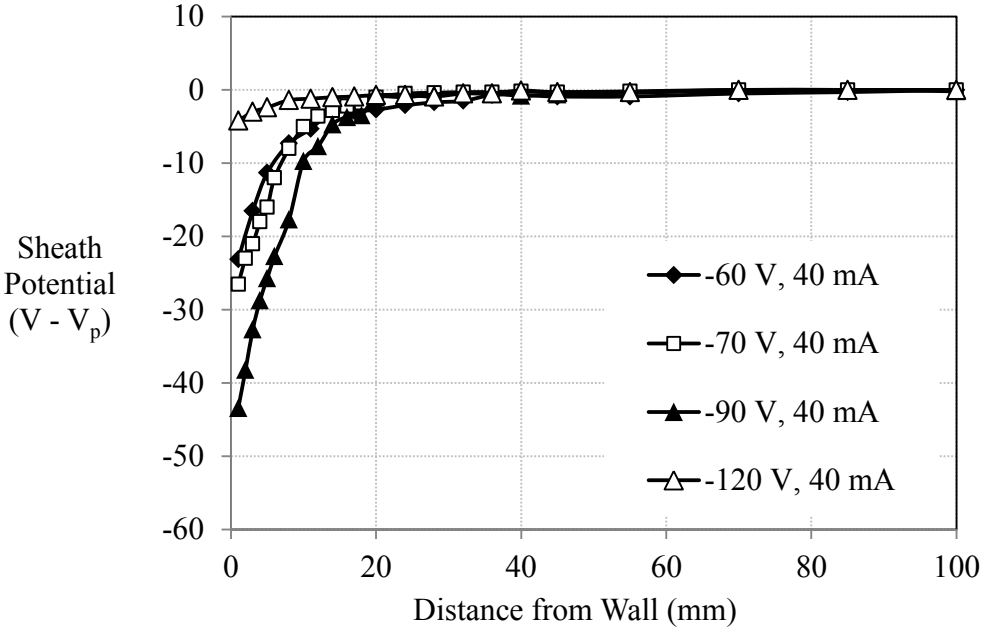

Figure 6.7: Measured sheath profiles over alumina wall at 40 mA discharge current. Argon plasma, extrapolation method, pressure 1 x 10^{-4} Torr-Ar.

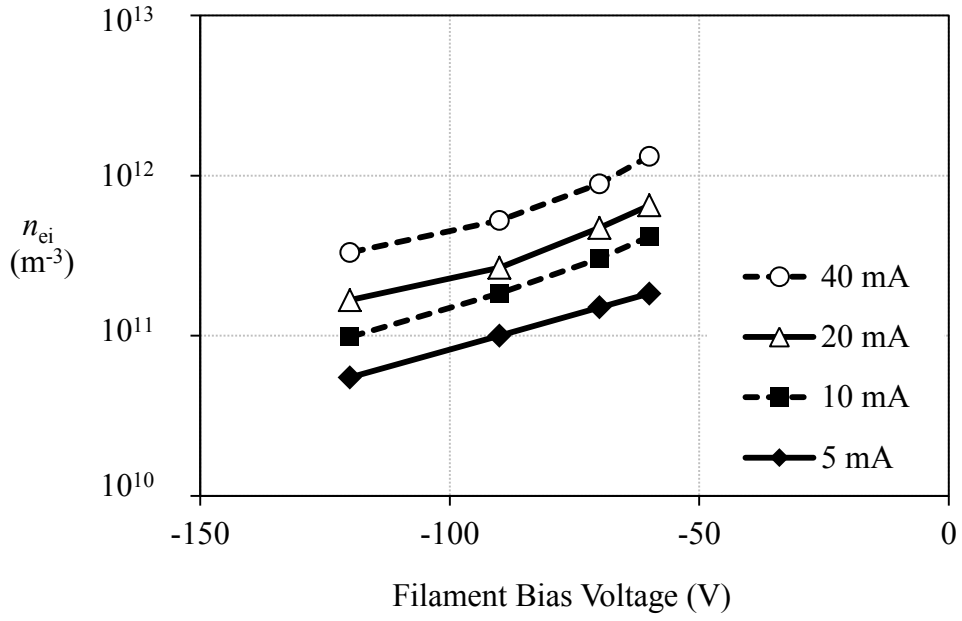

Figure 6.8: Planar Langmuir probe measurement of primary electron number density at varied filament bias voltage (discharge voltage) and discharge current. Argon plasma, pressure 1 x 10^{-4} Torr-Ar.

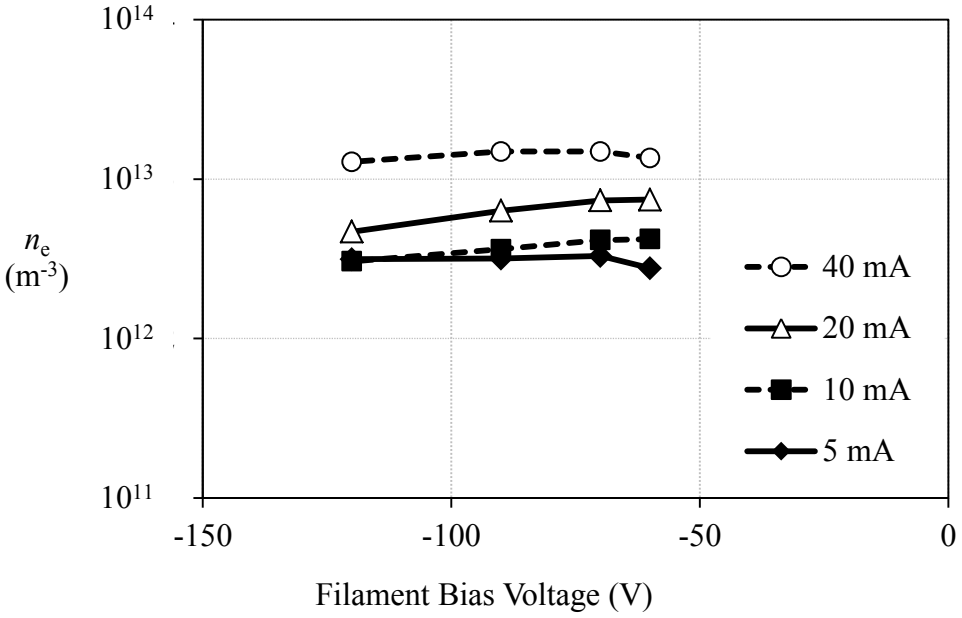

Figure 6.9: Planar Langmuir probe measurements of total electron number density at varied filament bias voltage (discharge voltage) and discharge current. Argon plasma, pressure 1 x 10^{-4} Torr-Ar.

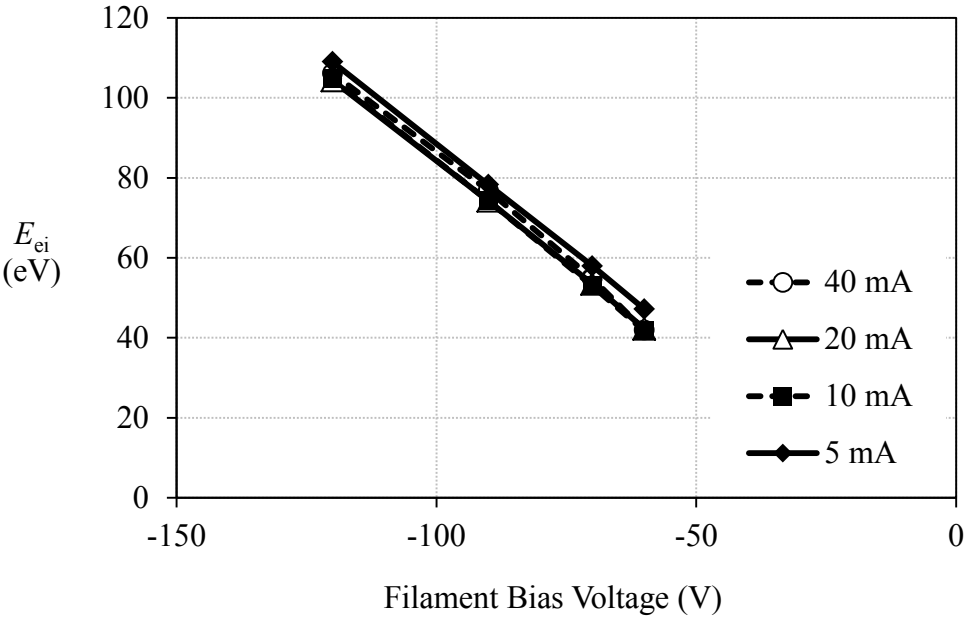

Figure 6.10: Planar Langmuir probe measurements of primary electron energy at varied filament bias voltage (discharge voltage) and discharge current. Argon plasma, pressure 1 x 10^{-4} Torr-Ar.

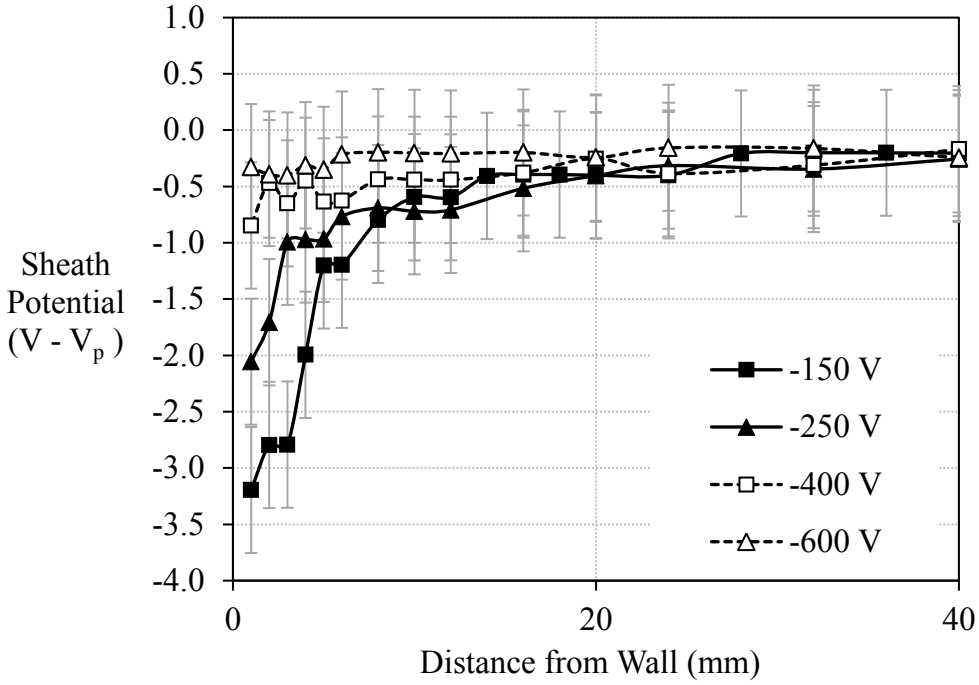

Figure 6.11: Measured sheath profiles over alumina wall at high primary electron accelerating voltages. Argon plasma, extrapolation method, pressure 1 x 10^{-4} Torr-Ar, discharge current 20 mA.

6.3.1 Experimental Setup

In this experiment, the wall material sample is a 4.5 x 4.5 inch square of alumina. The center 1.5x 4.5 inch horizontal swath of the surface is lined with emissive filaments (*c.f.* Figure 6.12). The electrical connection is made on the back side (the side not facing the plasma cell center / filaments) so that the front side can be free of non-emitting conductive material. The filaments are 0.006-inch diameter 2% thoriated tungsten. There are seven filaments in the swath. The filaments are held in tension to keep them within 1 mm of the wall surface along their length while cold. The filaments are powered in parallel with DC current.

6.3.2 Results

The bias of the plasma cell discharge filament is varied to control the energy of plasma energetic electron population. The floating potential of the wall filaments is monitored

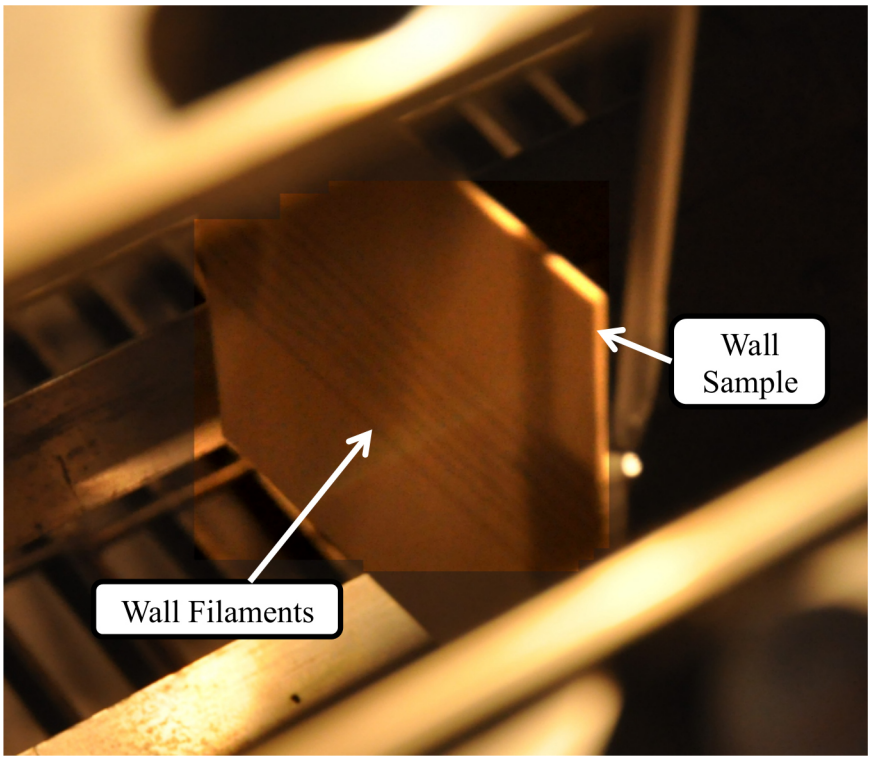

Figure 6.12: Photo of filament-driven emitting wall sample installed in plasma cell. Brightness and contrast increased on sample to show wall filaments.

as the filament bias is varied. The wall filament heating current is also adjusted and gradually increased over the course of the experiment, to change the amount of thermionic emission from the wall filaments. Figure 6.13 shows the plasma cell on at 10 mA discharge current with the wall filaments on.

The experiment is carried out over 3 days, with the vacuum chamber retained at vacuum throughout. The plasma discharge is turned off overnight.

For a given level of heating current of the wall filaments, significant variation is observed in the wall filament floating voltage response over the course of the experiment. Figure 6.14 shows the response of the wall filament floating potential to filament bias / plasma electron energy between days 1-3 with the wall filaments at low heating current (1 A per filament).

As the heating current of the wall filaments is increased, the floating potential collapses to near the plasma potential as observed in the other experiments at high

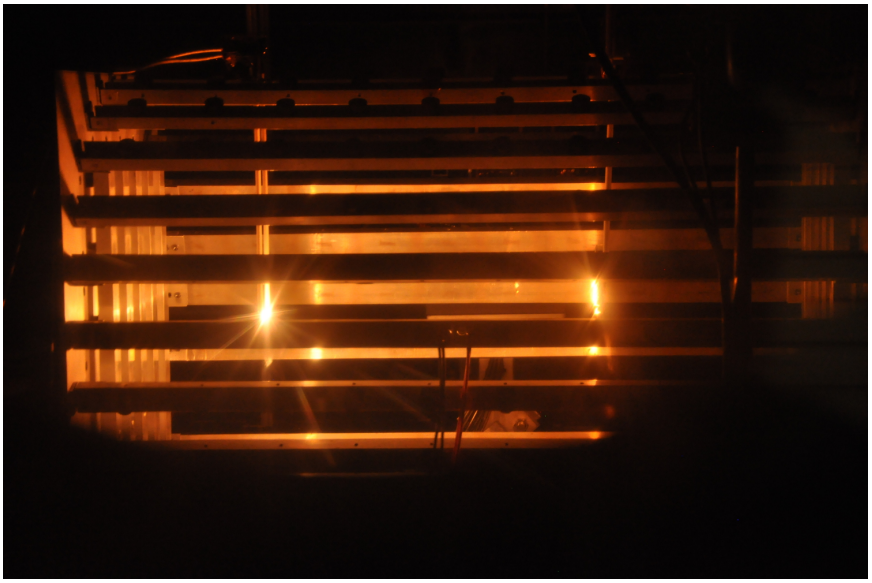

Figure 6.13: Photo of filament-driven emitting wall sample operating in plasma cell. Argon plasma, pressure 1 x 10^{-4} Torr-Ar, discharge current = 10 mA, wall filament heating current = 1 A per filament.

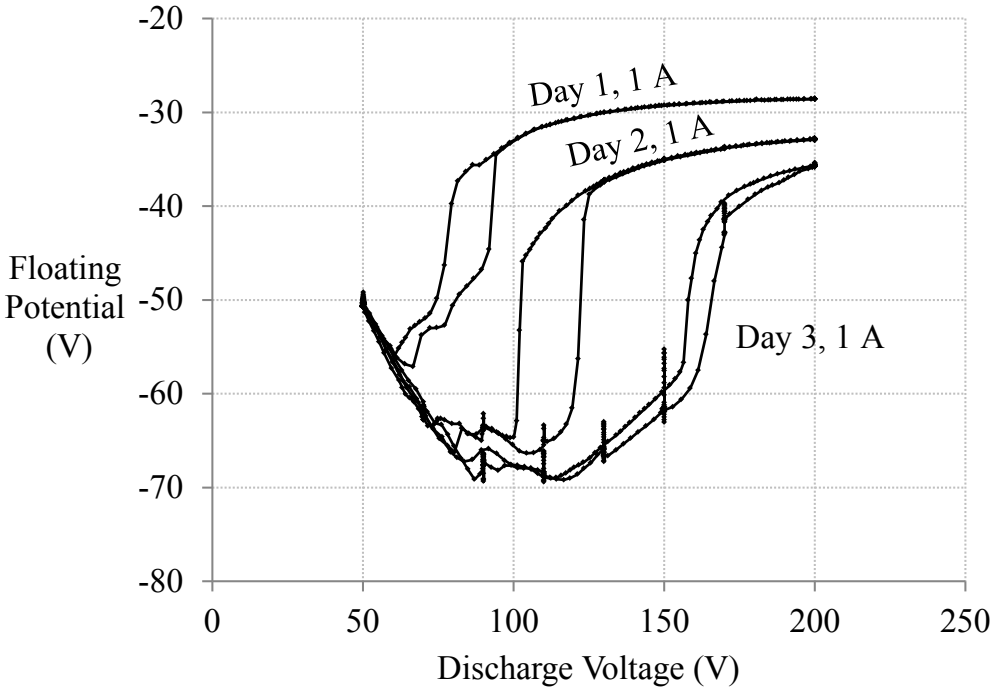

Figure 6.14: Floating sheath potential of wall filaments (average of high and low legs) vs. discharge filament bias / plasma electron energy, days 1-3. As experiment duration progresses, sheath collapse occurs at higher discharge voltage. Vertical lines are perturbations due to Langmuir probe sweeps 100 mm from wall. Argon plasma, pressure 1 x 10^{-4} Torr-Ar, discharge current = 10 mA, wall filament heating current = 1 A per filament.

emission. Figures 6.15 and 6.16 show the response of the wall filament floating potential and plasma potential to filament bias / plasma electron energy, for different levels of the wall filament heating current.

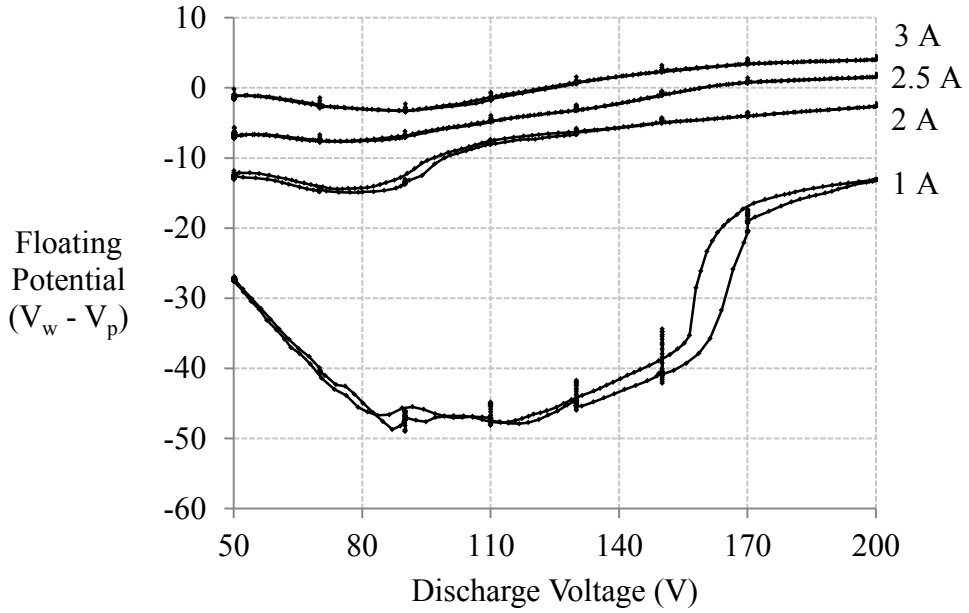

Figure 6.15: Floating potential of wall filaments (average of high and low legs) and plasma potential with varied levels of heating current and discharge filament bias / plasma electron energy. Vertical lines are perturbations due to Langmuir probe sweeps 100 mm from wall. Argon plasma, pressure 1 x 10^{-4} Torr-Ar, discharge current = 10 mA.

Post-test inspection of the wall material sample confirmed that significant re-deposition of the wall filament material had occurred on the alumina wall material sample over the course of the experiment. The curved shape of the deposited layer also indicated that thermal expansion of the filaments had caused them to sag and deform along the surface of wall. The deposited layer did not give the surface low enough resistance to be measurable on a Fluke 83 V multimeter, which is to say that either some additional layer prevented the multimeter lead from making a connection or the resistance remained greater than 50 MΩ.

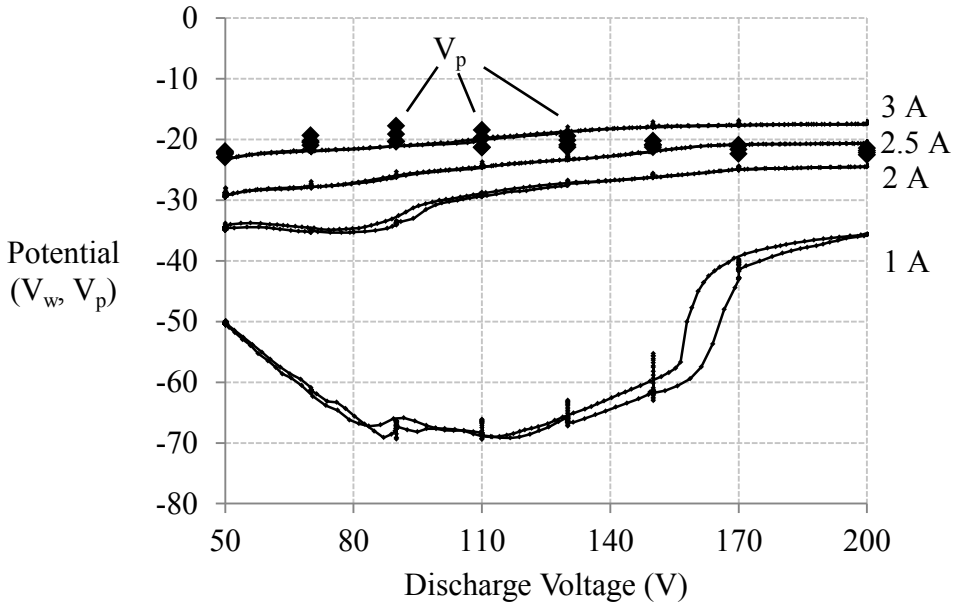

Figure 6.16: Floating sheath potential (with respect to interpolated plasma potential) of wall filaments (average of high and low legs) with varied levels of heating current and discharge filament bias / plasma electron energy. Vertical lines are perturbations due to Langmuir probe sweeps 100 mm from wall. Argon plasma, pressure 1 x 10^{-4} Torr-Ar, discharge current = 10 mA.

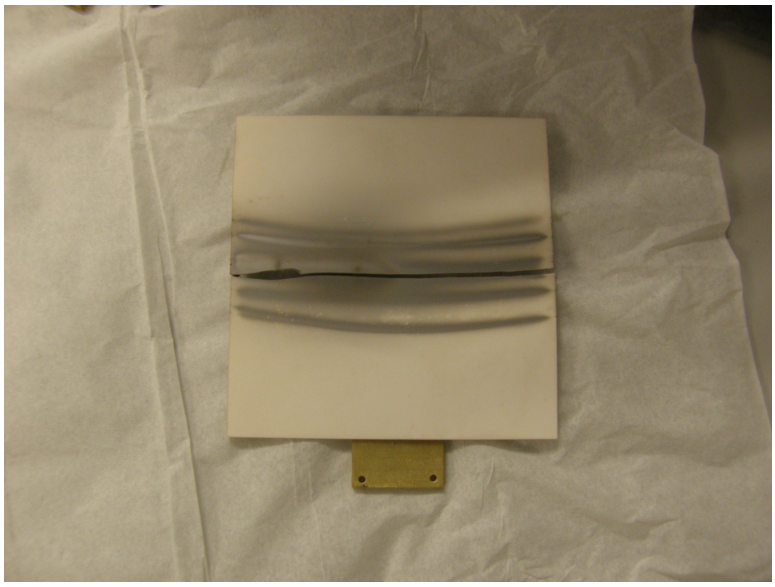

Figure 6.17: Post-test photo of fractured alumina wall material sample. Significant re-deposition of the wall filament material is visible.

Wall Filament Oscillations

In order to search for a signature of any periodic phenomena in the sheath such as the electron emission observed in the GWU PIC simulation, time-resolved measurements of the floating voltage of the high and low leads of the wall filaments were recorded. The filament floating voltage was measured on a Teledyne LeCroy HDO6104 oscilloscope with 100 MHz bandwidth 100:1 attenuation voltage probes. Figure 6.18 shows a power spectrum obtained from a DFT of a typical collected trace. No spectral windowing is used in the DFT beyond the normal rectangular windowing.

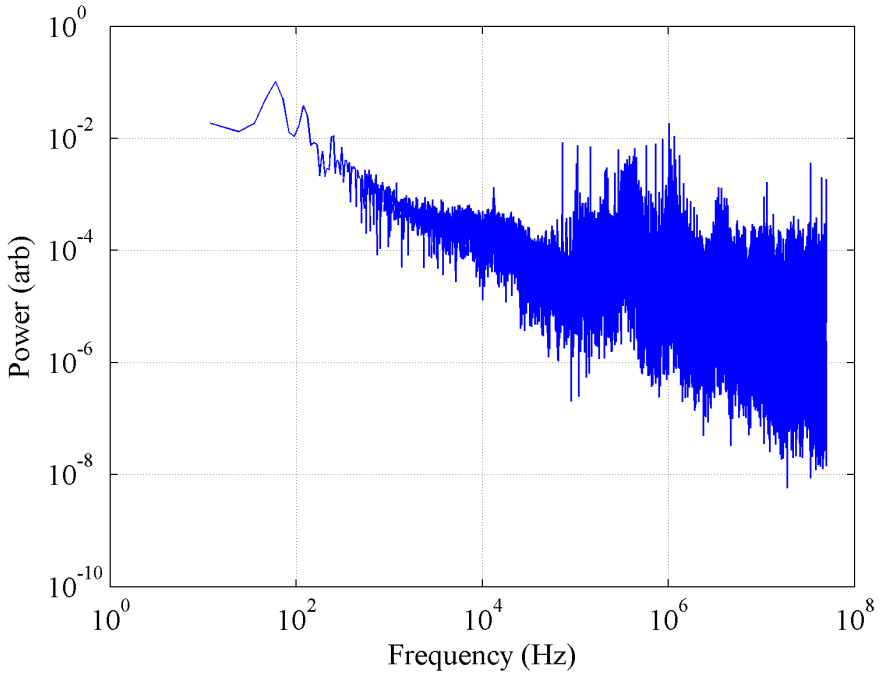

Figure 6.18: Power spectrum obtained from a discrete Fourier transform (DFT) of a typical collected trace of the wall filament floating voltage. Argon plasma, pressure 1 x 10^{-4} Torr-Ar, discharge current = 10 mA.

The 60 Hz ripple from the wall power supply dominates the power spectrum at low frequencies and there is substantial power in the high-frequency components > 100 kHz. The low-KHz range of the signal is comparatively quiet, however there is a small peak located at 13.3 kHz.

Figure 6.19 shows an average of the power spectra obtained from eight DFT's

collected at varying plasma cell discharge voltages. Some of the noise is reduced and the peak at 13.3 kHz is more prominent. A zoomed in view of the 13.3 kHz peak is shown in Figure 6.20. Though small in magnitude, this peak could be due to the small voltage fluctuations caused by a periodic electron emission mechanism such as the one in the GWU simulation. In the simulation, the emission plasmoids are periodic at about 25 kHz, so they are in roughly the same frequency range as the experimentally observed signature.

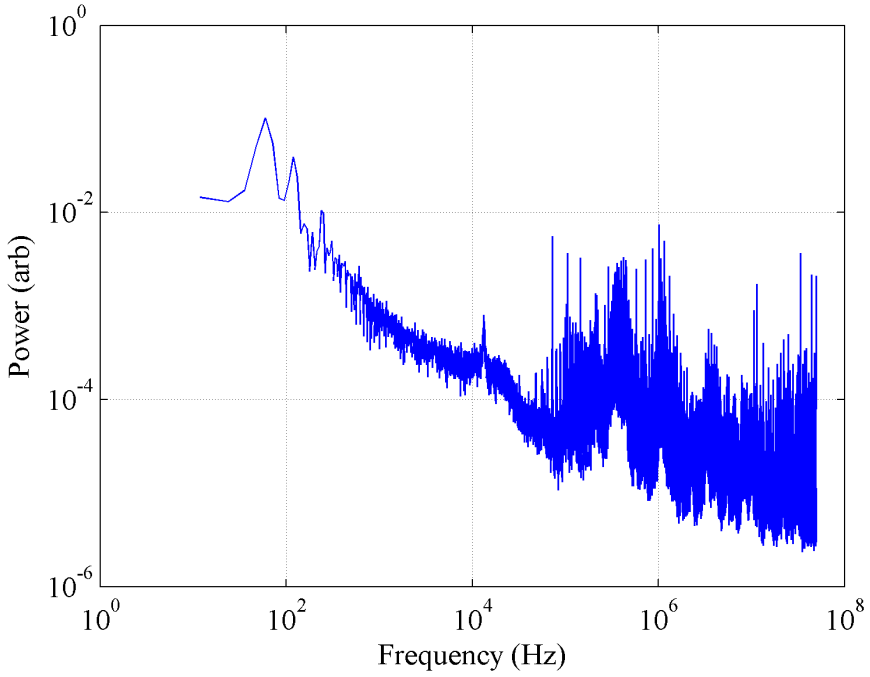

Figure 6.19: Averaged power spectrum obtained from eight DFT's of the wall filament floating voltage. Argon plasma, pressure 1 x 10^{-4} Torr-Ar, discharge current = 10 mA.

6.4 Discussion

These results have resolved the transition of the sheath potential profile to the collapsed high-emission regime. In Figure 6.11, it is shown that the increasing the primary electron energy continues to decrease the sheath potential until it is within the measurement error. This goes beyond the "space-charge-limit" of the Hobbs and

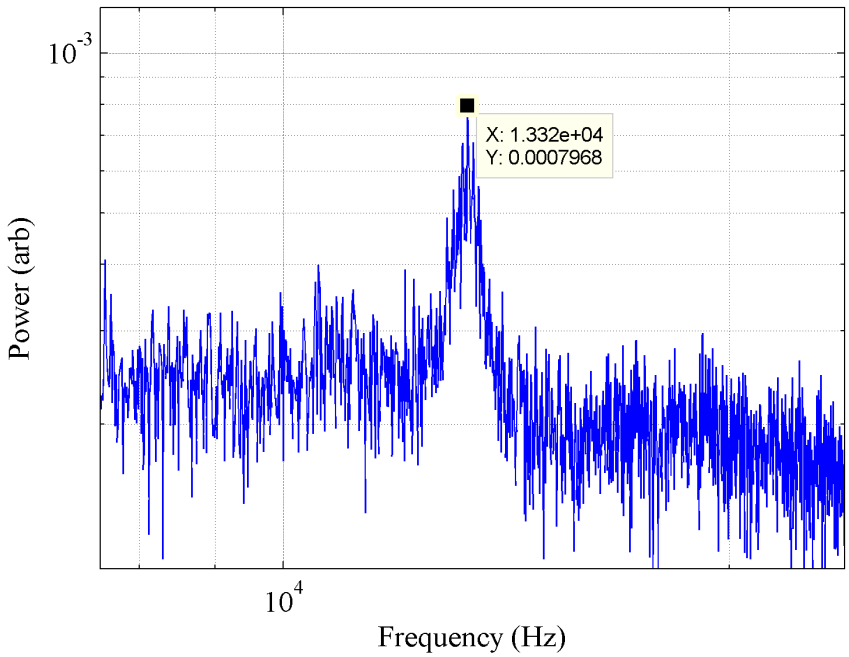

Figure 6.20: Zoomed in view of the averaged power spectrum to show the peak at 13.3 kHz. Argon plasma, pressure 1 x 10^{-4} Torr-Ar, discharge current = 10 mA.

Wesson theory, which if directly applied does not predict sheath potentials decreased below $\approx 1T_e$. Due to the energetic electron population, this may not be altogether surprising – the Hobbs and Wesson model is derived assuming a Maxwellian plasma with a single electron temperature, and no energetic electron population. However, this result does underscore that the moniker of "space-charge-limited" sheath that has been applied to the Hobbs and Wesson results should not be taken as an unbreakable physical limit applicable to all emitting-wall sheaths in all plasmas.

The sheath results do not resolve the presence of any virtual cathode-type potential dip structures near the wall boundary. This could be due to limited measurement resolution in the near wall region, or it could be the case that in these plasma conditions a virtual cathode does indeed not form. It looks like there may be the start of a virtual cathode in the high energy condition with the BN wall, however it is within the experimental error in determining the potential.

A piece of information that cannot be directly determined from the observations is

the energy distribution of the emitted electrons. Secondary electrons are generally assumed to be low temperature – in Hall effect thrusters, the secondary electrons can cause a cooling effect on the global electron temperature of the thruster as they thermalize with the bulk plasma electrons. Detailed models for the energy distribution of secondary electrons [35, 97] often include a contribution of elastically reflected electrons returning to the plasma with no energy loss – it is possible that this population plays a significant role.

Observed Deposition

The observed deposition of tungsten from the wall filaments on the bulk substrate is very probably the reason for the great variation in observed sheath collapse voltage over the duration of the experiment in Figure 6.14 – Tungsten has a much lower SEE yield than alumina, which would have the observed effect of postponing the sheath collapse to higher energy. This finding, while it was not the original goal of the experiment, illustrates the surface sensitivity of the sheath collapse with SEE and is interesting for electric propulsion ground testing applications. Ground test of thrusters typically results in considerable deposition of sputtered material in the thruster discharge channel. The sputtered material originates from the facility surfaces impacted by the energetic ion plume of the thruster, usually a set of graphite baffles termed a "beam dump". This deposition is not observed in regions where the thruster ions are actively eroding the wall during operation – the local sputtering rate of the thruster ion plume exceeds the redeposition rate, and the new ceramic is continually exposed keeping the surface "clean". Redeposition from sputtering of the vacuum facility would not occur in a flight thruster on orbit if the plume is unobstructed, which could impact the SEE yield of the channel wall and the overall operation and performance of the thruster.

Electron Emission

Figure 6.16 shows that as the filament heating current is increased, the floating potential of the wall filaments is driven more positive, in line with theoretical expectation. The floating potential is always seen to increase with conditions that would cause increased electron emission, whether through increasing the filament heating current to increase thermionic emission from the filaments, or by increasing the electron energy of the plasma cell population to increase secondary electron emission from the alumina.

The sheath "collapse" with increasing emission still occurs at low filament heating currents, similar to previous experiments and modeling (Chapters 4 and 5). At high heating currents, the sheath is always "collapsed" for all values of the plasma electron energy, and the result of increasing primary electron energy is a monotonic increase in floating potential.

Having the wall filaments emitting along the surface of the wall provides an interesting window into the behavior of the emissive sheath. As shown in Figure 6.16, fluctuations in the wall filament floating potential are visible when a Langmuir probe is being swept in the plasma. The Langmuir probe was located 100 mm from the wall when the sweeps causing the perturbations were taken. The perturbations are strongest in the 1 A case at plasma conditions where the sheath is almost collapsed, or in the gradual transition region towards collapse.

These results of floating potential of the heated wall filaments are similar to the results observed with alumina for large beam energies (c.f. Figure 6.11,) in which the sheath potential collapses to almost zero within the measurement resolution. These results, driven by thermionic emission rather than solely secondary emission, confirm that the sheath is not fully collapsed when it has decreased to a potential of order of 1 T_e. These results combined with the near-flat sheath potential profile measured at high electron emission (*c.f.* Figure 6.11) indicates that in cases of strong emission, the sheath may assume a shape more similar to the monotonic "inverse sheath", rather

than a non-monotonic profile with an inverse sheath near the wall, a potential well, and an electron-repelling region outside of that.

Oscillations

The observed oscillations peak at 13 kHz is similar to oscillations in the Beam Electron Emission regime of the sheath seen in the GWU PIC simulation. Figure 6.21 shows a time series of the floating wall potential and snapshots of the sheath profile at certain times.

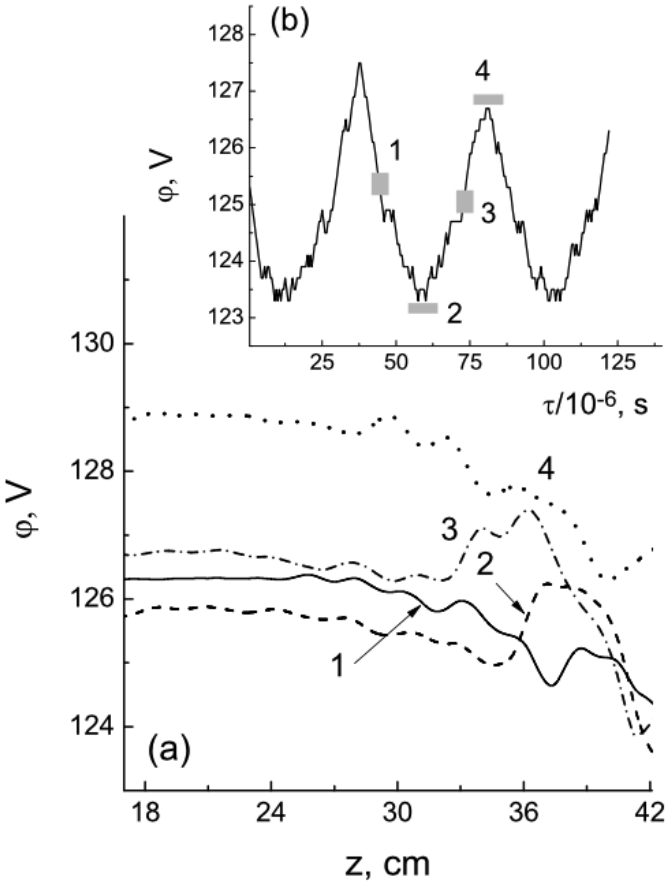

Figure 6.21: From GWU PIC simulation, Ref. [82], Figure 2, time series of the floating wall potential and snapshots of the sheath profile at certain times.

The frequency of oscillations in the GWU simulation is about 25 kHz, which is within a factor of two of the observed oscillation.

In light of the many interesting features of this dataset, it is desirable to compare the data with theoretical models of the problem and plasma simulations to understand and generalize the results. Chapter 6.4.1 gives comparison with simulation by our collaborators at GWU, and Chapter 7 compares the data to kinetic emitting-wall sheath models from literature.

6.4.1 Comparison with GWU Simulation

In order to be able to generalize and broadly apply the results of the plasma cell experiments, particularly the results regarding secondary electron emission obtained in the previous chapter, the experimental data was fed to our collaborators at GWU. GWU performed a detailed kinetic simulation of the experimental conditions using the PIC method with Monte Carlo collisions (MCC). The simulation reproduced many features of the experiment. Their simulation setup and results are briefly summarized below – for more details, the reader may refer to their publication on the subject [82].

Setup

The PIC-MCC model used by GWU tracks particles for both the electrons and ions. The model is two-dimensional with cylindrical symmetry and the electron and ion energy distribution functions (EEDF's and IEDF's) are three-dimensional in terms of velocity and two-dimensional in space (known as 2D3V). The energy distribution functions are found from the Boltzmann equations

$$\frac{\partial f_{\mathrm{i}}}{\partial t} + \vec{v_{\mathrm{i}}}\frac{\partial f_{\mathrm{i}}}{\partial \vec{r}} - \frac{e\vec{E}}{m_{\mathrm{i}}}\frac{\partial f_{\mathrm{i}}}{\partial \vec{u_{\mathrm{i}}}} = Q_{\mathrm{i}} \tag{6.1}$$

$$\frac{\partial f_{\mathrm{e}}}{\partial t} + \vec{v_{\mathrm{e}}}\frac{\partial f_{\mathrm{e}}}{\partial \vec{r}} - \frac{e\vec{E}}{m_{\mathrm{e}}}\frac{\partial f_{\mathrm{e}}}{\partial \vec{u_{\mathrm{e}}}} = Q_{\mathrm{e}} \tag{6.2}$$

where $\vec{u_{\mathrm{e}}}$, $\vec{u_{\mathrm{i}}}$, m_{e} and m_{i} are the electron and ion velocities and masses respectively; Q_{e} and Q_{i} are the collisional integrals for electrons and ions with background atoms at specified pressure. The floating potential of the wall material sample is found from

the zero net current condition of charged particle flux to the wall. In the simulation, the discharge chamber is smaller than in the experiment (r = 20 cm and h = 50 cm in the simulation, vs. r = 29 cm and h = 91 cm in the experiment) and the magnetic multipole boundary is not modeled. Data from literature is used for the alumina SEE yield [95] and the energy distribution of the emitted electron is specified as a half-Maxwellian distribution with a temperature 0.1-0.5 eV.

Results

The GWU model results, the SEE yield relation used for alumina adapted from [95], and comparison of sheath profiles to experimental data are shown in Figures 6.22a), 6.22b), and 6.23 respectively. The model achieves excellent agreement in several ways – the sheath potentials and thicknesses are in the same range as the experiment. The observed phenomenon of the sheath collapse is also captured.

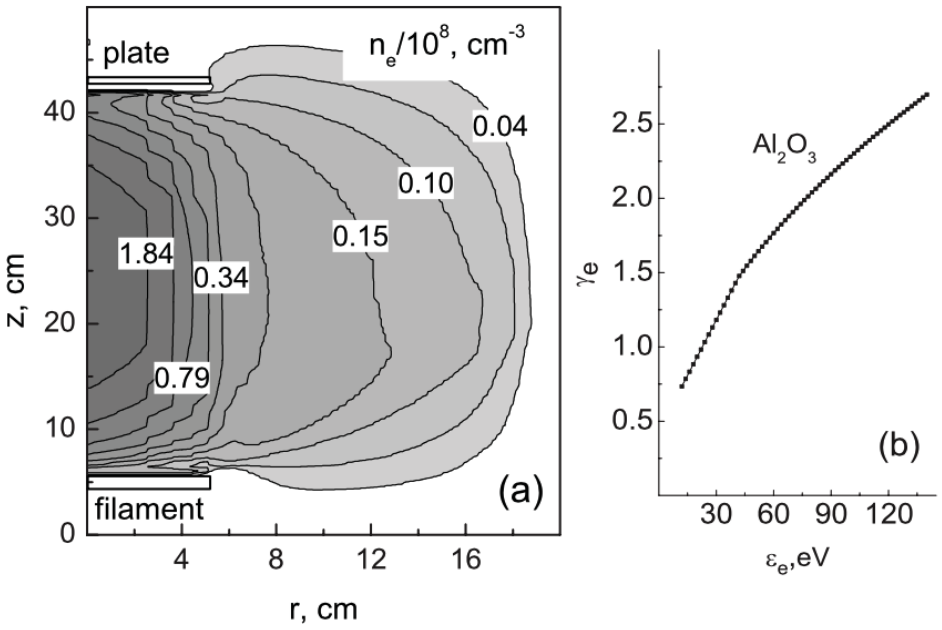

Figure 6.22: From Ref. [82], Figure 2, GWU simulation domain, electron density results, and alumina SEE yield data used. Data shown for I_D = 30 mA, V_D = -70 V.

Despite the broad agreement between experiment and simulation, there are some remaining fine discrepancies. In the experiment, the sheath potential and thickness

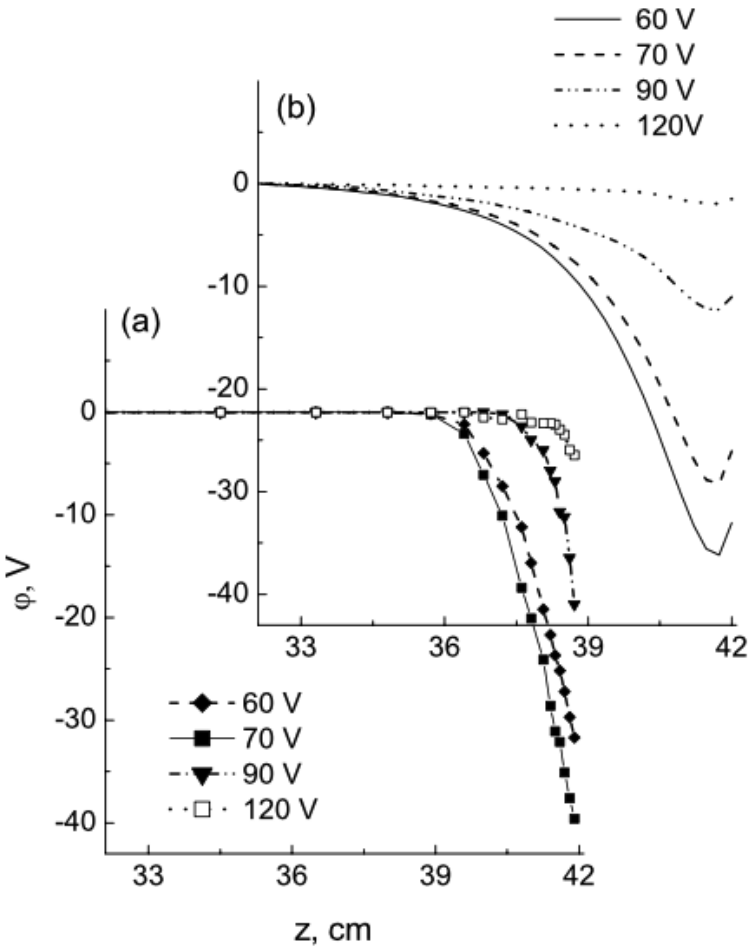

Figure 6.23: From Ref. [82], Figure 4, comparison of GWU simulation and GT experimental data. Measured (a) and calculated (b) potential distributions for V_{D} = -60, -70, -90 and -120 V at I_{D} = 10 mA.

increases when increasing the electron energy from 60 V to 70 V. In the simulation results, the reverse trend is true, and the sheath potential falls. This disagreement is more pronounced in the simulations at 40 mA discharge current, in which the experiments finds increasing sheath potentials up to 90 V and the simulation always shows decreasing. In addition, the simulation shows the presence of a virtual cathode potential structure at all conditions with significant SEE, which is not resolved in the experiment.

Discussion

In the classic simulation vs. experiment dichotomy, the simulation has perfect diagnostics of an imperfect physics, and the experiment has imperfect diagnostics of perfect physics. The GWU team is able to take advantage of the former to provide some interesting insights into the emitting-wall sheath problem as modeled.

Firstly, they observe an intermediate sheath regime to the two sheath regimes observed in experiment (non-collapsed, collapsed.) They term the intermediate regime the "beam-electron emission" or BEE regime, and in it they observe significant electron emission and a virtual cathode potential structure, but still at relatively high sheath potentials compare to the non-collapsed Child-Langmuir / Debye sheath regime. The emitted electrons are initially low temperature, but are then accelerated out of the sheath, thus forming the beam-like emission. This in an interesting result that is somewhat in conflict with the classical Hobbs and Wesson model. In the Hobbs and Wesson model, the electric field at the wall does not vanish and allow for the formation of a virtual cathode until the emission yield has nearly reached unity and the sheath potential has collapsed to $\approx\ 1\ T_{\mathrm{e}}$. In addition, they observe an oscillatory behavior of the electron emission, where the electron population near the wall builds up to a critical density where it is able to effect the potential structure, and then is emitted in a packet or burst emission to the plasma. Given the promising agreement of the

simulation with experiment so far, it is good reason for future experimental work to look for some of these features, and to theoretically consider why it is that the H&W model does not predict a virtual cathode where the simulation does.

CHAPTER VII

KINETIC THEORY ANALYSIS

The results of the experiments with secondary electron emission showed the influence of the energetic primary electron population at low plasma density conditions in the plasma cell. In particular, these energetic populations showed the strong ability to influence the wall floating potential despite the relatively low number density in respect to the ionization electrons.

In an attempt to more quantitatively understand the effect the energetic population was having on the plasma, we performed a literature search and a comparison to an applicable theoretical model of the emitting wall sheath problem. Fluid theories such as the classical Hobbs and Wesson model contain no mechanism for introducing energetic populations with non-Maxwellian energy distributions, so we selected a kinetic model.

7.1 Formulation

The emitting sheath problem has been analyzed using kinetic theory by Schwager [81], Sheehan [87], and quite recently Rizopoulou [80]. For comparison with our experimental work, Sheehan's model is convenient because it does not include the artificial "source sheath" that the other models employ to enable comparison with PIC simulations. We do not use Sheehan's model directly because it does not include a distribution function for the isotropic primary electrons that we find experimentally. These are electrons accelerated into the plasma device to a set energy, and confined through multiple bounces off of magnetic cusps such that their directionality is lost and their velocity distribution function (VDF) forms a spherical shell. We give the model formulation in this section, largely due to Sheehan and incorporating wall

material-SEE yield relations and a different form of electron energy distribution to include the isotropically distributed electrons observed in this plasma device.

It is assumed that the sheath is 1D, collisionless, free of ionization and recombination, free of magnetic fields, and composed solely of electrons and singly charged ions with mass ratio $\mu = m_{\mathrm{i}}/m_{\mathrm{e}}$. We consider the plasma electrons as a Maxwellian population at temperature T_{ep} and an isotropic monoenergetic population at energy E_{ei}. The emitted secondary electrons are considered to be half-Maxwellian at T_{ee}. Due to the low electron density/plasma frequency in the sheath (minimum wavelength for streaming instability [50] greater than sheath thickness), we neglect the effect of instabilities between the distribution functions and couple them solely through the jointly determined electric field. The plasma ions enter the sheath with a number density n_0 and a directed energy E_0 or $\epsilon = E_0/T_{\mathrm{ep}}$ towards the wall. The wall floats to the potential that balances positive and negative charge fluxes, $\phi_{\mathrm{w}} = \phi_{\mathrm{f}}$. The wall emission is set by the secondary electron yield γ, the average number of emitted electrons per incident electron. This sheath has no sources and no sinks of particles except at the boundaries, so the system is an electrostatic Vlasov-Poisson system and the distribution functions do not change along the trajectories in phase space. Acceleration is due to the electric field only so the trajectory in (ϕ, u) space is known if the velocity at the boundary is known. Therefore, if the distribution function is known at the boundaries, the sheath can be fully solved. The electron distribution functions are given in Eqs. 7.1 - 7.3 and illustrated in Figure 7.1.

$$f_{\mathrm{ep}}(u,\Phi) = \begin{cases} 0 & u \le u_{\mathrm{w}} \\ \sqrt{\frac{m_{\mathrm{e}}}{2\pi T_{\mathrm{ep}}}}\exp\left(-\frac{m_{\mathrm{e}}u^2}{2T_{\mathrm{ep}}} - \Phi\right) & u > u_{\mathrm{w}} \end{cases} \tag{7.1}$$

$$f_{\mathrm{ee}}(u,\Phi) = \begin{cases} \sqrt{\frac{2m_{\mathrm{e}}}{\pi T_{\mathrm{ee}}}}\exp\left(-\frac{m_{\mathrm{e}}u^2}{2T_{\mathrm{ee}}} + \Theta\left(\Phi_{\mathrm{w}} - \Phi\right)\right) & u \le u_{\mathrm{w}} \\ 0 & u > u_{\mathrm{w}} \end{cases} \tag{7.2}$$

$$f_{\mathrm{ei}}(u,\Phi) = \begin{cases} 0 & u \le u_{\mathrm{w}} \\ \frac{1}{u_{\mathrm{w}}(\Phi)+u_{\mathrm{ei}}(\Phi)} & u_{\mathrm{w}} < u < u_{\mathrm{ei}} \\ 0 & u \ge u_{\mathrm{ei}} \end{cases} \tag{7.3}$$

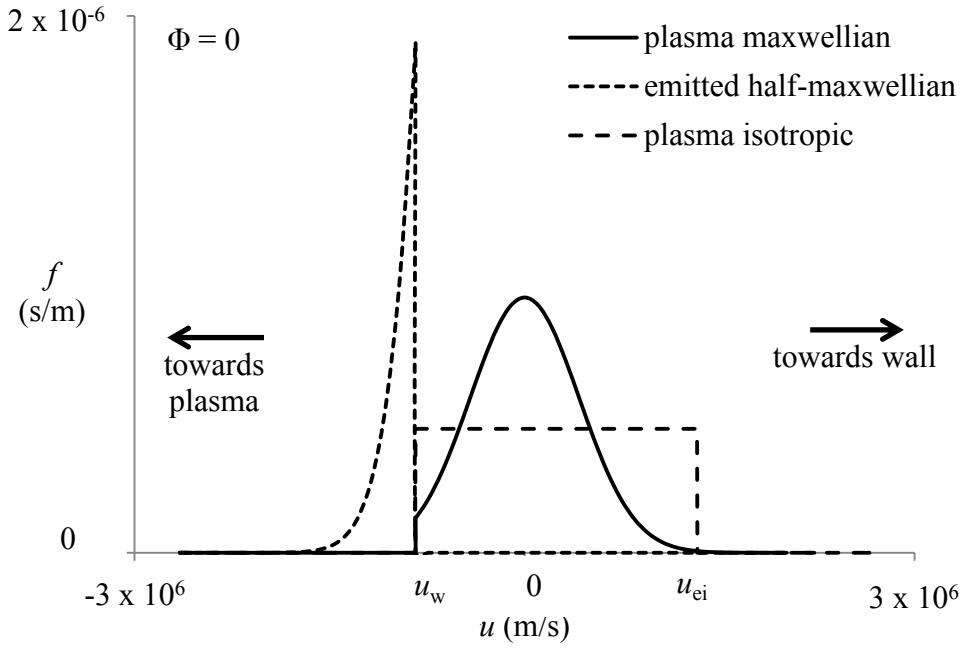

Figure 7.1: Velocity distribution functions used in model for plasma electrons f_{ep}, emitted electrons f_{ee}, and isotropic energetic electrons f_{ee}, shown at $\Phi = 0$ (sheath edge).

Equation 7.1 is the Maxwellian plasma electrons, repelled from the wall by the sheath potential. Equation 7.2 is a half-Maxwellian distribution of the emitted electrons from the wall, accelerated away from the wall by the sheath potential. Equation 7.3 is the isotropic primary electrons, which form a uniform distribution in 1D as can be shown by integrating the spherical shell VDF over the non-normal dimensions. Electrons with sufficient velocity to reach the wall are depleted from the tails of the distribution functions, so the equations are piecewise in velocity according to Equations 7.4 and 7.5.

$$u_{\mathrm{w}}(\Phi) = \sqrt{\frac{2T_{\mathrm{ep}}}{m_{\mathrm{e}}}\left(\Phi_{\mathrm{w}} - \Phi\right)} \tag{7.4}$$

$$u_{\mathrm{ei}}(\Phi) = \sqrt{\frac{2T_{\mathrm{ep}}}{m_{\mathrm{e}}}\left(\Phi_{\mathrm{ei}} - \Phi\right)} \tag{7.5}$$

In Figure 7.1 and Eqs. 7.2 and 7.4, $\Phi_{\mathrm{w}} = E_{\mathrm{w}}/T_{\mathrm{ep}}$, where E_{w} is the energy required to reach the wall. The emitted electron distribution f_{ee} is specified by the temperature ratio $\Theta = T_{\mathrm{ep}}/T_{\mathrm{ee}}$. The isotropic electron distribution f_{ei} is specified by the energy $\Phi_{\mathrm{ei}} = E_{\mathrm{ei}}/T_{\mathrm{ep}}$ and fraction $\alpha = n_{\mathrm{ei0}}/(n_{\mathrm{ei0}} + n_{\mathrm{ei0}})$. In this formulation, there are four unknown quantities: ϵ_0, Φ_{w}, and the normalization constants of the plasma and emitted electron distributions, which are the respective number densities. The number densities of the isotropic and Maxwellian plasma electrons are connected by the specification of α. We normalize the number densities of the plasma and emitted electron populations (n_{ep0} and n_{ee0}) at the boundary with respect to the ion number density n_0 as $N_{\mathrm{ep0}} = n_{\mathrm{ep0}}/n_0$ and $N_{\mathrm{ee0}} = n_{\mathrm{ee0}}/n_0$. To solve for the unknowns, we enforce the following constraints: quasineutrality at the sheath edge (7.6), the floating condition for balanced charge flux to the wall (7.7), the secondary emission yield relation between electron fluxes to and from the wall (7.8), and the marginal generalized Bohm criterion (7.9).

$$0 = 1 - N_{\mathrm{ep0}} - N_{\mathrm{ee0}} - \left(\frac{\alpha}{1-\alpha}\right) N_{\mathrm{ep0}} \tag{7.6}$$

$$\begin{aligned} 0 = 1 - \frac{1}{\sqrt{\pi}} \frac{\exp\left(-\Phi_{\mathrm{w}}\right)\sqrt{\mu/\epsilon}}{2 - \mathrm{erfc}\left(\sqrt{\Phi_{\mathrm{w}}}\right)} \left(N_{\mathrm{ep0}}\right) + \frac{1}{\sqrt{\pi\Theta}} \frac{\exp\left(-\Phi_{\mathrm{w}}\Theta\right)\sqrt{\mu/\epsilon}}{\mathrm{erfc}\left(\sqrt{\Phi_{\mathrm{w}}\Theta}\right)} \left(N_{\mathrm{ee0}}\right) \\ - \frac{1}{2}\left(\frac{\Phi_{\mathrm{ei}} - \Phi_{\mathrm{w}}}{\sqrt{\Phi_{\mathrm{ei}}} + \sqrt{\Phi_{\mathrm{w}}}}\right)\left(\frac{\alpha}{1-\alpha}\right)\left(N_{\mathrm{ep0}}\right) \end{aligned} \tag{7.7}$$

$$\begin{aligned} 0 = 0 - \frac{\gamma}{\sqrt{\pi}} \frac{\exp\left(-\Phi_{\mathrm{w}}\right)\sqrt{\mu/\epsilon}}{2 - \mathrm{erfc}\left(\sqrt{\Phi_{\mathrm{w}}}\right)} \left(N_{\mathrm{ep0}}\right) + \frac{1}{\sqrt{\pi\Theta}} \frac{\exp\left(-\Phi_{\mathrm{w}}\Theta\right)\sqrt{\mu/\epsilon}}{\mathrm{erfc}\left(\sqrt{\Phi_{\mathrm{w}}\Theta}\right)} \left(N_{\mathrm{ee0}}\right) \\ - \frac{\gamma}{2}\left(\frac{\Phi_{\mathrm{ei}} - \Phi_{\mathrm{w}}}{\sqrt{\Phi_{\mathrm{ei}}} + \sqrt{\Phi_{\mathrm{w}}}}\right)\left(\frac{\alpha}{1-\alpha}\right)\left(N_{\mathrm{ep0}}\right) \end{aligned} \tag{7.8}$$

$$0 = \frac{1}{2\epsilon} - \left(\frac{1}{\sqrt{\pi}} \frac{\exp\left(-\Phi_w\right)}{\sqrt{\Phi_w}(\text{erfc}\left(\sqrt{\Phi_w}\right) - 2)} - 1 \right) (N_{ep0}) - \left(\frac{\Theta}{\sqrt{\pi}} \frac{\exp(-\Phi_w\Theta)}{\sqrt{\Phi_w\Theta}\text{erfc}(\sqrt{\Phi_w\Theta})} - \Theta \right) (N_{ee0}) + \frac{1}{2} \left(\frac{1}{\sqrt{\Phi_{ei}\Phi_w}} \right) \left(\frac{\alpha}{1-\alpha} \right) (N_{ep0}) \quad (7.9)$$

In each of equations 7.6 - 7.9, the four terms on the right hand side represent the contributions of the plasma ions, plasma Maxwellian electrons, emitted electrons, and plasma isotropic electrons, respectively. The equations are nonlinear but smooth, and thus can be solved numerically. Once the unknowns ϵ, Φ_w, N_{ep0}, and N_{ee0} are obtained, the sheath potential profile can be computed by integrating the electrostatic Poisson equation.

7.2 Results

Figure 7.2 below shows a result of this analysis, which is that the isotropic monoenergetic electron population can dictate the wall floating potential if it has sufficient energy and number density. As γ increases, the electric field at the wall decreases until it reaches zero at a critical $\gamma = \gamma_c$ (close to unity).

Figure 7.2 shows the effect of the isotropic monoenergetic electron population on the wall floating potential. For a non-zero α, as Φ_{ei} increases, Φ_w must increase to repel the energetic electrons and maintain balanced charge fluxes to the wall. At high Φ_{ei}, the effect is similar to that of a directed beam of electrons as nearly all of the electrons have sufficient energy to impact the wall. The beam cannot push the floating potential higher than its energy at $\Phi_{ei} = 50$. The fraction of energetic electrons α effects the change in floating potential with γ: at low α, the floating potential decreases gradually as gamma increases, and at high α, the decrease occurs sharply. If γ is known as a function of incident energy, it can be determined for a given plasma condition. Figure 7.3 shows the solutions for Φ_w using data from the literature for γ of a BN wall [98], [25].

Figure 7.5 compares the experimentally measured sheaths to the computed sheaths

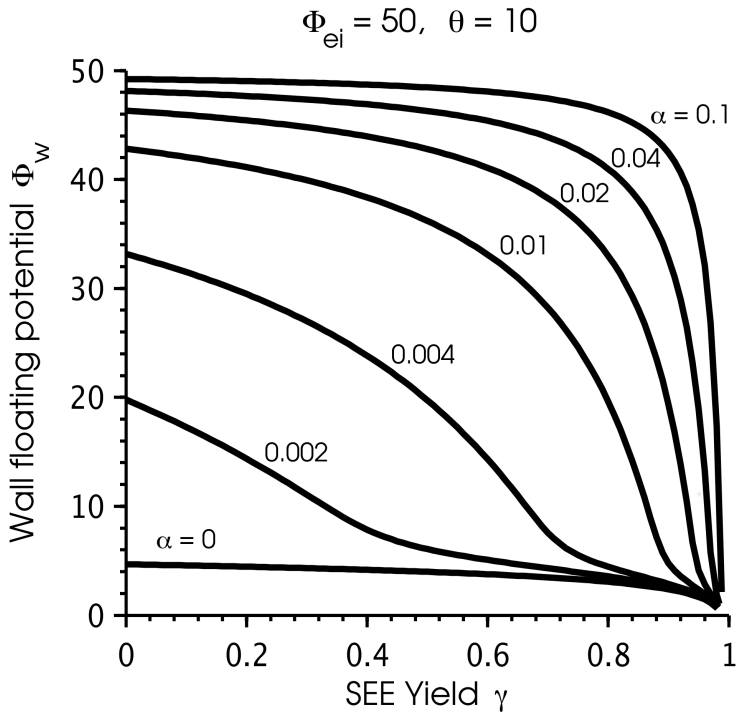

Figure 7.2: Model floating wall potential Φ_w with varied SEE yield γ and isotropic energetic electron fraction α.

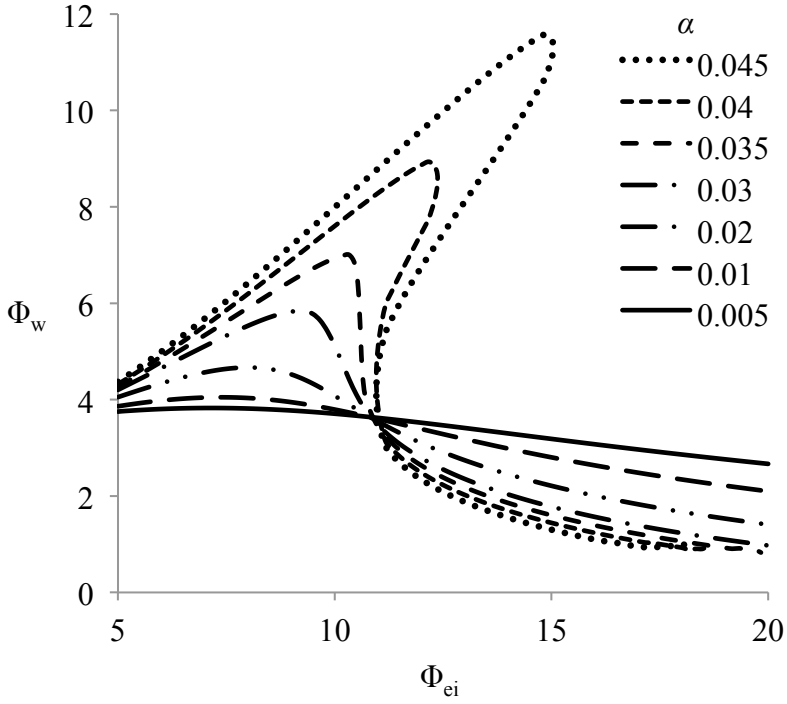

Figure 7.3: Model floating wall potential Φ_w with varied energetic isotropic electron energy Φ_{ei} and fraction α.

from the kinetic model using measured plasma parameters from the Langmuir probe. The fraction of energetic electrons α is calculated using the Langmuir probe data of Figure 6.1, and depends on Φ_{ei}. As the energy of the energetic isotropic electrons Φ_{ei} is increased, α is seen to decrease as shown in Figure 7.4.

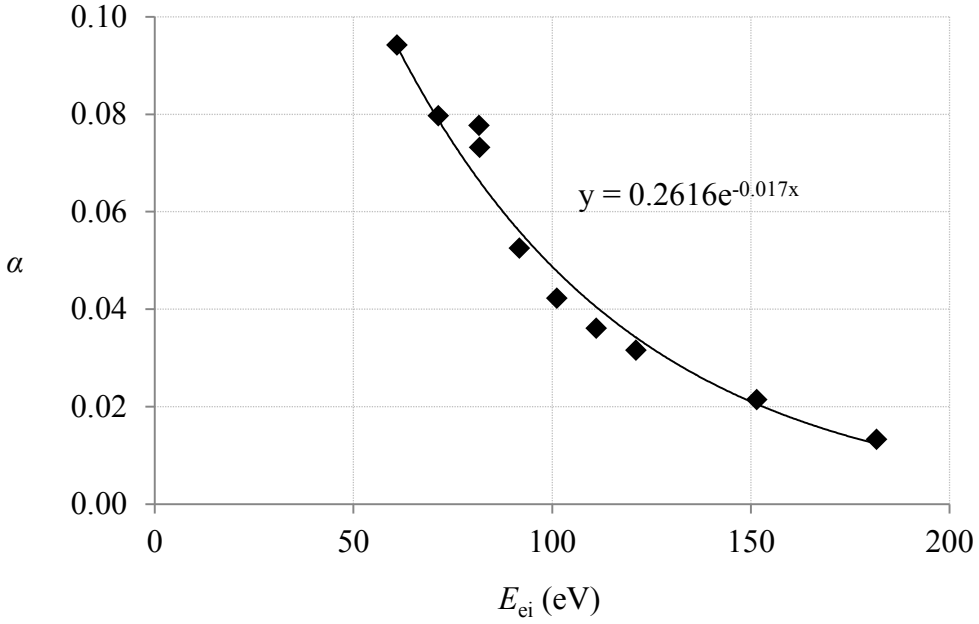

Figure 7.4: Determinations of experimental fraction of energetic electrons α from Langmuir probe data of Figure 6.1.

For comparing experimentally measured sheath profile to the model, the Debye length is calculated using a general form for multi-species plasma [[17], *c.f.* Appendix A.4] shown in equation (7.10).

$$\frac{1}{{\lambda_D}^2} = \sum^{\alpha} \frac{1}{\lambda_{d,\alpha}^2} = \frac{1}{\lambda_{d,cp}^2} + \frac{1}{\lambda_{d,hp}^2} \tag{7.10}$$

In equation (7.10), $\lambda_{d,cp}$ and $\lambda_{d,hp}$ are the Debye lengths calculated from the cold and hot plasma electron populations, respectively. We found that including the scarce energetic populations in the summation in equation (7.10) made a negligible difference. Agreement is good overall for the cases shown but failed for the 110 V and 130 V cases; the theory found multiple solutions. Inputs and outputs to the model are summarized in Table **??**.

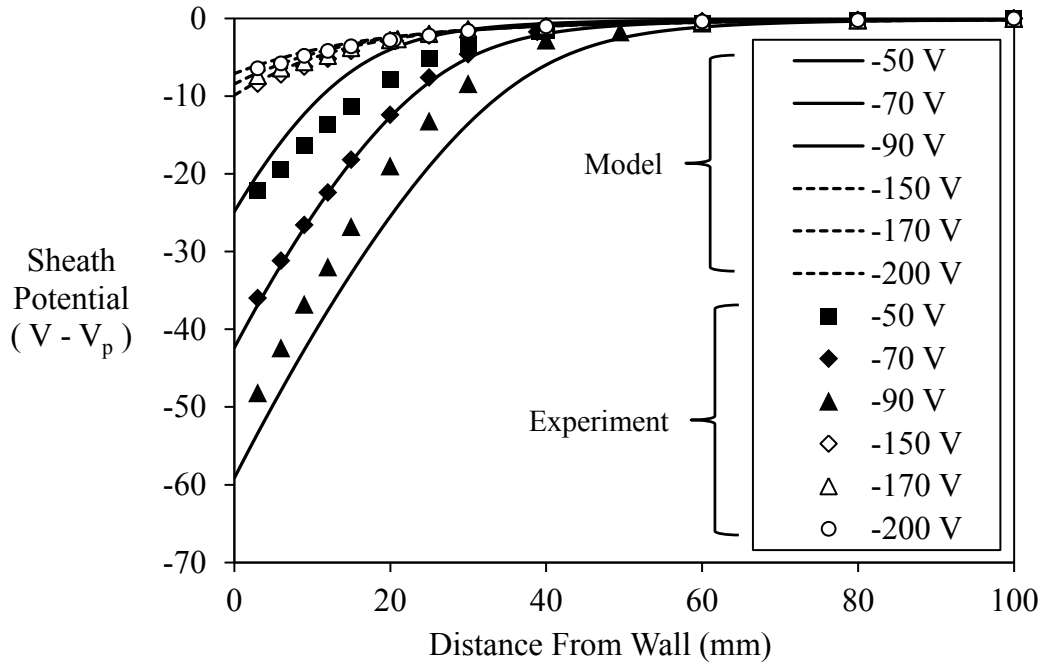

Figure 7.5: Model potential profiles compared to experimental results with BN data of Figure 9.5, where unique solutions were found from the model.

Table 7.1: Experimental measurements input to model, normalization parameters, and output for conditions shown in Figure 7.5.

Case	-50 V	-70 V	-90 V	-150 V	-170 V	-200 V
T_{ep} (eV)	3.485	3.510	3.506	5.803	5.289	5.481
λ_D (mm)	3.511	4.050	4.538	5.945	6.414	7.118
μ	72820	72820	72820	72820	72820	72820
α	0.1602	0.1092	0.0772	0.0284	0.0204	0.0124
Φ_{ei}	7.599	12.97	18.43	20.99	26.63	30.91
Φ_w	7.173	11.62	15.40	1.654	1.588	1.276
Φ_w model	7.130	12.05	16.84	1.502	1.403	1.484

7.3 Discussion

The solutions become multi-valued in some regions for $\alpha > 0.035$, exhibiting a S-curve hysteresis. This is similar to some hysteresis curves shown for targets in fusion plasmas where the transition is caused by heat flux driving thermionic emission [[92], [102]]. Here, it arises with a cold wall due to the high yield of the relatively scarce energetic isotropic electrons. The physical outcome is that there are multiple potentials the wall could assume and satisfy all of the constraints in the model (quasineutrality at sheath edge, charge flux conservation, SEE yield relation, and Bohm criterion). In practice, we expect that the solution branch that manifests physically will depend on the history of the plasma conditions in reaching that condition, for example, if Φ_i is started at a low value and steadily increased at $\alpha > 0.035$, the wall potential to follow the high potential branch until it enters the one-solution region at high Φ_i, manifesting in a step change in the wall potential.

The origin of this collapse / hysteresis behavior in this system is the interdependency of the sheath potential and SEE yield. There is a substantial difference between the collapsed and non-collapsed sheaths. In the non-collapsed sheath, the floating condition is largely enforced by equal flux of plasma ions and plasma electrons to the wall – any secondary electrons emitted from the wall are accelerated away from the wall into the plasma without strongly modifying the local space charge. In the transition to the collapsed sheath, enough SEE is being emitted that it begins to neutralize the sheath region and decrease the potential barrier. With the potential barrier weakened, electrons from the plasma are less slowed during their transit of the sheath and impact the wall with more energy, further increasing SEE. With a significant energetic electron population, this can cause the "collapse" behavior observed, in which the sheath potential magnitude rapidly falls until the collapsed equilibrium is reached. In the collapsed solution, the sheath potential magnitude has fallen enough that a significant fraction of the cold plasma electrons can stream to the wall. The

floating condition is enforced less by ion flux and increasingly by plasma electrons and opposing secondary electrons. Although a detailed exploration of the modeling was not done in the scope of work of this research, it seems that an energetic plasma electron population and a wall with positive-slope SEE yield curve will be necessary for hysteresis to occur in the system.

CHAPTER VIII

INFLUENCE OF WALL TEMPERATURE

Heat flux from dense plasmas can elevate nearby walls to high temperatures. Temperatures of 600-800 K are not uncommon, and temperatures as high as 1000 K have been measured in HET discharge channels [67, 68]. Having seen theoretically that energy distribution of emitted electrons is important to the sheath structure, the question of the influence of the wall temperature is important for thruster development.

8.1 Experimental Setup

A radiative sample heater is designed and built to heat wall material samples to thruster temperatures for testing in the plasma cell. A photo of the sample heater with a dummy graphite wall material sample is shown in Figure 8.1. The sample heater is a cube enclosing heating elements formed from 0.042-inch diameter tantalum wire and alumina tube supports. Because the heater wire is not directly adjacent to the wall material sample, the induced magnetic fields from the heater coil at the sample surface is of the order of Earth background field (0.5 G) and there is no worry of it influencing the sheath over the sample.

8.2 Results

First experiments with the sample heater were performed on the smooth and rough BN wall material samples. The results showed no change in the shape of the potential profiles, but they did show a change in the "transition voltage" of the energetic electrons at which the change from high, increasing sheath potential to low decreasing sheath potential took place, shown in Figure 8.2. In the first series of experiments, no procedure was performed before the experiments to clean the wall material sample

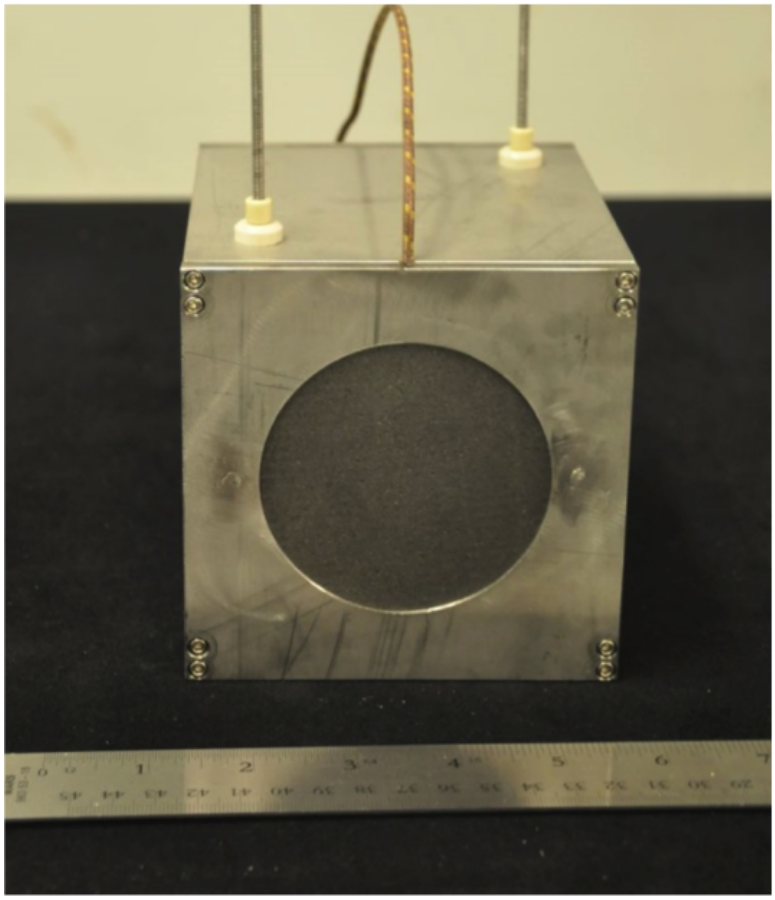

Figure 8.1: Photo of the sample heater with a dummy graphite wall material sample.

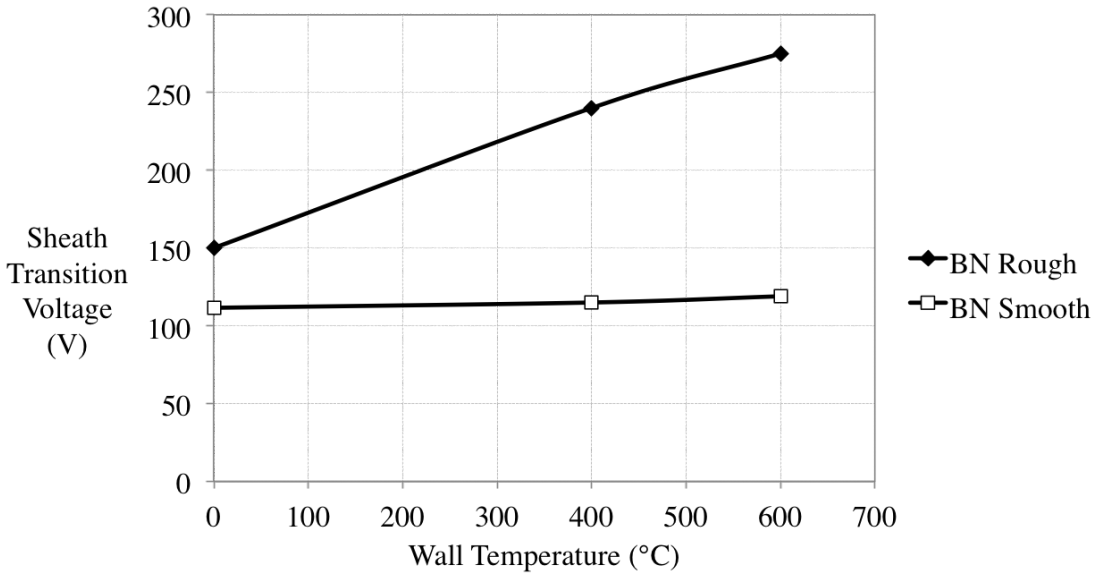

Figure 8.2: Primary electron energy required for sheath collapse vs. wall temperature, initial results. Argon plasma, pressure 1 x 10^{-4} Torr-Ar, discharge current = 10 mA.

surface from contaminants. In addition, data was collected without record of the history of plasma conditions, i.e., whether the filament bias voltage / bombarding electron energy was being increased or decreased when the measurement was taken. Given the multiple solutions of floating potential predicted by theory in the transition region (*c.f.* Figure 7.3), this may have effected the accuracy of the results. The

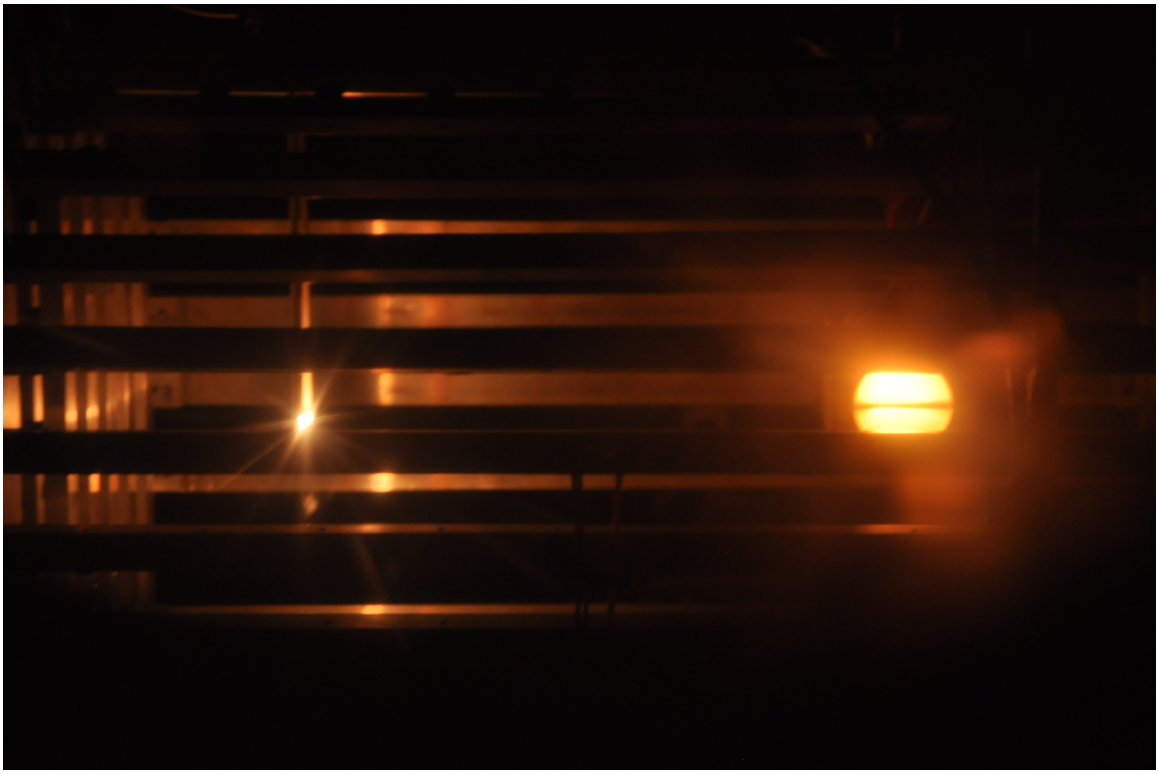

Figure 8.3: Plasma cell in operation with sample heater on. Argon plasma, pressure 1 x 10^{-4} Torr-Ar, discharge current = 10 mA.

experiments were repeated with a surface cleaning procedure and an automated data acquisition system to record the history of heater and plasma conditions. In these experiments, on advice from the materials group at UA, the plasma-facing surfaces of the wall material samples were cleaned by an acetone rinse, deionized water rinse, and sprayed dry with nitrogen. To monitor the floating potential of the wall, the emissive probe located 1 mm from the wall material sample at low heat, acting as a floating witness electrode for the wall potential. This close to the wall and below the plasma Debye length, the probe sheath is blended in with the sheath of the wall

material and the floating potential of the probe should be effectively the same as the wall floating potential. Experiments with a conductive LaB_6 wall material sample (Figure 8.4) confirmed that this method generally tracked the wall potential. These

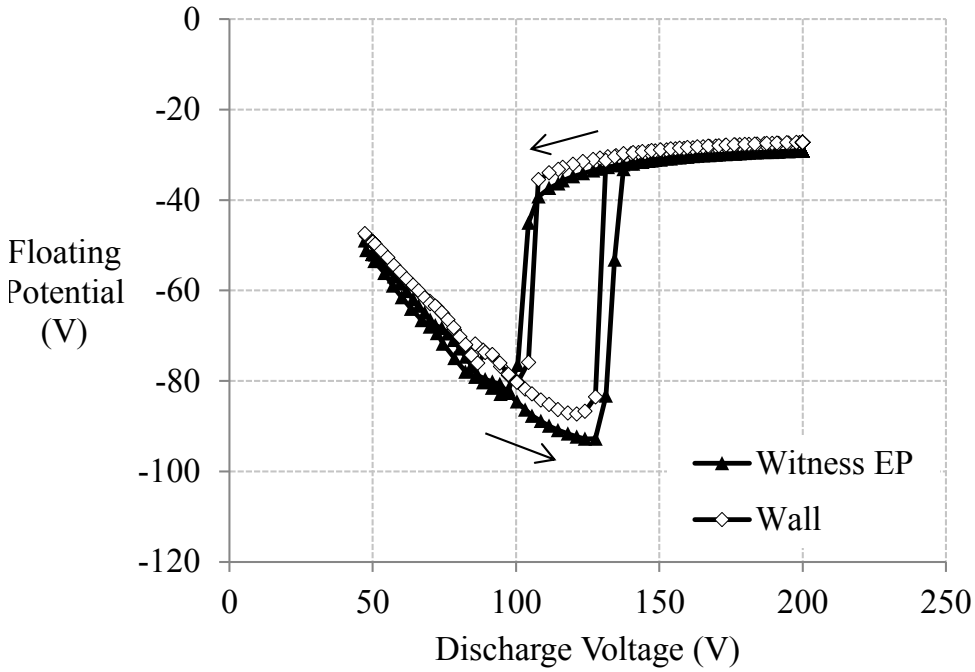

Figure 8.4: Witness emissive probe floating potential vs. LaB_6 floating potential.

more controlled experiments revealed significant outgassing from the wall material on initial heat-up. Figure 8.5 shows an observation of the rise in chamber backpressure caused by outgassing of the wall material samples and sample heater assembly during an initial heat-up. At peak, the observed pressures (uncorrected for gas type) represent approximately a 5 sccm gas load, indicating a significant removal of adsorbed gases from the heater assembly and samples. Initial experiments were performed on a steel sample which had been vacuum-sprayed with a LaB_6 coating. Figures 8.8 and 8.9 show a nominal scan of the wall floating potential taken with the witness emissive probe, as the discharge filament bias voltage / energy of the isotropic electron population is scanned from 50 to 200 V, first increasing from 50 to 200, then decreasing from 200 back to 50 V. The voltage is changed continuously at a rate of approximately 1 V/s

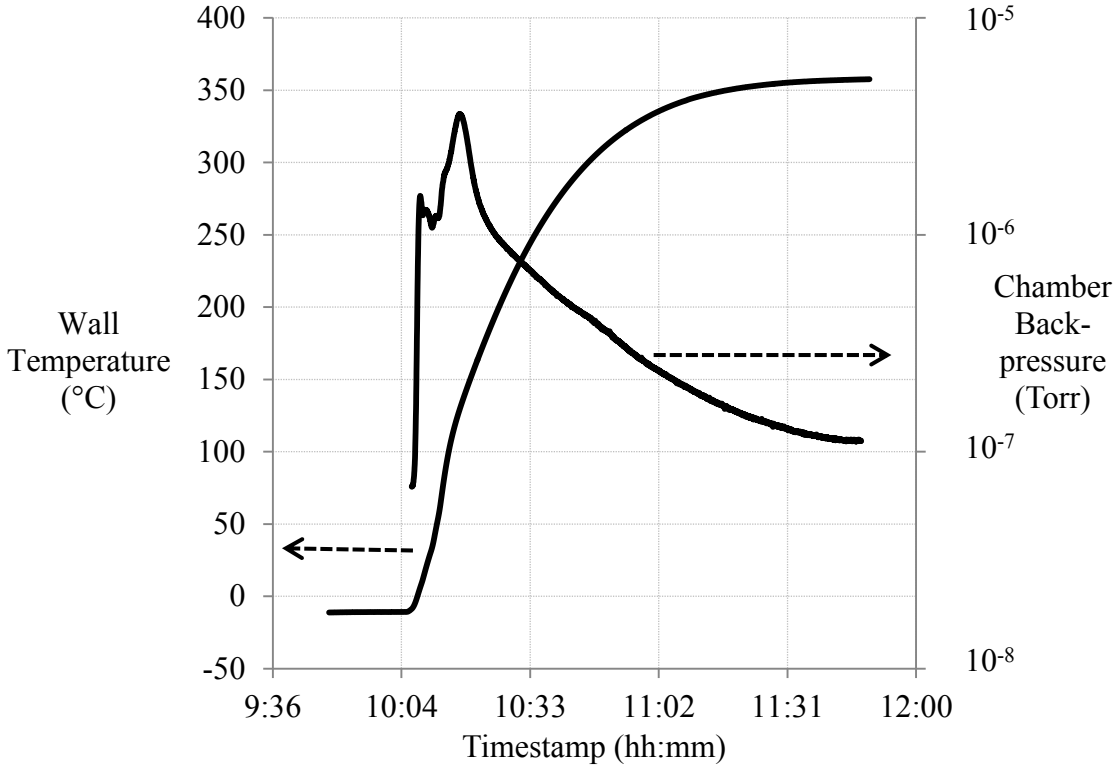

Figure 8.5: Rise in chamber backpressure (uncorrected for gas type) observed while heating samples at vacuum with 2 cryopumps active.

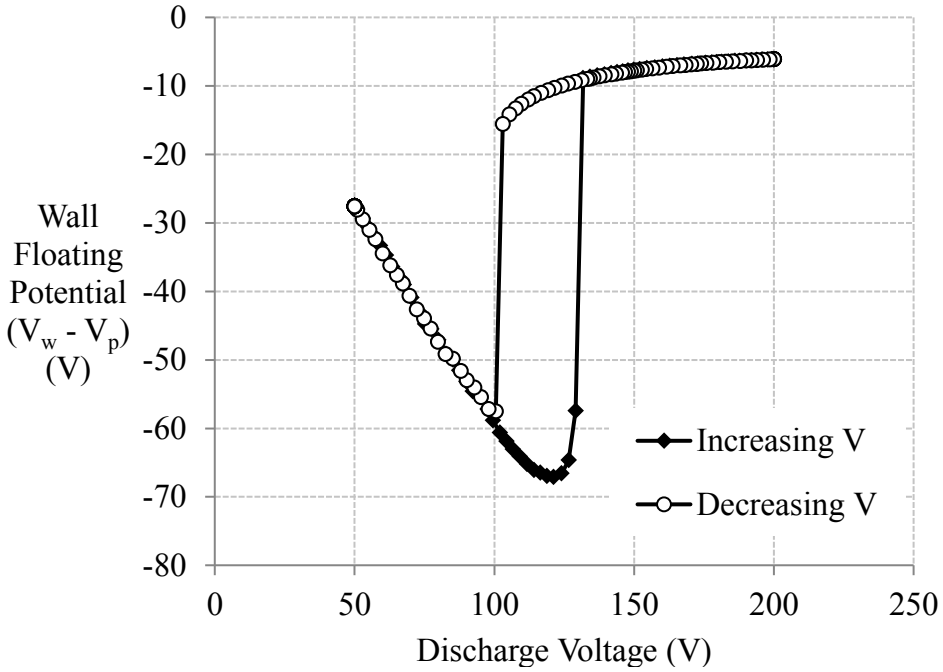

Figure 8.6: Filament bias voltage vs. floating sheath potential of LaB_6-coated steel sample. Argon plasma, pressure 1 x 10^{-4} Torr-Ar, discharge current 10 mA, wall temperature 50 °C.

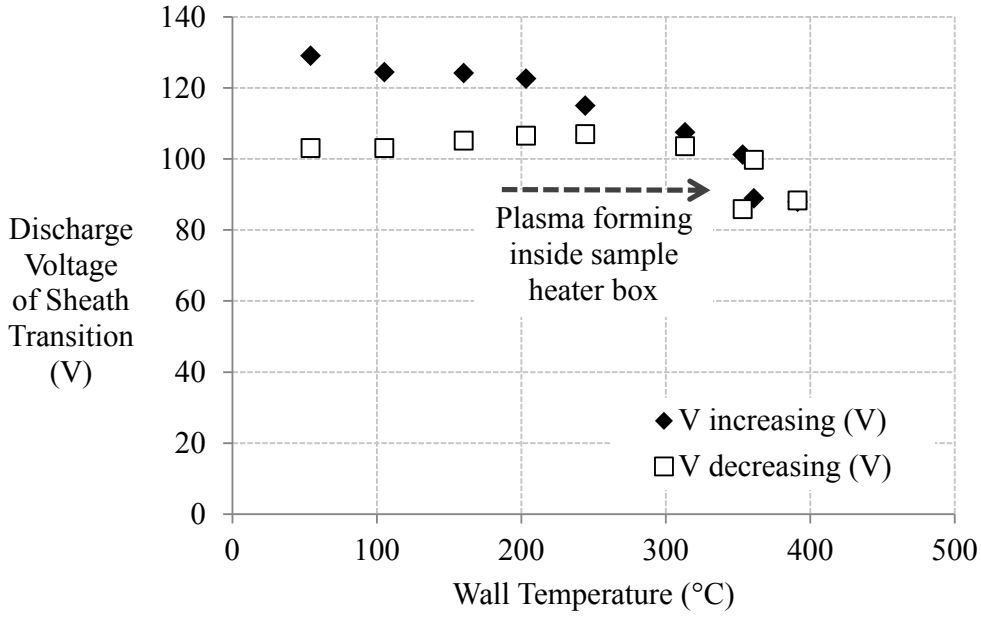

Figure 8.7: Filament bias voltage required for sheath collapse vs. wall temperature. Argon plasma, pressure 1 x 10^{-4} Torr-Ar, discharge current 10 mA. Wall temperature strictly increasing. In increased heating conditions, hysteresis disappears, believed due to the formation of a plasma within the sample heater box.

(an average of 0.94 V/s for the data shown in Figure 8.9), and the floating potential is sampled using a multiplexed ADC channel at 0.5 Hz. The ADC channel impedance is 10 MΩ. Figure 8.10 shows a summary of several sweeps such as the one shown in

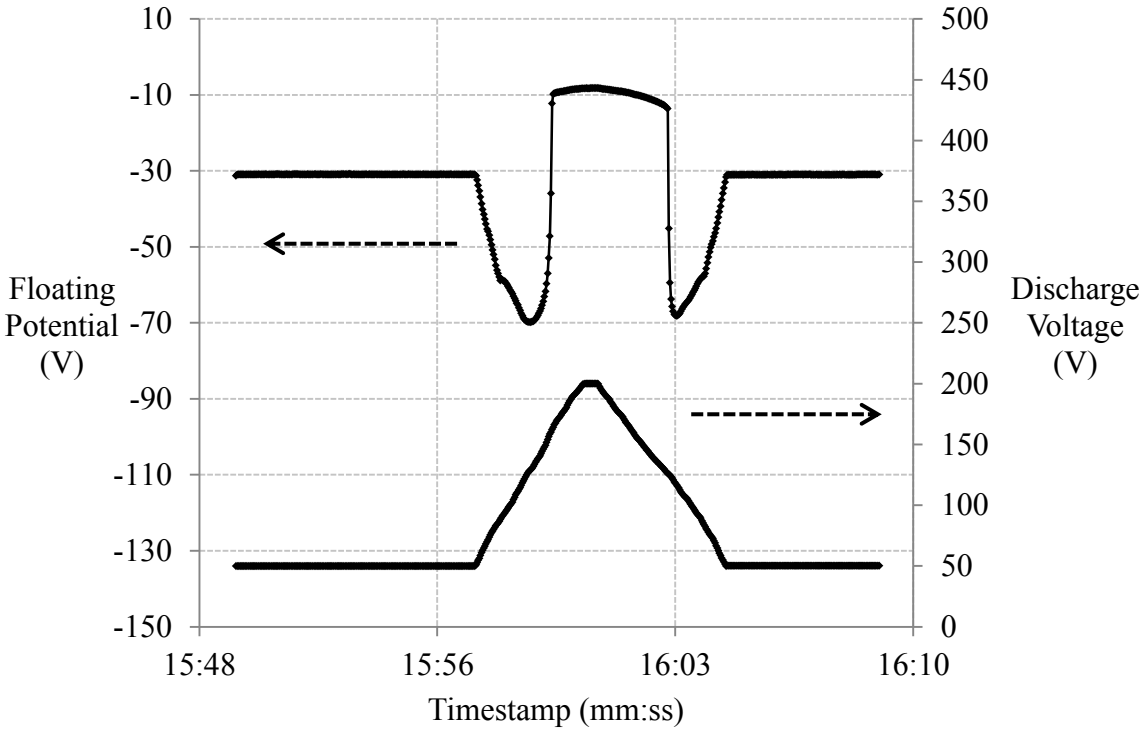

Figure 8.8: Filament bias voltage and floating sheath potential vs. time. Argon plasma, pressure 1 x 10^{-4} Torr-Ar, BN wall temperature 284 °C.

Figure 8.9 taken over a time period of 4 hours, during which the wall temperature was cooled from an initially heated state at ≈ 500 °C to near ambient temperature at 40 °C. The discharge filament bias voltage at which the sheath transition occurs is determined as the data point where the central-difference derivative is the greatest, for both increasing and decreasing filament bias voltages.

8.3 Discussion

An interesting observation from the data of Figures 8.8 - 8.10 is that in all conditions the sheath collapsed at a higher filament voltage when the filament voltage was being increased than when it was being decreased. This hysteresis behavior is similar to

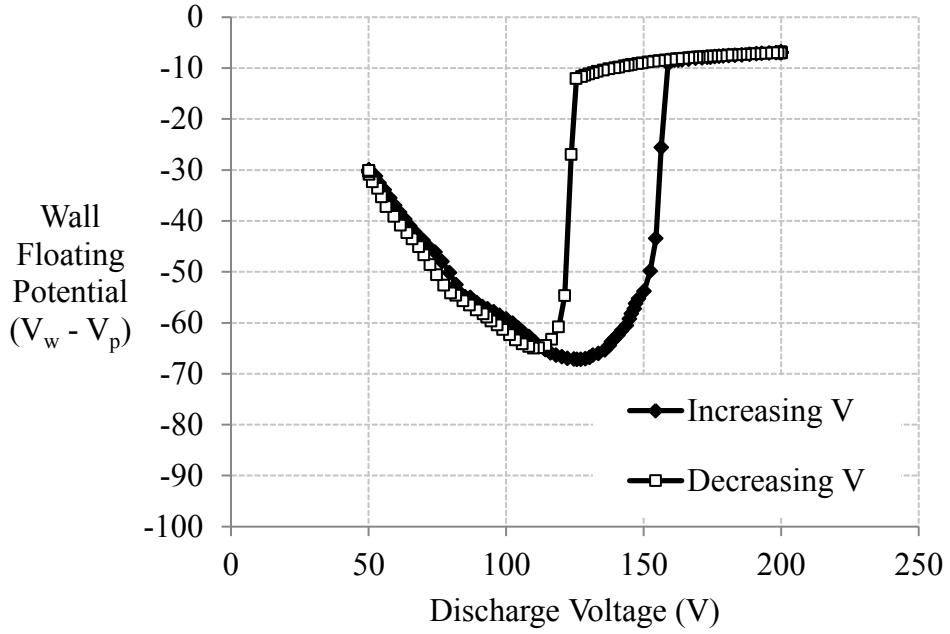

Figure 8.9: Filament bias voltage vs. floating sheath potential (V) of BN sample as measured with witness emissive probe. Argon plasma, pressure 1 x 10^{-4} Torr-Ar, discharge current 10 mA, wall temperature 381 °C.

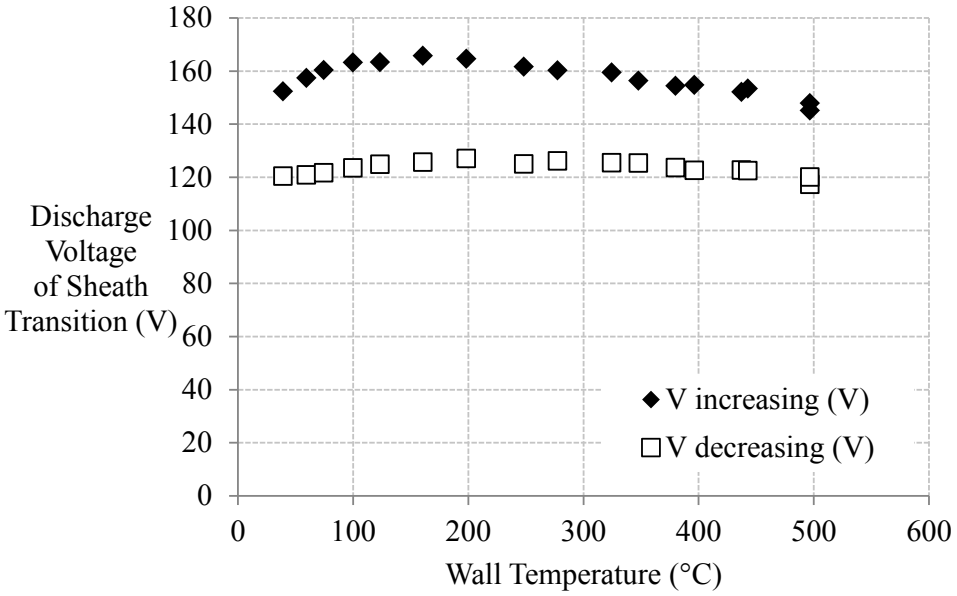

Figure 8.10: Filament bias voltage required for sheath collapse over BN sample vs. wall temperature. Argon plasma, pressure 1 x 10^{-4} Torr-Ar, discharge current 10 mA, wall temperature strictly decreasing. No significant dependence on wall temperature is observed.

the S-curve behavior predicted in the emitting-wall sheath models in Chapter 7 (*c.f.* Figure 7.3) for conditions with prevalent energetic electrons.

This hysteresis occurred at all wall temperatures with the BN wall, but disappeared at elevated temperatures with the LaB_6. It is believed that the disappearance of hysteresis is driven by the formation or leak of plasma into the interior of the sample heater box. In support of this hypothesis, it is first observed that the LaB_6-coated sample begins to have always the same potential as the metal sample heater box, despite being separated by ceramic standoffs. Beyond these insulators, the back of the metal substrate of the LaB_6-coated sample was not insulated from the interior of the heater box, so plasma contacting it would affect the floating potential. The heater box contained hot tantalum filaments which could have assisted in forming a plasma. If a plasma did form in the heater box, it would likely change the total energy distribution encountered by the LaB_6 sample from that assumed in the sheath model and thus could lead to the disappearance of the hysteresis phenomenon. It could also be that connecting to the sample frame changed the overall wall SEE yield relation, which also effects the conditions for hysteresis in the model. A plasma inside the box would not effect the BN sample, which insulates itself from the interior of the heater box by virtue of being a non-conductive material.

Aside from the observed effects of outgassing with surface temperature, we do not find any strong effects on the sheath and plasma-wall interaction that are intrinsically dependent on wall temperature in the temperature regime studied 0-500 °C. This gives increased confidence that at subthermionic temperatures such as are sustainable in thrusters, the resulting effect on the sheath and the plasma-wall interaction will not be significant.

Due to the large sheath thickness, the current testing was performed at a relatively low sheath electric field. A strong sheath electric field resulting from a high-density plasma and thin sheath may be able to elicit field emission from BN. Attempts in

literature to achieve this effect has been shown to require very strong electric fields in the neighborhood of 10^6 - 10^7 V/m even when the crystal structure of the BN is optimized to promote emission (cubic phase rather than hexagonal phase) [29]. Such strong fields would not be achieved in the sheath until plasma densities of order 10^{20} m^{-3} are attained. This may be an area to investigate in the future, if thruster plasma densities are able to be increased to such levels. If field emission does begin to occur, it is expected to have little dependence on temperature up to 1500 K [36].

CHAPTER IX

INFLUENCE OF SURFACE ROUGHNESS AND FEATURES

In high-density plasmas, the sheath thickness length scale will be very small due to the increased plasma density, so even relatively "smooth" walls with only microscale surface features could appear rough and featured to the plasma. These experiments were conducted to investigate the effect of surface features on the sheath when the feature sizes are much less than or on the order of the Debye length. Since the Debye lengths are relatively large (millimeters) in the plasma cell, wall samples with micrometer-scale roughness and millimeter-scale grooves were used.

9.1 Experimental Setup

Sheaths were measured over the rough and smooth BN samples described in Chapter 6. A height map from a scan is shown in Figure 9.1.

The average roughness (computed as the arithmetic mean of the absolute deviations in height from the mean height) is 10.4 µm, averaged across 5 scans at 20x magnification. The standard deviation of the average roughness between the five scans is 2.68 µm.

The macroscopically grooved wall material samples for this series of experiments were prepared by our collaborators at UA. They are 3-inch diameter, 1/4-inch thick discs of material with 5-mm wide grooves milled across the plasma-facing surface. Two grooved BN samples were investigated, one with 1-mm groove depth and one with 5-mm groove depth. They are held in the sample heater/holder from the wall temperature experiments (Chapter 8), with the heater not operated in this experiment. The sample holder setup and probe alignment on a plateau of the sample is shown in

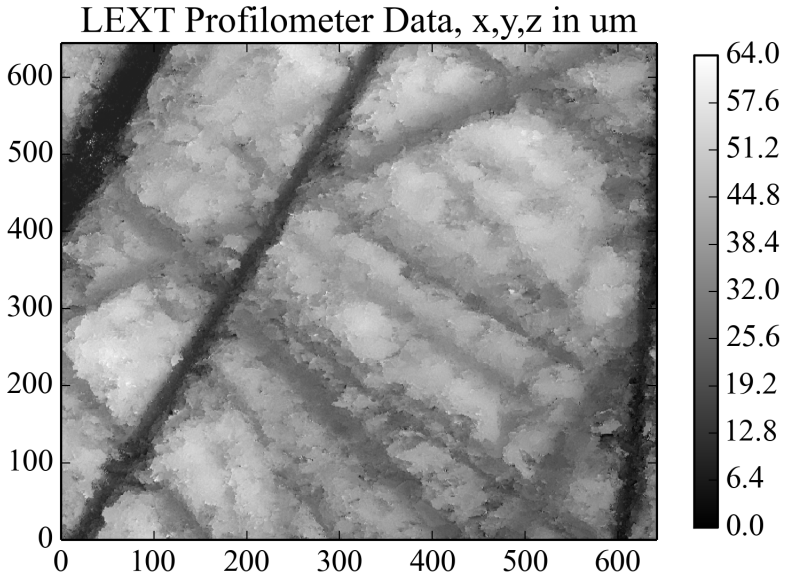

Figure 9.1: Sample height map in micrometers of roughened BN sample measured using LEXT OLS4000.

Figure 9.2.

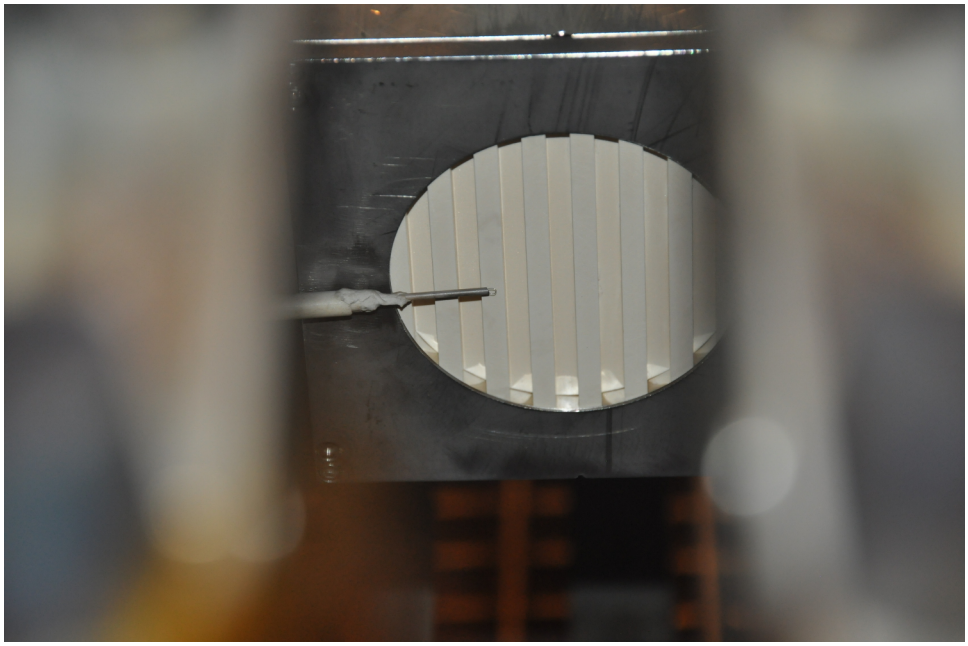

Figure 9.2: Photo of 5mm-depth grooved BN sample installed in plasma cell and alignment of emissive probe tip above surface plateau.

The plasma discharge current was varied between several levels, in order to vary

the plasma density, Debye length, and ultimately the sheath thickness with respect to the fixed groove size. The plasma becomes visible as a faint pink glow at 500 mA discharge current, as shown in Figure 9.3.

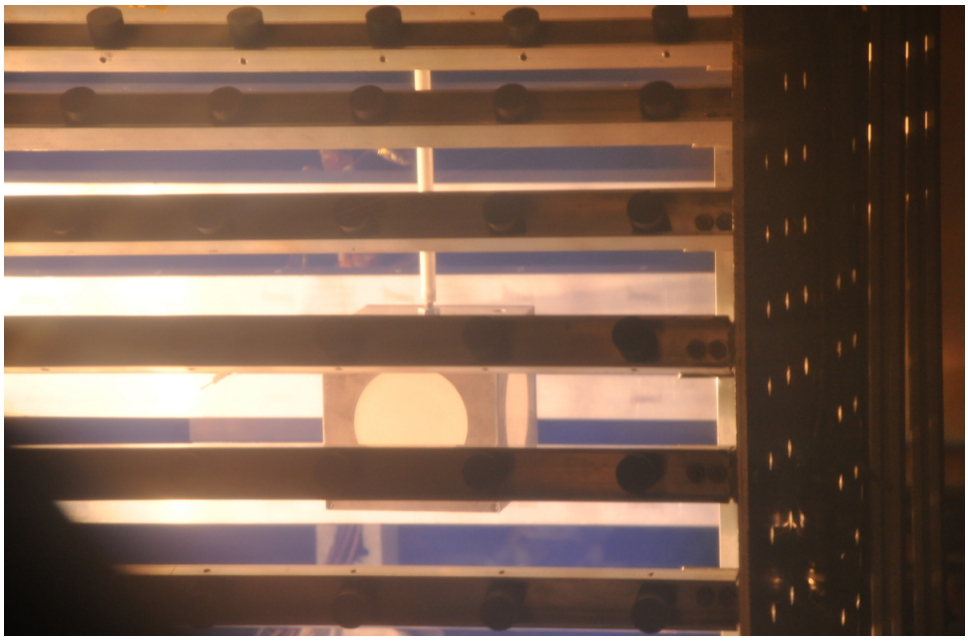

Figure 9.3: Photo of plasma cell testing at 500 mA discharge current with grooved and non-grooved BN samples. Argon plasma, pressure = 1 x 10^{-4} Torr-Ar.

9.2 Results

The sheath measured over the rough and smooth BN samples are shown in Figures 9.4 and 9.5.

The sheaths over the rough and the smooth BN samples are similar within the measurement precision, except that the sheath over the smooth sample transitions to the collapsed equilibrium at a lower filament bias than the sheath over the rough sample. This is believed due to the rough wall's geometrical obstruction and retention of secondary electrons that could otherwise escape, keeping it at a lower yield than the smooth wall for a given plasma condition.

The sheath measurements for these experiments were performed in 2D as well as 1D, to observe possible potential gradients in the plane of the wall surface due to

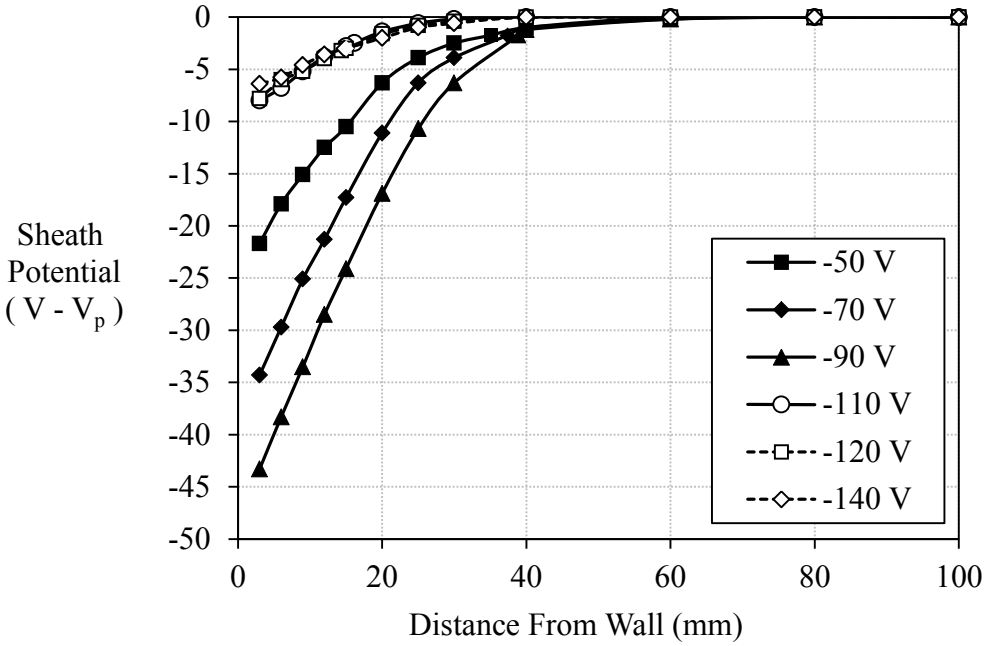

Figure 9.4: Measured sheath potential profiles over smooth BN wall for varied values of the primary electron accelerating voltage. Argon plasma, extrapolated method, pressure = 1 x 10^{-4} Torr-Ar, discharge current 10 mA.

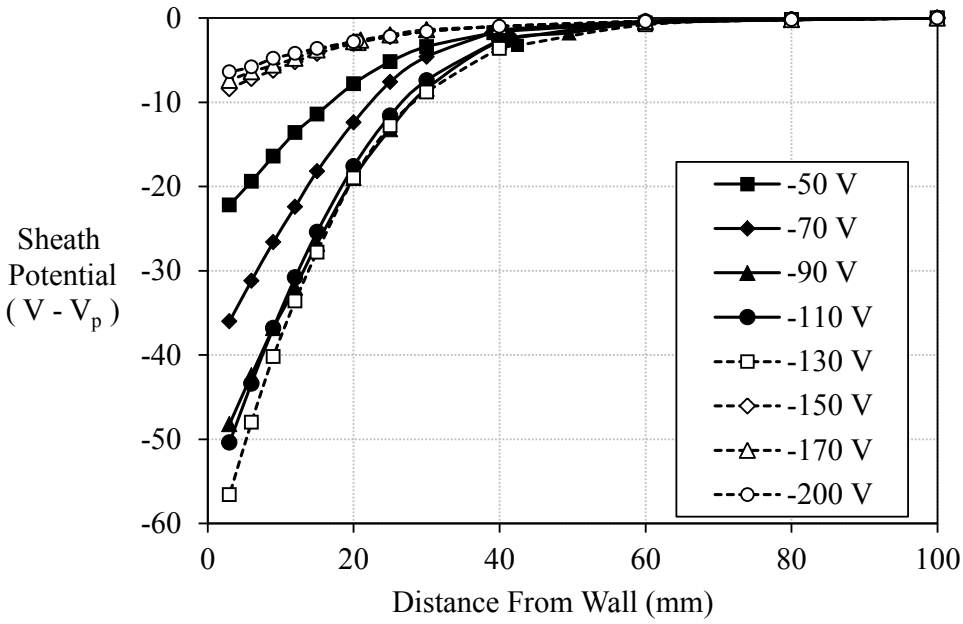

Figure 9.5: Measured sheath potential profiles over rough BN wall for varied values of the primary electron accelerating voltage. Argon plasma, extrapolated method, pressure = 1 x 10^{-4} Torr-Ar, discharge current 10 mA.

the grooved surface features. Due to the substantial increase in the volume of data required to collect, abbreviated measurements were run on the sample with 1-mm deep grooves. It was observed that it was hard to distinguish any results from a flat sample, so 2D measurements on the 1-mm depth sample were halted and effort was focused on the 5-mm deep sample. The results are shown in Figure 9.6 - 9.10.

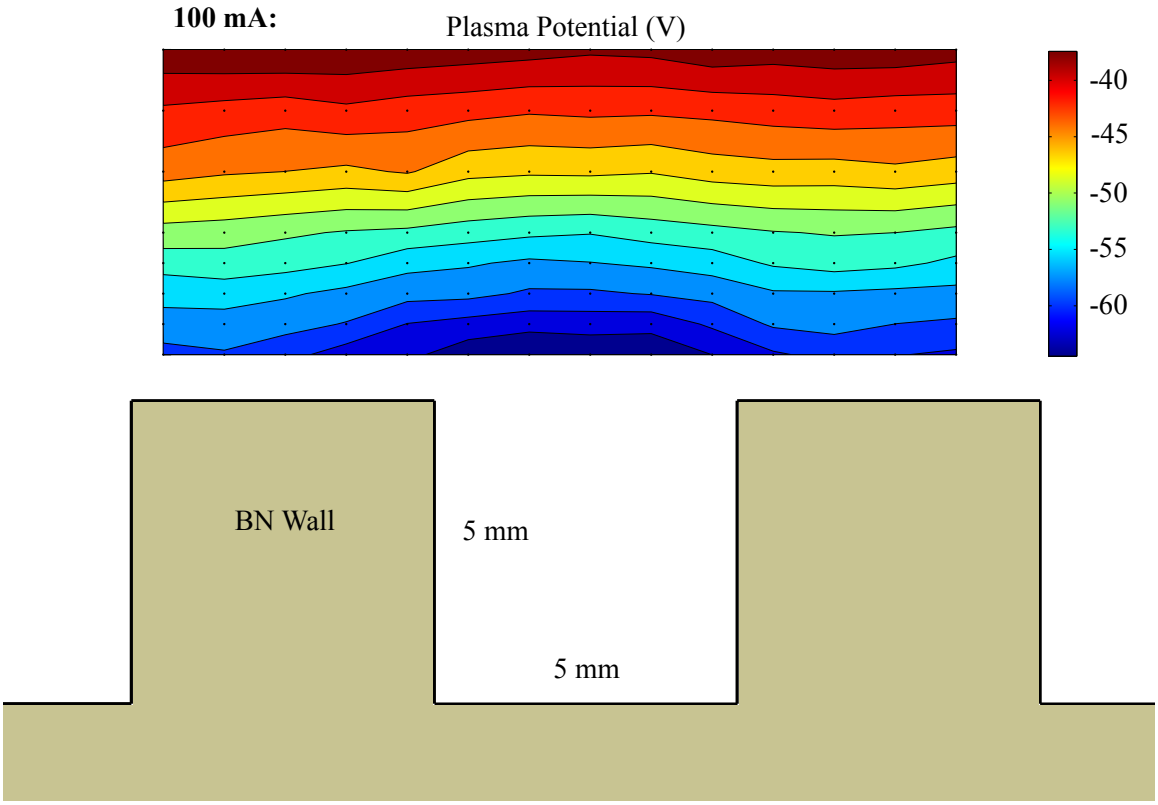

Figure 9.6: Potential measurements in 5x13 mm area near 5-mm-grooved BN wall. Argon plasma, mean method, pressure = 1 x 10^{-4} Torr-Ar, discharge current 100 mA, sheath thickness 12 mm.

The discharge voltage is also varied with the probe positioned 10 mm from the wall to map out the floating voltage of the wall material samples as a function of the primary electron energy, as shown in Figure 9.11.

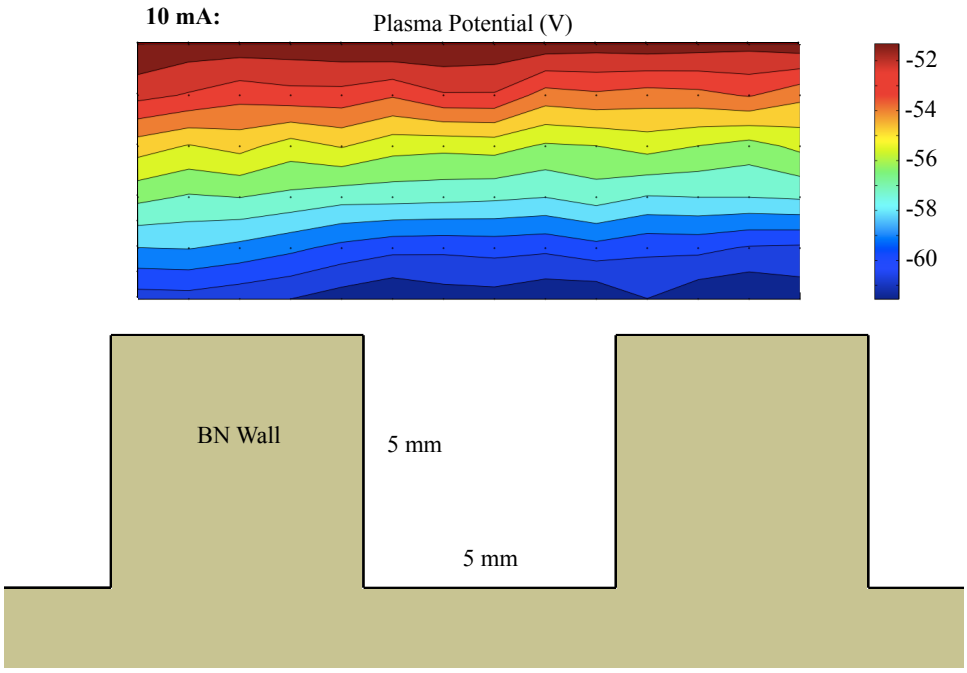

Figure 9.7: Potential measurements in 5x13 mm area near 5-mm-grooved BN wall. Argon plasma, mean method, pressure = 1 x 10^{-4} Torr-Ar, discharge current 10 mA, sheath thickness 35 mm.

9.3 Discussion

During these experiments, the wall material sample was not changed so the physical dimensions of the grooves remained the same. The plasma discharge current was varied between several levels, in order to vary the plasma density, Debye length, and ultimately the sheath thickness. Sheath thicknesses can be seen for the different operating conditions in Figure 9.9.

An intuitive nondimensionalization of the groove dimensions is groove depth over Debye length. If this non-dimensional parameter is combined with the groove aspect ratio and a dimensionless groove spacing, the three dimensionless parameters provide full coverage of the possible parameter space of grooved wall surfaces.

For the 10 mA condition, it can be seen from Figure 9.9 the sheath thickness is about 35 mm, so it is greater than the feature size of 5 mm, so the plasma and sheath

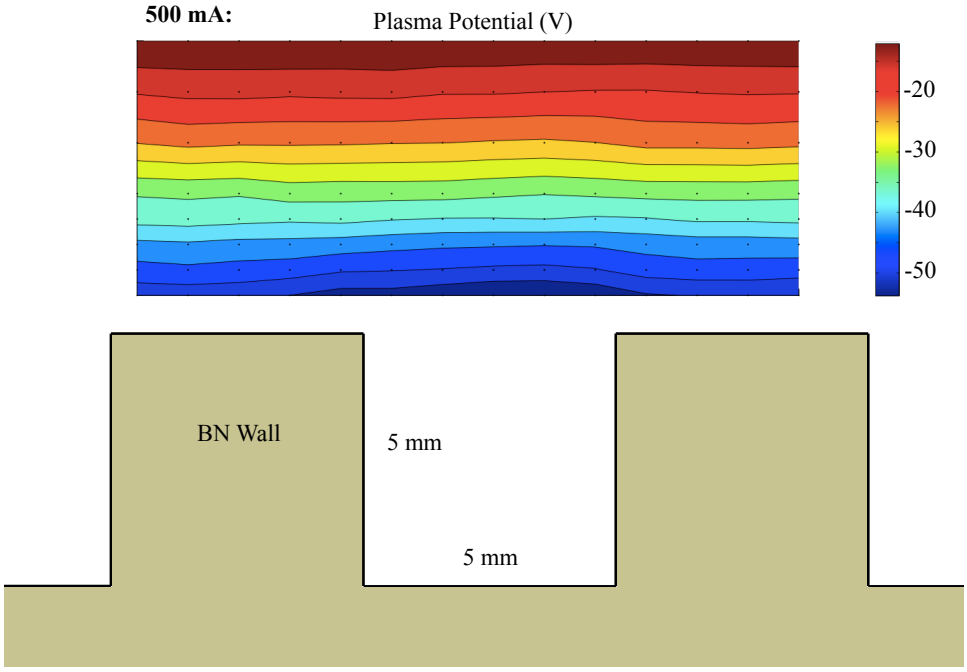

Figure 9.8: Potential measurements in 5x13 mm area near 5-mm-grooved BN wall. Argon plasma, mean method, pressure = 1 x 10^{-4} Torr-Ar, discharge current 500 mA, sheath thickness 8 mm.

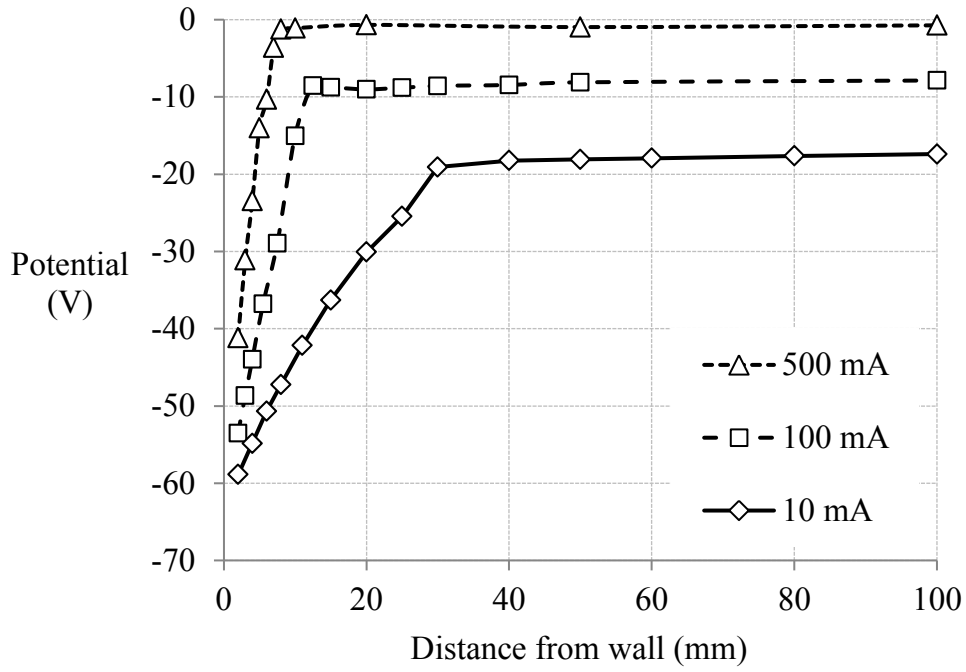

Figure 9.9: One-dimensional sheath potential profiles with 5-mm deep grooved BN sample. Argon plasma, mean method, pressure = 1 x 10^{-4} Torr-Ar, discharge voltage 70 V, varied discharge current.

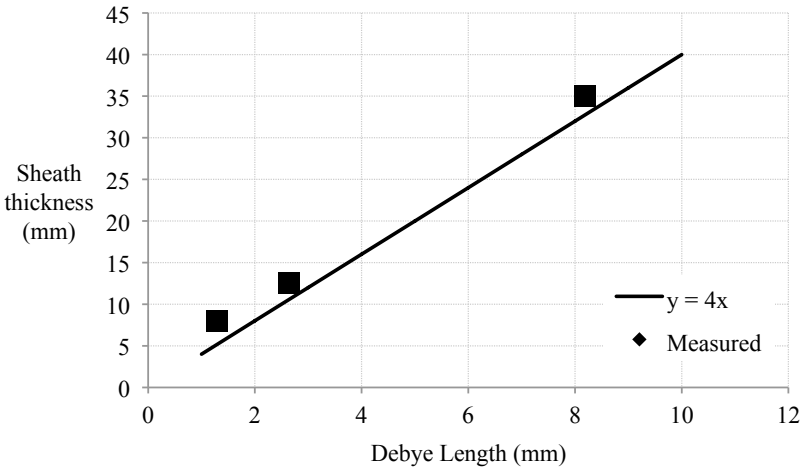

Figure 9.10: Sheath thicknesses of data of Figure 9.9 vs. measured Debye length. Results are close to 4 Debye lengths, which is greater than ≈ 2.7 predicted in theory, possibly due to effects of energetic electrons and/or Langmuir probe uncertainty. Argon plasma, pressure = 1 x 10^{-4} Torr-Ar, discharge voltage 70 V.

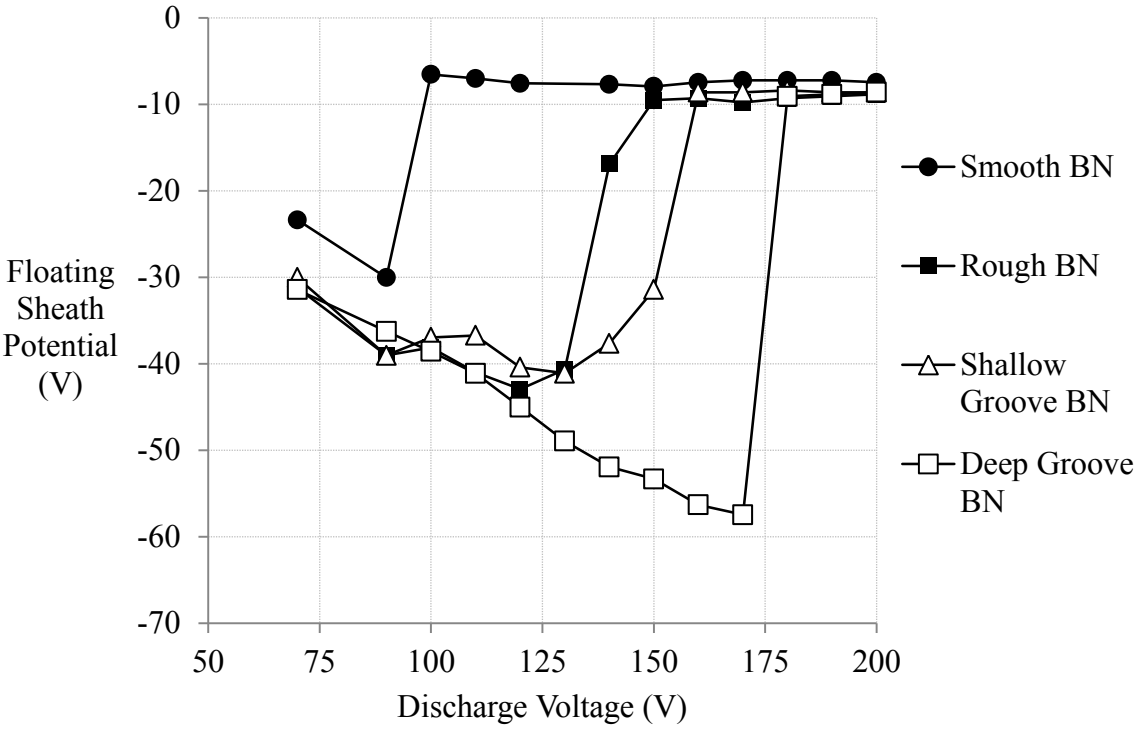

Figure 9.11: Potential 10 mm from wall vs discharge voltage / primary electron energy for smooth, rough, and 1- and 5-mm-deep grooved BN wall material samples. Argon plasma, pressure = 1 x 10^{-4} Torr-Ar, discharge current 10 mA. Debye length varies from 4-8 mm. Roughened and grooved sample topologies postpone sheath collapse to increased energies.

cannot "see" the surface features. The sheath remains largely undisturbed and planar. In this experiment, it was not possible to fit the probe inside the grooves themselves and take data within the grooves, so the sheath behavior therein remains unknown.

At the 100 mA condition, the sheath thickness is about 12 mm, so it closer to the 5 mm length scale of the grooves. The plasma forms an observable curved potential structure near to the wall.

At the 500 mA condition, the sheath thickness is about 8 mm, still closer to the 5 mm length scale of the grooves. The plasma seems to still form a curved potential structure at the groove exit, but due to the increased plasma density the structure is almost below the spatial resolution of the probe.

Figure 9.10 shows the measured sheath thicknesses compared to the measured Debye lengths. The theoretically predicted linear scaling is observed, although the coefficient is higher than the ≈ 2.7 Debye lengths predicted in theory, closer to 4 Debye lengths. This could arise from multiple sources, including uncertainty in determining the sheath edge, uncertainty in determining the plasma parameters and calculating the Debye length, and presence of energetic electrons in the plasma increasing the sheath potential and thickness.

The sheath collapse with increasing discharge voltage / primary electron energy is again observed for all samples, as seen in the results of the investigation of only the smooth BN sample (Chap. 6). The sheath collapse is postponed to yet further energies over the shallow (1 mm depth) and deep (5 mm depth) grooved samples, with the greatest resistance to collapse displayed by the deeply grooved sample.

9.3.1 Electron Trapping

The results shown in Figure 9.11 indicate that some amount of decrease in the effective electron emission from the wall is achieved by grooves at comparable scales o the plasma Debye length. A pertinent question is, how much decrease in effective SEE

yield is achieved, and how much would be achieved by other grooves of differing geometries. A baseline for comparison can be obtained by considering the optical obstruction represented by the groove.

To form a baseline "optical" model of SEE trapping, we will assume the following:

- Uniformly spaced grooves of infinite length
- Particles travel in straight lines (neglect effects of in-groove electric field)
- Particles from the plasma enter the groove diffusely
- Secondary electrons are emitted diffusely from the walls and floor of the groove
- Electron emission is solely a function of particle flux from the plasma, i.e. $\gamma = \text{constant}$
- Emitted electrons whose trajectories terminate on other surfaces within the groove are "trapped" and do not cause additional emissions

This approach contains only geometric information of the grooves, and can be facilitated using standard view factor expressions. We will use the nomenclature of the groove geometry as shown in Figure 9.12. The groove geometry contains three parameters

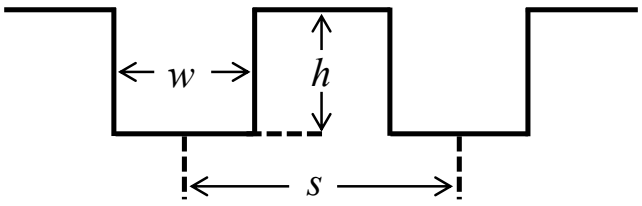

Figure 9.12: Nomenclature for description of grooved walls.

sharing one physical dimension (length), so two non-dimensional parameters are needed to cover the parameter space. We will use the aspect ratio of the groove and the ratio

of groove width to groove centerline spacing, as given in equations (9.1) and (9.2).

$$\mathrm{AR} = \frac{h}{w} \tag{9.1}$$

$$\mathrm{SR} = \frac{w}{s} \tag{9.2}$$

The needed view factor relations are those of an infinite strip adjoining another strip at a 90 degree angle, and two strips separated by a given width. These are respectively:

$$\mathrm{F}_{12} = \sqrt{1 + \mathrm{AR}^2} - \mathrm{AR} \tag{9.3}$$

$$\mathrm{F}_{12} = \frac{1 + \mathrm{AR} - \sqrt{1 + \mathrm{AR}^2}}{2} \tag{9.4}$$

Additional relations accounting for finite length of the surfaces are also available but are longer and not used in this baseline model. When the groove aspect ratio changes, it is necessary to keep track of which source is the origin and which is the target in equation (9.3) – conveniently the same form of the equation can be used, but the aspect ratio is inverted. We denote the surfaces in the groove problem as follows: the entrance plane into the groove is "E" for entrance/exit plane to the groove (where the wall surface would be in a non-grooved wall) "S" for the side walls, and "B" for the bottom of the groove. The overall reduction in gamma from the presence of the groove can be constructed from the view factors of the floor and the two side surfaces towards the entrance/exit plane.

$$\frac{\gamma_{\mathrm{groove}}}{\gamma_0} = \mathrm{F}_{\mathrm{EB}}^2 + 2\mathrm{F}_{\mathrm{ES}}\mathrm{F}_{\mathrm{SE}} \tag{9.5}$$

The first term in 9.5 is the SEE from the bottom of the groove, and the second term is the contribution from the two sides. The term γ_0 denotes the emission yield that would be presented from a non-grooved wall, which has been assumed constant. The emission out of the groove is entirely a function of aspect ratio in this formulation. This factor describes only the reduction in emission from the areas of the wall that are grooved – the effective yield of the wall as a whole will be higher due to the

non-grooved regions emitting at the nominal yield. To determine the effective SEE yield of the whole wall surface, it is necessary to include the groove spacing:

$$\frac{\gamma}{\gamma_0} = \mathrm{SR}\left(\frac{\gamma_{\mathrm{groove}}}{\gamma_0}\right) + (1 - \mathrm{SR}) \tag{9.6}$$

Figure 9.13 shows the range of reductions in SEE yield that can be expected based on equation (9.6). It is seen that at high aspect ratio (deep grooves), very few straight-line paths are available for the electrons to escape the groove and the predicted yield decreases linearly with groove area.

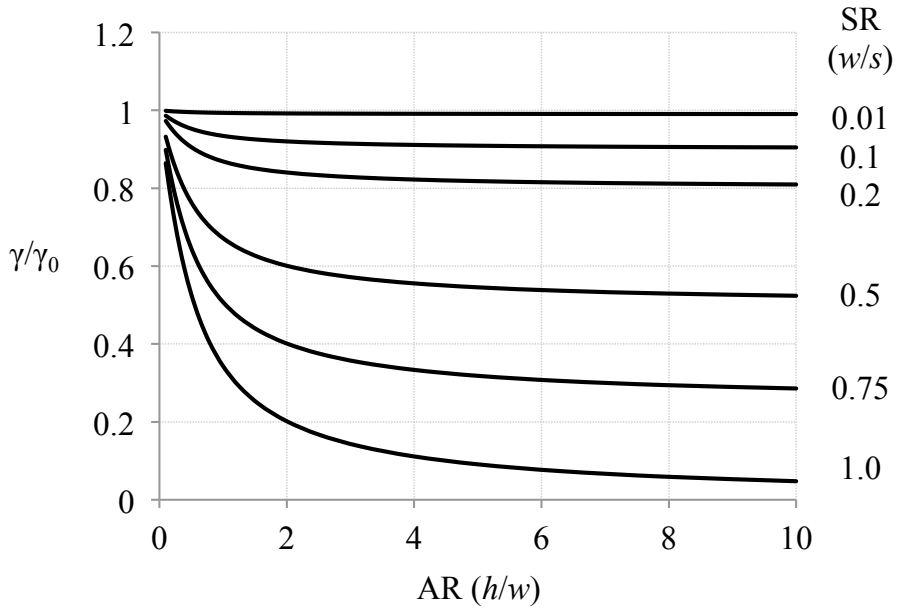

Figure 9.13: Optical model of reduction in SEE yield with grooved walls.

Comparison with Experimental Data

In order to compare the model to the experimental data from 9.11 to the optical trapping model, it is needed to know the effective emission yield that is occurring in the experiments for the known groove geometries. This yield can be estimated using the model of Chapter 7 by applying an arbitrary reduction factor to the wall SEE yield and testing to see which values predict the observed sheath collapse best. The groove geometries are summarized in Table **??**.

Table 9.1: Groove dimensions using nomenclature of Figure 9.12 and equations 9.1 and 9.2, and comparison to plasma Debye length and sheath thickness.

Case	Deep-groove BN	Shallow-groove BN
h (mm)	5.0	1.0
w (mm)	5.0	5.0
s (mm)	10.0	10.0
AR	1	0.2
SR	0.5	0.5
$\frac{\gamma}{\gamma_0}$ model	0.6716	0.8766
λ_D (mm)	8.18	8.18
x_w (mm)	35	35

Figure 9.14 shows the experimental data from 9.11 compared to model with a constant energetic electron fraction $\alpha = 0.025$ and BN SEE yield data suppressed by an arbitrary reduction factor. For the macroscopic groove samples tested in Figure 9.14, the potentials measured are smaller in magnitude the predicted wall potentials, which agrees with intuition as they are measured 10 mm from the wall, midway through the sheath thickness. The groove geometry can be input to the optical trapping model to predict the reduction factor for the electron emission. For the shallow groove sample, AR = 0.2, SR = 0.5, and the predicted $\gamma/\gamma_0 = 0.877$. For the deep groove sample, AR = 1, SR = 0.5, and the predicted $\gamma/\gamma_0 = 0.672$. As shown in the comparison Figure 9.14, the postponement of the sheath collapse in roughly correct for the deep grooves, but the shallow grooves postpone the collapse further than predicted. This could be due to approximate model parameters and/or the significance of microscale roughness on the shallow and deep groove sample, which is observed on the rough sample to have a significant effect over the smooth sample.

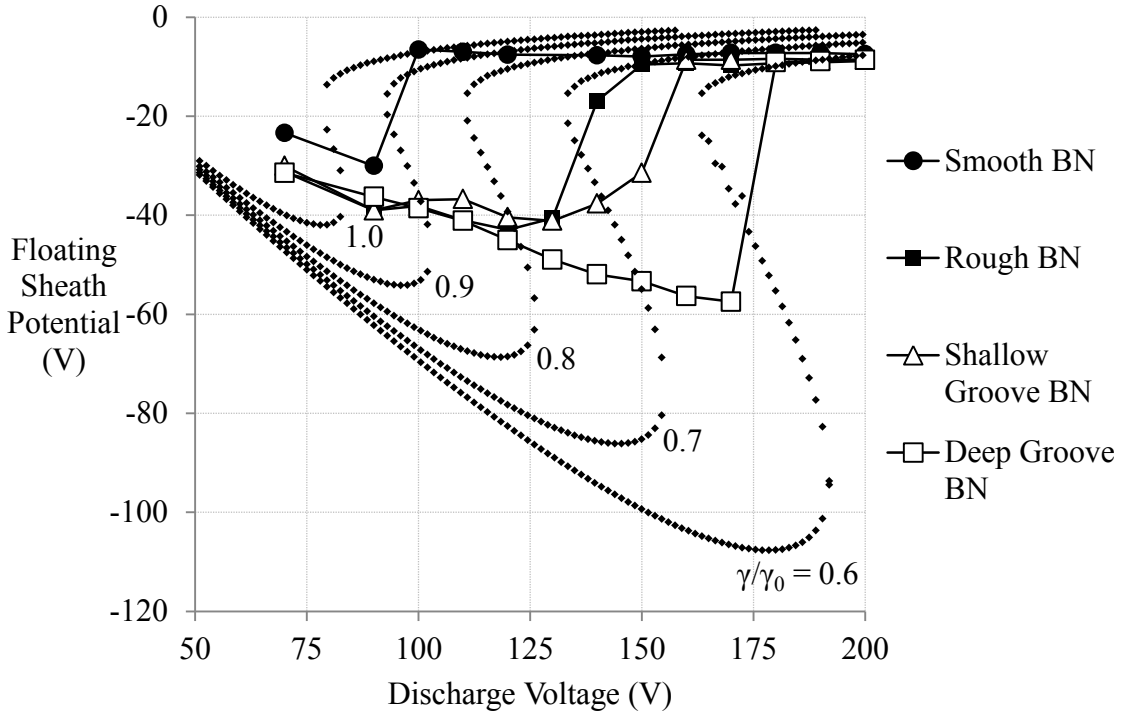

Figure 9.14: Comparison of sheath collapse over grooved samples with optical trapping model from 0 - 40% trapping / kinetic sheath model with BN SEE yield data, argon, $\alpha = 0.025$, $\Theta = 10$, $T_{ep} = 3$. Experimental points measured 10 mm from the wall. Shallow groove sample predicted $\gamma/\gamma_0 = 0.877$. Deep groove sample predicted $\gamma/\gamma_0 = 0.672$.

9.3.2 Comparison to GWU Simulation

The experimental data was provided to GWU. At the time of this writing GWU has completed their first simulations with grooved samples. The results for potential and electron density are shown in Figures 9.15 and 9.16. The results in Figure 9.15 show

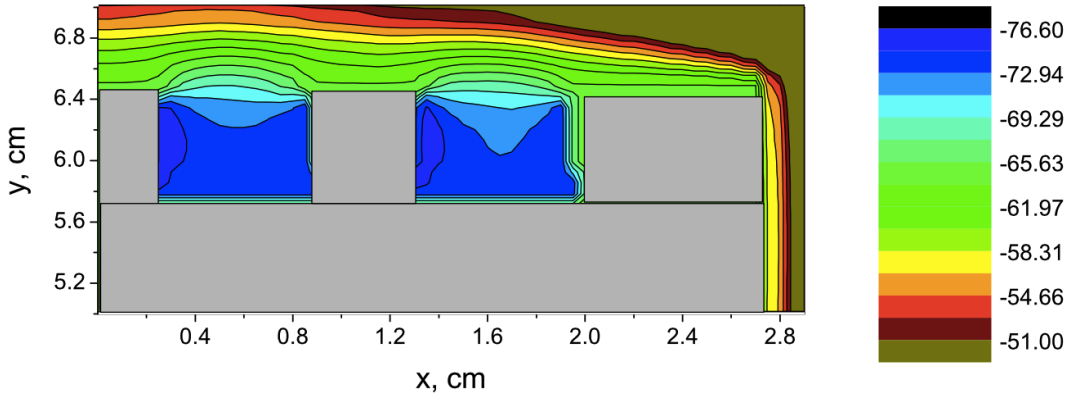

Figure 9.15: GWU preliminary simulation results of potential (V) over grooved wall material sample. Simulated primary electron energy = 70 V in the -y direction.

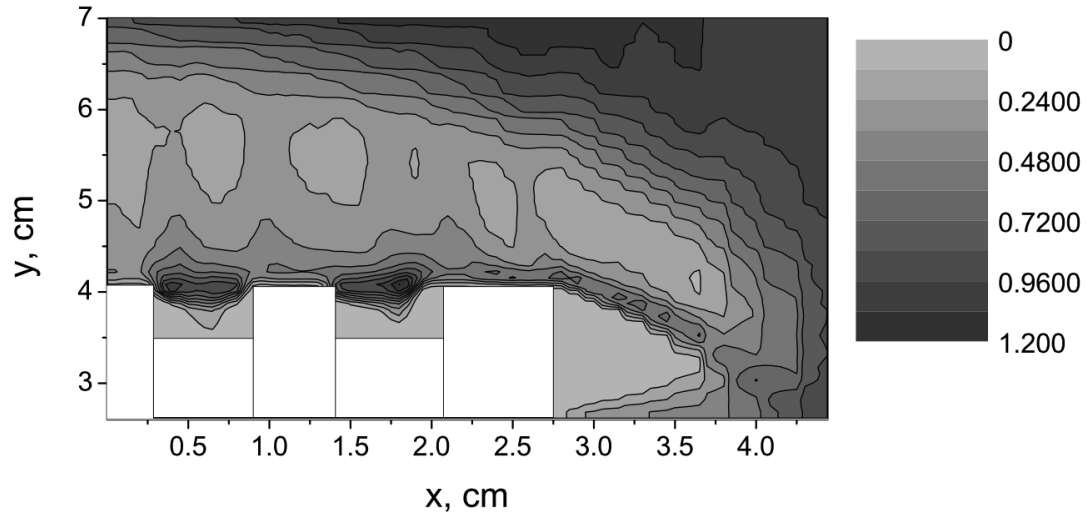

Figure 9.16: GWU preliminary simulation results of electron density (10^8 cm^{-3}) over grooved wall material sample. Simulated primary electron energy = 70 V in the -y direction.

a similar potential structure at the entrance to the grooves as to the experimental measurement (*c.f.* Figure 9.6). The electron density map in Figure 9.16 shows that

the potential structure is caused by an accumulation of electron density near the groove entrance. The electrons appear to be preferentially concentrated at the groove entrance due to electrostatic forces from the nearby floating walls and their overlapping semi-sheaths. The results are preliminary but exciting, and more simulations are planned to investigate if the electron concentration is connected to SEE from the boundary, or to the electron beam present in the plasma source, or if it is intrinsically created by the grooved surface structure. If similar electron concentrations could develop in Debye-scale surface depressions in Hall effect thruster channels, it could focus ions into the depressions and thus contribute to the growth of the anomalous large-scale erosion ridges observed in Hall effect thruster lifetime tests.

CHAPTER X

CONCLUSIONS

The overall goal of this research has been to study thruster-relevant sheath physics in a quiescent large-sheath plasma environment. This has been pursued through direct measurements of sheath potential profiles and study of the effects of electron emission from the wall, wall roughness, and wall temperature. Specific results of the studies as well as promising directions for future work are summarized below.

10.1 Electron emission: Hobbs & Wesson and Beyond

The research in this thesis has yielded detailed measurements of sheaths undergoing the transition from classical Child-Langmuir scaling to a collapsed Hobbs & Wesson structure. In addition to the raw dataset, good agreement has been found with a model that extends the traditional Hobbs & Wesson formulation to a kinetic framework. The model is largely due to Sheehan *et al.*, adapted somewhat in this work to use wall material-SEE yield relations and a different form of electron energy distribution to include the isotropically distributed electrons observed in this plasma device. Promising agreement has also been observed with particle-in-cell simulations of the full experimental plasma device. This research therefore provides increased confidence in modeling of sheaths and plasma-wall interactions up to this level (near unity emission coefficient) of electron emission. This is a valuable regime for thruster development, as most thruster plasma-wall interactions are desired to remain in the non-collapsed sheath region to prevent high electron energy fluxes to the wall, while possibly taking advantage of some electron flux from the wall to modulate plasma temperatures.

An interesting finding of this work pertains to the question of the existence and properties of the "inverse sheath" regime of a strongly emitting electrically isolated

surface, proposed recently by Campanell *et al.* It is seen that as the effective plasma temperature is increased (driven by the enhanced energy of an energetic population), the Hobbs & Wesson-like sheath gradually erodes and comes to resemble more of a flat-line disappearance of the sheath. Measurements of the floating potential of emitting filaments along an alumina wall sample show that with strong emission, they do float to a higher potential on average than the bulk plasma potential. It is likely that the spatially-resolved measurements do not have sufficient spatial resolution to resolve an inverse sheath if one exists. However, the gradual disappearance of the negative-sloping Hobbs-and-Wesson sheath region is notable and gives pause to the idea of simply appending a virtual cathode / inverse sheath layer to the traditional Hobbs-and-Wesson sheath of $\approx 1\ T_e$ and considering the issue settled. The question of the quantitative details of the transition between the collapsed-but-not-inverted H&W sheath and the fully inverse sheath is not fully covered by this research, but this research does show that a range of possibilities exist beyond the space-charge-limited sheath potential of $\approx 1\ T_e$.

Observation of Sheath Oscillations

In the experiment with filaments stretched along the emitting wall material surface, a small but definite peak was observed in the Fourier transform of the wall filament floating voltage. This could correspond to a fluctuating nature of the secondary electron emission process from the wall as predicted in particle-in-cell simulations, as it is observed in a similar frequency range (the measured peak is at 13.3 kHz, GWU observes the oscillation at 25 kHz). Little effect of the discharge voltage / energy of energetic electron population is seen on the frequency of the experimentally observed peak, which remains at 13.3 ± 0.1 kHz.

10.2 Effect of Wall Temperature with BN

This research has also explored the effects of elevated wall temperature on the plasma-wall interaction with BN walls and sheath properties. Although first experiments showed a potential effect of wall temperature, further studies showed no effect directly connected to wall temperature. Some effect occurred over significantly longer timescales, which were determined to be due to degassing of the surface and deposition of sputtered metal on the wall material samples. In particular, over long durations of multiple days in the wall material experiments that as the experiment continues, the sheath collapse becomes postponed until higher energies, as sputtered metal accumulates on the surface which has a lower SEE yield than the ceramics it covers.

This underscores the potential for facility effects in electric propulsion ground testing – if a freshly-machined thruster with a ceramic channel is launched into orbit and operated in space, where there is no facility wall from which to backsputter a metal/graphite coating of the discharge channel, the steady-state sheath potential and power balance of the thruster on orbit may differ significantly from the ground test conditions. Or it may not – because the sheath collapse is a sharp change in the plasma properties, it may make very little difference whether the channel is sputter-coated or not if the thruster is operating in a condition far from the sheath transition point.

10.3 Effect of Surface Topology due to Obstruction of Electron Emission

The present research observes that surface topology is a very relevant effect for plasma wall interactions where electron emission is significant. In all cases of rough and featured walls studied, both below and comparable to the plasma Debye length, a substantial increase in the energy required to elicit enough SEE to collapse the sheath was observed with increasingly featured surfaces. For macroscopic wall features, the reduction in emission observed was found to be similar what would be expected from

straightforward geometric trapping. This informs efforts to develop novel plasma-facing materials using innovative microscale and nanoscale surface geometries. There is also interesting experimental measurement of a curved potential structure forming at the entrance of surface grooves, now replicated in particle-in-cell simulations, which if present in thrusters could focus ions and constitute a mechanism for the development of ridged erosion patterns. Further work is necessary to determine what is causing the potential structure, i.e. if it is a consequence of the energetic electron population or perhaps the wall material emission condition.

10.4 Experimental Validation of Classical Sheath Theories and Sheath Scaling

The measurements in this work have again confirmed the validity of the Child-Langmuir and Bohm sheath scaling for typical low temperature plasma conditions. While there have existed some sheath measurements in literature before showing similar agreement, primarily from the work of Dr. Hershkowitz's group at University of Wisconsin-Madison, it is healthy to have more confirmation from a diversity of experimental facilities and backgrounds. Simultaneously, it is a good validation for the more exploratory research conducted in this work, and lends confidence to the measurement techniques used throughout.

10.5 Recommendations for Future Work

As previously stated, experimental research on sheaths is sparse and there are many areas of interest left to investigate.

10.5.1 Strongly Emitting Sheath

Most directly related to the present research, it remains to determine more precisely the characteristics of the sheath transition between non-emitting and strongly-emitting sheath regimes, particularly the region in which the transition to the inverse sheath

regime occurs. This will require effort on both the theoretical / modeling side to determine the correct physics, and the experimental side to test the models. Specifically, the author believes there is need for a physical model that correctly bridges the gap between enforcing the Bohm criterion in the non-emitting case and not enforcing it in the strongly-emitting inverse sheath case.

10.5.2 High Electric Field

One drawback of the low-density sheath approach pursued in this work is that the electric fields at the material surface were intrinsically quite low, on the order of 1000 V/m. At increased plasma densities, the increased sheath electric field may begin to promote electron emission from the wall through the Schottky effect or even through field emission, particularly if the wall nanostructure is shaped to concentrate the field. Further experiments at high plasma densities and correspondingly high electric fields would be interesting to investigate this possibility, although measurement of the full sheath profile would become very challenging and it would probably be best to just try to track the wall potential and plasma potential.

10.5.3 Magnetic Field Effect on Sheaths

Another avenue of investigation that recommends itself is the interaction of sheaths and magnetic field. Since the application of magnetic fields is one of the primary methods of improving the efficiency of thrusters and plasma discharges in general, the determination of the impact of magnetic fields on sheaths has great practical value for the design and optimization of devices. As discussed in the literature review section, experimental measurements and even models are sparse in this subset of plasma-wall interactions. Using probes as the primary diagnostic may be non-trivial, as probe measurements in magnetized plasmas are subject to additional complications. The avenue of investigation may go hand-in-hand with the investigation of anomalous electron mobility across magnetic fields in plasmas, the quantitative calculation of

which is one of the unsolved physics problems in the development of Hall effect thrusters.

10.5.4 Origin of Erosion Ridges

Hall effect thrusters have been observed to develop a ridged erosion pattern in long duration (≈10,000 hours firing) qualification tests. While the origin of the grooves is currently unknown, this research suggests that there may exist a sheath mechanism for the growth of trenches in situations under long-duration ion bombardment. The potential focusing structure observed in Figure 9.6 could act to preferentially focus ions into existing grooves / trenches, thereby deepening them over time and increasing the effect. In future experiments it would be interesting to investigate the potential structure inside the groove. This area could not be interrogated in the current experiments (the emissive probe was oriented parallel to the surface plane, and did not include a dogleg or 90° bend to allow the probe tip to get inside the groove.) If the space charge sparsity of electrons continues within the groove, an electric field may continue to exist inside the groove, boosting the energy of ion impacting the wall and increasing the erosion rate.

APPENDIX A

DERIVATIONS

A.1 Electrostatic Poisson Equation

The electrostatic Poisson Equation needed to calculate sheath potential profiles proceeds from Gauss's Law and the Maxwell-Faraday equation of classical electromagnetics.

$$\nabla \cdot \vec{E} = \frac{\rho}{\epsilon_0} \tag{A.1}$$

$$\nabla \times \vec{E} = -\frac{\partial \vec{B}}{\partial t}, \tag{A.2}$$

The only further assumption needed to reach the electrostatic Poisson equation is an absence of time-varying magnetic field. This gives that the electric field is irrotational,

$$\nabla \times \vec{E} = \vec{0}, \tag{A.3}$$

and thus it can be written as the gradient of a scalar potential. By famously non-intuitive convention, a negative sign is included.

$$\vec{E} = -\nabla\phi \tag{A.4}$$

Substituting into Gauss' Law gives the electrostatic Poisson equation.

$$\nabla^2\phi = -\frac{\rho}{\epsilon_0} \tag{A.5}$$

The overall charge density can be expressed as the sum of the charge densities of each plasma species α

$$\nabla^2\phi = -\frac{1}{\epsilon_0}\sum^{\alpha}\left(q_\alpha n_\alpha\right). \tag{A.6}$$

A.2 Boltzmann Relation

The Boltzmann relation is a commonly-used equation for describing plasmas that gives a relation between electron density n_e and the plasma potential ϕ. It shows that gradients in number density and potential are coupled in plasmas.

Assumptions:

- Plasma electrons are treated as classical (non-relativistic) particles
- Plasma electrons have a Maxwellian energy distribution described by T_e

The energy distribution is:

$$f(E) = 2\sqrt{\frac{E}{\pi}}\left(\frac{1}{k_B T_e}\right)^{\frac{3}{2}} \exp\left(\frac{-E}{k_B T_e}\right) \tag{A.7}$$

The presence of electric fields and the charged nature of the electron allows the presence of potential energy in the system. Incorporating that into the energy distribution, it is:

$$f(E) = 2\sqrt{\frac{E}{\pi}}\left(\frac{1}{k_B T_e}\right)^{\frac{3}{2}} \exp\left(\frac{-E + e\phi}{k_B T_e}\right) \tag{A.8}$$

The local electron density n_e is obtained by integrating over all energies 0 to ∞. Since the temperature is uniform, the only dependence is with ϕ:

$$n_e = n_0 \exp\left(\frac{e\phi}{k_B T_e}\right) \tag{A.9}$$

where n_0 is the number density at a reference position and ϕ is the potential with respect to the potential at that reference position. This equation is the usual form of the Boltzmann relation.

In the context of the typical plasma sheath, the Boltzmann relation can be used to see to first order the fraction of plasma electrons that make it through the retarding sheath potential. If a given sheath potential $\phi_w = -5T_e$, the number density of electrons at the wall is

$$n_{e,w} = n_e \exp(-5) \approx 0.0067\ n_e \tag{A.10}$$

so it is seen that this sheath screens out approximately 99% of the bulk plasma electron density.

A.3 Plasma Frequency

The plasma frequency is a fundamental plasma parameter describing how rapidly the charged particle populations in the plasma are able to respond to a perturbation. Typically the term is short for "electron plasma frequency" as the electrons are usually the lightest and most mobile species in the plasma and have the fastest response / highest frequency. It can be derived from Gauss' Law and the fluid description of plasma dynamics, specifically the electron momentum equation and continuity equation.

$$\nabla \cdot \vec{E} = \frac{\rho}{\epsilon_0} = \frac{e}{\epsilon_0}\left(n_\mathrm{i} - n_\mathrm{e}\right) \tag{A.11}$$

$$\vec{F_\mathrm{L}} = e\vec{E} = m\frac{\mathrm{d}\vec{u_\mathrm{e}}}{\mathrm{d}t} \tag{A.12}$$

$$\dot{n_\mathrm{e}} = \nabla \cdot n_\mathrm{e}\vec{u_\mathrm{e}} \tag{A.13}$$

If you consider a perturbation to the electron number density, Gauss' Law is

$$\nabla \cdot \vec{E} = \frac{e}{\epsilon_0}\left(n_{\mathrm{i}0} - \left(n_{\mathrm{e}0} + \mathrm{d}n_\mathrm{e}\right)\right) \tag{A.14}$$

$$\nabla \cdot \vec{E} = \frac{e}{\epsilon_0}\left(\mathrm{d}n_\mathrm{e}\right). \tag{A.15}$$

The perturbation applied to continuity is

$$\mathrm{d}\dot{n_\mathrm{e}} = \nabla \cdot \left(n_{\mathrm{e}0} + \mathrm{d}n_\mathrm{e}\right)\vec{u_\mathrm{e}} \tag{A.16}$$

$$\mathrm{d}\dot{n_\mathrm{e}} = \nabla \cdot n_{\mathrm{e}0}\vec{u_\mathrm{e}} \tag{A.17}$$

$$\mathrm{d}\dot{n_\mathrm{e}} = n_{\mathrm{e}0}\nabla \cdot \vec{u_\mathrm{e}} \tag{A.18}$$

If you take the time derivative and substitute A.15 and A.12, you can reveal that it is a harmonic oscillator equation:

$$\mathrm{d}\ddot{n_\mathrm{e}} = n_{\mathrm{e}0}\nabla \cdot \frac{\mathrm{d}\vec{u_\mathrm{e}}}{\mathrm{d}t} \tag{A.19}$$

$$\mathrm{d}\ddot{n_\mathrm{e}} + n_{\mathrm{e}0}\nabla \cdot \left(\frac{e\vec{E}}{m_\mathrm{e}}\right) = 0 \tag{A.20}$$

$$\mathrm{d}\ddot{n}_\mathrm{e} + \frac{n_{\mathrm{e}0}e}{m_\mathrm{e}}\nabla\cdot\vec{E} = 0 \tag{A.21}$$

$$\mathrm{d}\ddot{n}_\mathrm{e} + \frac{n_{\mathrm{e}0}e^2}{m_\mathrm{e}\epsilon_0}(\mathrm{d}n_\mathrm{e}) = 0. \tag{A.22}$$

The natural frequency of the oscillator is

$$\omega_\mathrm{pe} = \sqrt{\frac{n_{\mathrm{e}0}e^2}{m_\mathrm{e}\epsilon_0}} \tag{A.23}$$

which is the electron plasma frequency.

A common physical description for the plasma frequency is if you were to have a planar slab of ion-electron plasma and you were to instantaneously displace all the electrons by a small distance out-of-plane, they would oscillate normal to the plane against the assumed stationary ion background at the plasma frequency. The plasma frequency depends on only macroscopic quantities, so it can be seen that it is a pure collective behavior effect.

A.4 Debye Length

The Debye length is the length scale that describes the characteristic distance over which Debye shielding occurs in plasmas. Derivations in literature for the Debye length often neglect species other than a Maxwellian population of plasma electrons because the plasma electrons typically end up dominating, but in general the Debye length is a function of all the charged species in the plasma.

To derive the Debye length, we want to see how a plasma of free charged particles acts to shield out the charge of a given test charge. We will thus need the electrostatic Poisson equation (c.f. Appendix A.1).

$$\nabla^2\phi = -\frac{1}{\epsilon_0}\sum^{\alpha}(n_\alpha q_\alpha) \tag{A.24}$$

It is seen in Appendix A.2 that Maxwellian charged particles in a plasma will arrange themselves exponentially in response to a potential gradient (Appendix A.2 was tailored to electrons but in principle can be applied to any plasma species.) We can write the Boltzmann relation as

$$n_\alpha = n_{\alpha 0}\exp\left(-\frac{e\phi}{k_\mathrm{B}T_\alpha}\right) \tag{A.25}$$

where α denotes a particular plasma species i.e. electrons, ions, etc. Plugging the Boltzmann relation into the Poisson equation, it becomes

$$\nabla^2\phi = -\frac{1}{\epsilon_0}\sum^{\alpha}\left(n_{\alpha 0}q_\alpha\exp\left(-\frac{e\phi}{k_\mathrm{B}T_\alpha}\right)\right). \tag{A.26}$$

If we replace the exponential with two terms of a series expansion about $\phi = 0$ (corresponding to the plasma potential infinitely far removed from the test charge) we get

$$\nabla^2\phi = -\frac{1}{\epsilon_0}\sum^{\alpha}\left(n_{\alpha 0}q_\alpha\left(1-\frac{e\phi}{k_\mathrm{B}T_\alpha}\right)\right). \tag{A.27}$$

The first term inside the summation is zero, by quasineutrality of the far-field plasma. Thus we are left with

$$\nabla^2\phi = \sum^{\alpha}\left(\frac{n_{\alpha 0}q_\alpha^2}{\epsilon_0 k_\mathrm{B}T_\alpha}\right)\phi. \tag{A.28}$$

The term multiplying ϕ on the right-hand-side has dimensions of 1/length^2. So we can presciently define a length λ_{D} such that

$$\lambda_{\mathrm{D}} = \sqrt{\sum^{\alpha} \left(\frac{\epsilon_0 k_{\mathrm{B}} T_{\alpha}}{n_{\alpha 0} q_{\alpha}^2} \right)}, \tag{A.29}$$

allowing us to write the Poisson equation as

$$\nabla^2 \phi = \frac{1}{{\lambda_{\mathrm{D}}}^2} \phi. \tag{A.30}$$

A general solution of the differential equation can be found if boundary conditions are applied. Considering cylindrical coordinates and applying boundary conditions

$$\phi(r \to \infty) = 0, \tag{A.31}$$

$$\phi(r \to 0) = \frac{q_{\alpha}}{4\pi\epsilon_0 r}, \tag{A.32}$$

the solution becomes

$$\phi(r) = \frac{q_{\alpha}}{4\pi\epsilon_0 r} \exp\left(-\frac{r}{\lambda_{\mathrm{D}}} \right). \tag{A.33}$$

It is seen that the presence of the plasma introduces an exponential factor shielding the potential of the test charge beyond the Coulomb $1/r$ decay. The exponential factor is mediated by λ_{D}, so it is recognized that λ_{D} is the Debye length and it is controlling the size of the sheath that shields out the potential of the test charge.

Equation A.29 is the general form of the Debye length in a multispecies (Maxwellian) plasma. Because plasma electrons are often substantially hotter than plasma ions, there is often very little change if only the plasma electrons are considered, the so-called electron Debye length.

$$\lambda_{\mathrm{d}} = \sqrt{\frac{\epsilon_0 k_{\mathrm{B}} T_{\mathrm{e}}}{n_{\mathrm{e}} e^2}} \tag{A.34}$$

A.5 Child-Langmuir Sheath

The Child-Langmuir Law was originally developed to describe the flow of charge in vacuum diodes, but can be also applied to describe plasma sheaths. Many sources describe the physics with respect to vacuum diodes but few explain the application to plasma sheaths, so this appendix is intended to clarify the sheath application. Figure A.1 illustrates the situation. When the description is applied to plasma sheaths,

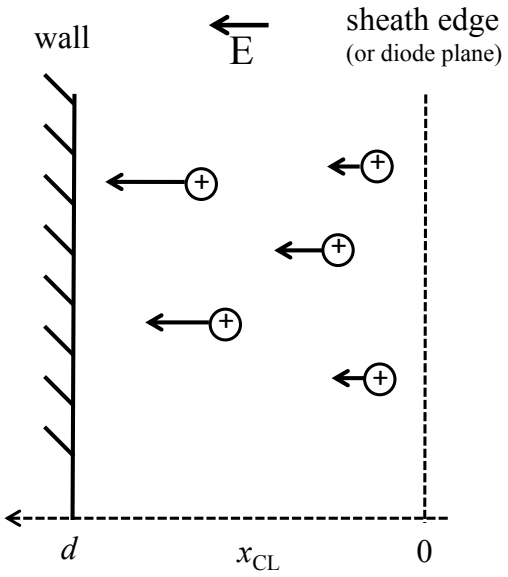

Figure A.1: Spatial locations of reference for the Child-Langmuir problem.

the surface at $x_{\mathrm{CL}} = 0$ is the "sheath edge" and the ions enter the domain from the bulk plasma. Assumptions of the model are:

- Ions are treated as classical (non-relativistic) particles
- Ions are singly-charged, $Z_{\mathrm{i}} = 1$
- Ions are emitted from an infinite planar surface and travel to another planar surface – fully 1D problem
- Ions have zero energy at the starting plane and accumulate energy from the electrical potential difference between planes

- The electric field vanishes at $x_{\mathrm{CL}} = 0$; $\frac{\mathrm{d}\phi}{\mathrm{d}x_{\mathrm{CL}}} = 0$

The last assumption corresponds to the "space-charge-limited" condition, which means that the maximum amount of charged particles are flowing, such that their mutual repulsion has built up to the level at which it cancels out the applied electric field at the starting point. This is the important physics of the Child-Langmuir law, and is why the law often shows up in situations where there is a flow of a single polarity of charge.

The one-dimensional flow of current is conserved at all spatial locations, and it is

$$J = eZ_{\mathrm{i}}n_{\mathrm{i}}u_{\mathrm{i}} = en_{\mathrm{i}}u_{\mathrm{i}} \tag{A.35}$$

as all ions are assumed to carry a single charge. The velocity of an ion as it is accelerated in the electric field can be related to the local potential as

$$u_{\mathrm{i}} = \sqrt{-\frac{2e\phi}{m_{\mathrm{i}}}}. \tag{A.36}$$

The electrostatic Poisson equation is

$$\nabla^2\phi = \frac{\mathrm{d}^2\phi}{\mathrm{d}x_{\mathrm{CL}}^2} = -\frac{e}{\epsilon_0}n_{\mathrm{i}}. \tag{A.37}$$

Substituting A.35 and A.36 into A.37,

$$\frac{\mathrm{d}^2\phi}{\mathrm{d}x_{\mathrm{CL}}^2} = -\frac{e}{\epsilon_0}\frac{J}{eu_{\mathrm{i}}} = -\frac{J}{\epsilon_0}\sqrt{-\frac{m_{\mathrm{i}}}{2e\phi}}. \tag{A.38}$$

A trick to integrate equation A.38 is to multiply both sides by $\frac{\mathrm{d}\phi}{\mathrm{d}x_{\mathrm{CL}}}$, making the integral of the left hand side equal to $\frac{1}{2}(\frac{\mathrm{d}\phi}{\mathrm{d}x_{\mathrm{CL}}})^2$.

$$\int \frac{\mathrm{d}\phi}{\mathrm{d}x_{\mathrm{CL}}}\frac{\mathrm{d}^2\phi}{\mathrm{d}x_{\mathrm{CL}}^2}\,\mathrm{d}x_{\mathrm{CL}} = \int -\frac{J}{\epsilon_0}\sqrt{-\frac{m_{\mathrm{i}}}{2e\phi}}\,\mathrm{d}\phi. \tag{A.39}$$

$$\frac{1}{2}\left(\frac{\mathrm{d}\phi}{\mathrm{d}x_{\mathrm{CL}}}\right)^2 = \frac{2J}{\epsilon_0}\sqrt{-\frac{m_{\mathrm{i}}\phi}{2e}}. \tag{A.40}$$

There is a constant of integration dealt with in the integration from A.39 to A.40, it is proportional to the derivative of ϕ at $x_{\mathrm{CL}} = 0$ which we have assumed to be zero.

Continuing,

$$\frac{\mathrm{d}\phi}{\mathrm{d}x_{\mathrm{CL}}} = \sqrt{\frac{4J}{\epsilon_0}\sqrt{-\frac{m_{\mathrm{i}}\phi}{2e}}}. \tag{A.41}$$

Integrating with separation of variables,

$$-\int \phi^{-\frac{1}{4}} d\phi = \int \sqrt{\frac{4J}{\epsilon_0}} \left(\frac{m_{\mathrm{i}}}{2e}\right)^{\frac{1}{4}} \mathrm{d}x_{\mathrm{CL}} \tag{A.42}$$

$$-\frac{4}{3}\phi^{\frac{3}{4}} = \sqrt{\frac{4J}{\epsilon_0}} \left(\frac{m_{\mathrm{i}}}{2e}\right)^{\frac{1}{4}} x_{\mathrm{CL}} \tag{A.43}$$

$$\phi(x_{\mathrm{CL}}) = -\left(\frac{81J^2 m_{\mathrm{i}}}{32{\epsilon_0}^2 e}\right)^{\frac{1}{3}} {x_{\mathrm{CL}}}^{\frac{4}{3}}. \tag{A.44}$$

The constant of integration can be dropped if the potential is defined such that $\phi = 0$ at $x_{\mathrm{CL}} = 0$. Equation A.44 is one form of the Child-Langmuir law. The Child-Langmuir law gives a relationship between three quantities: potential ϕ, distance x_{CL}, and current density J. If you know two of the three, you can calculate the remaining one, if you know one of the three, you can get and equation between the remaining two. The original and most familiar form of the Child-Langmuir law is the expression solved for the current density J, which is

$$J = \epsilon_0 \frac{4}{9}\sqrt{\frac{2e}{m}} \frac{\phi^{\frac{3}{2}}}{{x_{\mathrm{CL}}}^2} \tag{A.45}$$

This form of the equation allows you to calculate the current density in a vacuum diode of given spacing and voltage. It is also useful in electric propulsion for calculating the current density extracted from an ion engine for a given accelerator grid spacing and voltage. Because the current scales with x^{-2}, outweighing the scaling with potential of $\phi^{\frac{3}{2}}$, closely spaced grids allow more extracted beam current for a given electric field. Therefore it is generally desirable to position the grids as close together as is possible without causing electrical breakdown / arcing between the grids.

Returning to the sheath application, we need an expression for the ion current if we are to get a relation between potential and distance. We can use results from

presheath analysis to say that ions flow into the sheath at the Bohm velocity, and thus carry a current of

$$J = \alpha_{\mathrm{ps}} n_{\mathrm{p}} e u_{\mathrm{B}} = \alpha_{\mathrm{ps}} n_{\mathrm{p}} e \sqrt{\frac{eT_{\mathrm{e}}}{m_{\mathrm{i}}}} \tag{A.46}$$

where n_{p} is the bulk plasma density and α_{ps} is a factor less than unity describing the decrease in density across the presheath, such that $\alpha_{\mathrm{ps}} n_{\mathrm{p}}$ is the density at the sheath edge. Thus we can plug equation A.46 into A.44 to get an expression for the sheath potential profile $\phi(x_{\mathrm{CL}})$.

$$\phi(x_{\mathrm{CL}}) = -\left(\frac{81 \left(\alpha_{\mathrm{ps}} n_{\mathrm{p}} e \sqrt{\frac{eT_{\mathrm{e}}}{m_{\mathrm{i}}}} \right)^2 m_{\mathrm{i}}}{32 {\epsilon_0}^2 e} \right)^{\frac{1}{3}} x_{\mathrm{CL}}^{\frac{4}{3}} \tag{A.47}$$

$$\phi(x_{\mathrm{CL}}) = -\left(\frac{81}{32}\right)^{\frac{1}{3}} {\alpha_{\mathrm{ps}}}^{\frac{2}{3}} \left(\frac{n_{\mathrm{p}}^2 e^2 T_{\mathrm{e}}}{{\epsilon_0}^2} \right)^{\frac{1}{3}} {x_{\mathrm{CL}}}^{\frac{4}{3}} \tag{A.48}$$

Introducing non-dimensionalizations for potential and distance,

$$\frac{\phi(x_{\mathrm{CL}})}{T_{\mathrm{e}}} = -\left(\frac{81}{32}\right)^{\frac{1}{3}} {\alpha_{\mathrm{ps}}}^{\frac{2}{3}} \left(\frac{n_{\mathrm{p}} e}{\epsilon_0 T_{\mathrm{e}}} \right)^{\frac{2}{3}} {x_{\mathrm{CL}}}^{\frac{4}{3}} \tag{A.49}$$

$$\frac{\phi(x_{\mathrm{CL}})}{T_{\mathrm{e}}} = -\left(\frac{81}{32}\right)^{\frac{1}{3}} {\alpha_{\mathrm{ps}}}^{\frac{2}{3}} \left(\frac{x_{\mathrm{CL}}}{\lambda_{\mathrm{d}}} \right)^{\frac{4}{3}} \tag{A.50}$$

$$\Phi(\xi_{\mathrm{CL}}) = \left(\frac{81}{32}\right)^{\frac{1}{3}} {\alpha_{\mathrm{ps}}}^{\frac{2}{3}} {\xi_{\mathrm{CL}}}^{\frac{4}{3}} \tag{A.51}$$

This gives the result that the sheath potential scales with the 4/3 power of the sheath thickness and depends on the value of α_{ps} used in specifying the plasma density at the sheath edge. We can encapsulate the terms in constants such that

$$\Phi = \mathrm{C}_1 {\xi_{\mathrm{CL}}}^{\frac{4}{3}} \tag{A.52}$$

$$\xi_{\mathrm{CL}} = \mathrm{C}_2 \Phi^{\frac{3}{4}} \tag{A.53}$$

Table **??** shows the relation between choice of α_{ps} and the constants in equations A.52 and A.53. For the collisionless presheath result of $\alpha_{\mathrm{ps}} = \exp(-1/2)$, the constants are close to unity, so one can even use the 4/3 power relationship directly and expect to achieve reasonable accuracy, *i.e.*,

$$\Phi \approx {\xi_{\mathrm{CL}}}^{\frac{4}{3}} \tag{A.54}$$

Table A.1: Relation between fractional reduction in plasma density across the presheath $\alpha_{\rm ps}$ and the constants in equations A.52 and A.53.

$\alpha_{\rm ps}$	C_1	C_2
1.0	1.362	0.793
0.9	1.270	0.836
0.8	1.174	0.886
0.7	1.074	0.948
$\exp(-1/2)$	0.977	1.018
0.6	0.969	1.024
0.5	0.858	1.121
0.4	0.740	1.254
0.3	0.611	1.447

APPENDIX B

MAGNETIC FIELD EXPERIMENTS

One of the most interesting areas for future work in plasma-wall interactions is in investigating the effect of applied magnetic field on the plasma sheath and plasma-wall interaction. As discussed in Section 2.4, theoretical models particular to the sheath have been done by Chodura [22] and Ahedo [4]. The Chodura model is notable for the description of the magnetic presheath, and the Ahedo model extends the description to include effects of neutral collisions and strong magnetic field.

The experiment by Kim *et al.* [51] observes magnetic presheaths in agreement with the principal conclusions of the Chodura model. The Kim experiment uses a multidipole plasma device similar to the one used in this work but with some differences. The device constitutes its own vacuum vessel, and the magnetic fields used to effect the sheaths are applied via large external magnets. Having the magnetic coils external to the vacuum is advantageous in that they can be readily air- or water-cooled, but they also require high current to attain significant field strength in the experimental volume. The Kim experiment did not investigate the strong magnetic field regime of the Ahedo model (when the ion gyroradius is order of λ_{d}) – powerful magnets would be required to reach these conditions, as the fields required are moderate (around 500 G even for $n_{\mathrm{e}} = 10^{13}\mathrm{m}^{-3}$ argon plasma). In addition, the application of such a strong field across the normally-unmagnetized plasma device could necessitate additional considerations to maintain plasma uniformity.

Over the course of the current work, an experiment was conceived to investigate magnetized sheath and to also investigate the strong magnetic field regime of the Ahedo model. A schematic of the device is shown in Figure B.1. The idea is to have

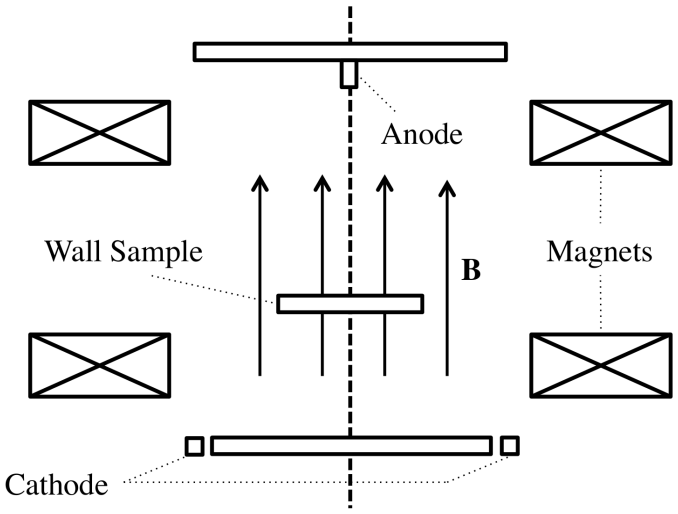

Figure B.1: Schematic of magnetic field experiment prototype.

effectively a Helmholtz coil with a circumferential cathode at one end, a central anode at the other end, limiter discs on both ends, and the sample to be tested in the center. A reduced size of Helmholtz coil would be used to enable sufficient magnetic fields to be achieved. A cross-field discharge would be established between the cathode and anode. Probe diagnostics could access the sheath region in front of the wall material sample, and the sample could be rotated to vary magnetic field incidence angle.

A prototype version of the experiment was assembled using solenoid magnets left over from another project. It was found that the discharge would not light at argon pressure (10^{-4} Torr) typical for operation of the multidipole plasma cell, both with magnets on and magnets off. Filament current was sufficient to drive a discharge current to the grounded vacuum chamber, but could not establish a current to the anode. Later, at higher argon pressure of order 1 Torr following regeneration of the cryopumps, a discharge was able to be lit between cathode and anode. Langmuir probe scans were taken with the planar Langmuir probe with the normal aligned with the magnetic field, but beyond observing a strange shape of the electron collection region no attempt was made to interpret them. Ion current magnitudes indicate that the plasma was perhaps an order of magnitude more dense than the standard 10 mA

plasma cell condition. Ultimately the experiment was ended by an arc between the

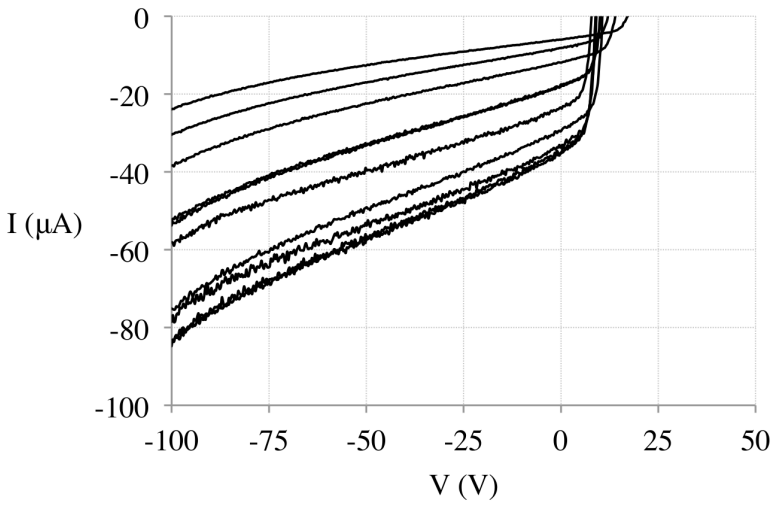

Figure B.2: Planar Langmuir probe I-V curves collected in 1 Torr discharge in prototype magnetic field experiment, ion current.

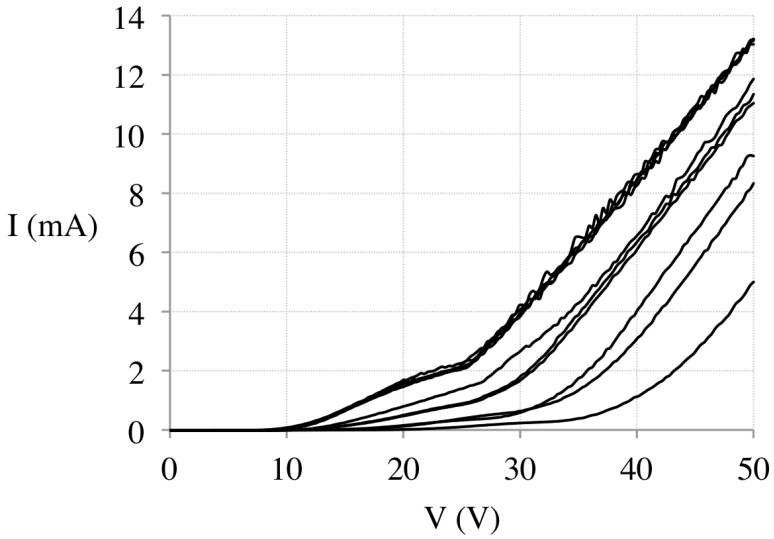

Figure B.3: Planar Langmuir probe I-V curves collected in 1 Torr discharge in prototype magnetic field experiment, electron current.

positive and negative sides of the tungsten filament serving as the thermionic cathode.

While no useful data was gained from this initial experiment, the concept is included here for the possible benefit of future investigations into this area. In hindsight, the author feels that even if a way is found to fix the current problems, the setup may be more complex and constricting then necessary. Fruitful results might be found by use

of an intrinsically magnetized plasma source such as a small mirror machine.

REFERENCES

[1] *IEPC Proc.*, no. IEPC-2003-258, (Toulouse, France), March 2003.

[2] "Solar arrays | nasa." `https://www.nasa.gov/mission_pages/station/structure/elements/solar_arrays.html#.VaLHIFzimEI`, 2013. Accessed: 2015-07-12.

[3] "Eutelsat 115 west b launched successfully into space." `http://news.eutelsat.com/pressreleases/eutelsat-115-west-b-launched-successfully-into-space-1123649`, March 2015. [Accessed 05-July-2015].

[4] Ahedo, E., "Structure of the plasma-wall interaction in an oblique magnetic field," *Physics of Plasmas*, vol. 4, p. 4419, 1997.

[5] Allen, J., "A note on the generalized sheath criterion," *Journal of Physics D: Applied Physics*, vol. 9, no. 16, p. 2331, 1976.

[6] Allen, J., "Probe theory-the orbital motion approach," *Physica Scripta*, vol. 45, no. 5, p. 497, 1992.

[7] Bachet, G., Chérigier, L., and Doveil, F., "Ion velocity distribution function observations in a multipolar argon discharge," *Physics of Plasmas*, vol. 2, p. 1782, 1995.

[8] Barnett, J. and Jahn, R., "Onset phenomena in mpd thrusters," 1985.

[9] Barral, S., Jayet, Y., Mazouffre, S., Dudeck, M., Veron, E., and others, "Hall effect thruster with an aln discharge channel," in *29th International Electric Propulsion Conference, IEPC-2005-152, Princeton, NJ*, 2005.

[10] Bauer, E., "Low energy electron microscopy," *Reports on Progress in Physics*, vol. 57, no. 9, p. 895, 1994.

[11] Benilov, M., "The child–langmuir law and analytical theory of collisionless to collision-dominated sheaths," *Plasma Sources Science and Technology*, vol. 18, no. 1, p. 014005, 2008.

[12] Böhm, D., "The characteristics of electrical discharges in magnetic fields." eds. A. Guthrie and RK Wakerling, McGraw-Hill, New York, 1949.

[13] Brieda, L., "Nonlinear poisson solver." `https://www.particleincell.com/2012/nonlinear-poisson-solver/`. Accessed: 2015-05-12.

[14] Brophy, J. R., Marcucci, M. G., Ganapathi, G. B., Garner, C. E., Henry, M. D., Nakazono, B., and Noon, D., "The ion propulsion system for dawn," *AIAA Paper*, vol. 4542, 2003.

[15] Brutscher, J., Günzel, R., and Möller, W., "Sheath dynamics in plasma immersion ion implantation," *Plasma Sources Science and Technology*, vol. 5, no. 1, p. 54, 1996.

[16] Byers, D. C. and Dankanich, J. W., "Geosynchronous-earth-orbit communication satellite deliveries with integrated electric propulsion," *Journal of Propulsion and Power*, vol. 24, no. 6, pp. 1369–1375, 2008.

[17] Callen, J., "Fundamentals of plasma physics." = http://homepages.cae.wisc.edu/ callen/. Accessed: 2015-06-08.

[18] Campanell, M., "Negative plasma potential relative to electron-emitting surfaces," *Physical Review E*, vol. 88, no. 3, p. 033103, 2013.

[19] Campanell, M., Khrabrov, A., and Kaganovich, I., "Absence of debye sheaths due to secondary electron emission," *Physical review letters*, vol. 108, no. 25, p. 255001, 2012.

[20] Campanell, M., Khrabrov, A., and Kaganovich, I., "General cause of sheath instability identified for low collisionality plasmas in devices with secondary electron emission," *Physical review letters*, vol. 108, no. 23, p. 235001, 2012.

[21] Child, C., "Discharge from hot cao," *Physical Review (Series I)*, vol. 32, no. 5, p. 492, 1911.

[22] Chodura, R., "Plasma–wall transition in an oblique magnetic field," *Physics of fluids*, vol. 25, p. 1628, 1982.

[23] Clark, S., "BoeingâĂŹs first two all-electric satellites ready for launch." `http://spaceflightnow.com/2015/03/01/boeings-first-two-all-electric-satellites-ready-for-launch/`, March 2015. [Accessed 05-July-2015].

[24] Coakley, P. G. and Hershkowitz, N., "Secondary electrons in a plasma-wall sheath," *Physics Letters A*, vol. 78, no. 2, pp. 145–148, 1980.

[25] Dawson, P., "Secondary electron emission yields of some ceramics," *Journal of Applied Physics*, vol. 37, no. 9, pp. 3644–3645, 1966.

[26] de Grys, K., Rayburn, C., and Haas, J., "Study of power loss mechanisms in the bpt-4000 hall thruster," in *39th AIAA/ASME/SAE/ASEE Joint Propulsion Conference and Exhibit*, p. 5277, 2003.

[27] Debye, P. and Hückel, E., "De la théorie des électrolytes. i. abaissement du point de congélation et phénomènes associés," *Physikalische Zeitschrift*, vol. 24, no. 9, pp. 185–206, 1923.

[28] Demidov, V., Ratynskaia, S., and Rypdal, K., "Electric probes for plasmas: The link between theory and instrument," *Review of scientific instruments*, vol. 73, no. 10, pp. 3409–3439, 2002.

[29] Encarnacion, P. A., *Electron field emission from boron nitride thin films*. ProQuest, 2008.

[30] Enos, G., Pugmire, T., and Shaw, R., "Applied resistojet technology," *Journal of Spacecraft and Rockets*, vol. 8, no. 1, pp. 63–68, 1971.

[31] Fife, J. M., "Hybrid-pic modeling and electrostatic probe survey of hall thrusters," 1999.

[32] Florenz, R. E., Hall, S. J., Gallimore, A. D., Kamhawi, H., Griffiths, C. M., Brown, D. L., Hofer, R. R., and Polk, J. E., "First firing of a 100-kw nested-channel hall thruster," tech. rep., DTIC Document, 2013.

[33] Franklin, R., "The plasma–sheath boundary region," *Journal of Physics D: Applied Physics*, vol. 36, no. 22, p. R309, 2003.

[34] Franklin, R. and Han, W., "Simple way to determine the edge of an electron-free sheath with an emissive probe," *Plasma Phys. Control. Fusion*, vol. 30, no. 6, pp. 771–771, 1988.

[35] Furman, M. and Pivi, M., "Probabilistic model for the simulation of secondary electron emission," *Physical Review Special Topics-Accelerators and Beams*, vol. 5, no. 12, p. 124404, 2002.

[36] Fursey, G. N., *Field emission in vacuum microelectronics*. Springer Science & Business Media, 2007.

[37] Goebel, D. M. and Katz, I., *Fundamentals of electric propulsion: ion and Hall thrusters*, vol. 1. John Wiley & Sons, 2008.

[38] Goeckner, M., Goree, J., and Sheridan, T., "Measurements of ion velocity and density in the plasma sheath," *Physics of Fluids B: Plasma Physics*, vol. 4, p. 1663, 1992.

[39] Henry, C., "Snecma receives follow-on contract from airbus for all-electric thrusters." `http://www.satellitetoday.com/technology/2015/03/25/snecma-receives-follow-on-contract-from-airbus-for-all-electric-thrusters/`, March 2015. [Accessed 05-July-2015].

[40] Hershkowitz, N., "How langmuir probes work," *Plasma Diagnostics: Discharge Parameters and Chemistry*, vol. 1, p. 113, 2013.

[41] Hershkowitz, N., DeKock, J. R., Coakley, P., and Cartier, S. L., "Surface trapping of primary electrons by multidipole magnetic fields," *Review of Scientific Instruments*, vol. 51, no. 1, pp. 64–69, 1980.

[42] Hobbs, G. and Wesson, J., "Heat flow through a langmuir sheath in the presence of electron emission," *Plasma Physics*, vol. 9, no. 1, p. 85, 1967.

[43] Hofer, R. R., Goebel, D. M., Mikellides, I. G., and Katz, I., "Magnetic shielding of a laboratory hall thruster. ii. experiments," *Journal of Applied Physics*, vol. 115, no. 4, p. 043304, 2014.

[44] Hofer, R. R., Katz, I., Mikellides, I. G., Goebel, D. M., Jameson, K. K., Sullivan, R. M., and Johnson, L. K., "Efficacy of electron mobility models in hybrid-pic hall thruster simulations," *AIAA Paper*, vol. 4924, p. 2008, 2008.

[45] Hofer, R. R., Mikellides, I. G., Katz, I., and Goebel, D. M., "Wall sheath and electron mobility modeling in hybrid-pic hall thruster simulations," *AIAA Paper*, vol. 5267, p. 2007, 2007.

[46] Hubble, A., Barnat, E., Weatherford, B., and Foster, J., "The electron spatial distribution and leak width in a magnetic cusp," *Plasma Sources Science and Technology*, vol. 23, no. 2, pp. 22001–22006, 2014.

[47] Intrator, T., Cho, M.-H., Wang, E. Y., Hershkowitz, N., Diebold, D., and DeKock, J., "The virtual cathode as a transient double sheath," *Journal of applied physics*, vol. 64, no. 6, pp. 2927–2933, 1988.

[48] Jahn, R. G., "Electric propulsion," *American Scientist*, pp. 207–217, 1964.

[49] Jamison, S., Shen, J., Jones, D., Issac, R., Ersfeld, B., Clark, D., and Jaroszynski, D., "Plasma characterization with terahertz time–domain measurements," *Journal of applied physics*, vol. 93, no. 7, pp. 4334–4336, 2003.

[50] Kathuria, S. and Kalra, G., "Two-stream instability in a collisionless plasma," *Astrophysics and Space Science*, vol. 24, no. 1, pp. 133–143, 1973.

[51] Kim, G.-H., Hershkowitz, N., Diebold, D., and Cho, M.-H., "Magnetic and collisional effects on presheaths," *Physics of Plasmas*, vol. 2, p. 3222, 1995.

[52] Kim, V., Kozlov, V., Skrylnikov, A., Veselovzorov, A., Fife, J. M., and Locke, S., *Investigation of operation and characteristics of small SPT with discharge chamber walls made of different ceramics*. Defense Technical Information Center, 2003.

[53] Knappmiller, S., Robertson, S., and Sternovsky, Z., "Method to find the electron distribution function from cylindrical probe data," *Physical Review E*, vol. 73, no. 6, p. 066402, 2006.

[54] Koch, D. and Hitchon, W., "The effects of collisions on the plasma presheath," *Physics of Fluids B: Plasma Physics (1989-1993)*, vol. 1, no. 11, pp. 2239–2243, 1989.

[55] Lang, A. and Hershkowitz, N., "Multidipole plasma density," *Journal of Applied Physics*, vol. 49, no. 9, pp. 4707–4710, 1978.

[56] LaPointe, M. R., Strzempkowski, E., and Pencil, E., "High power mpd thruster performance measurements," *AIAA Paper*, vol. 3467, p. 2004, 2004.

[57] Lawless, J. and SUBRAMANIAM, V., "Theory of onset in magnetoplasmadynamic thrusters," *Journal of Propulsion and Power*, vol. 3, no. 2, pp. 121–127, 1987.

[58] Lee, D., Hershkowitz, N., and Severn, G. D., "Measurements of ar+ and xe+ velocities near the sheath boundary of ar–xe plasma using two diode lasers," *Applied Physics Letters*, vol. 91, no. 4, pp. 041505–041505, 2007.

[59] Lee, D., Severn, G., Oksuz, L., and Hershkowitz, N., "Laser-induced fluorescence measurements of argon ion velocities near the sheath boundary of an argon–xenon plasma," *Journal of Physics D: Applied Physics*, vol. 39, no. 24, p. 5230, 2006.

[60] Leung, K., Hershkowitz, N., and MacKenzie, K., "Plasma confinement by localized cusps," *Physics of Fluids (1958-1988)*, vol. 19, no. 7, pp. 1045–1053, 1976.

[61] Leung, K., Samec, T., and Lamm, A., "Optimization of permanent magnet plasma confinement," *Physics Letters A*, vol. 51, no. 8, pp. 490–492, 1975.

[62] Leung, K., Taylor, G., Barrick, J., Paul, S., and Kribel, R., "Plasma confinement by permanent magnet boundaries," *Physics Letters A*, vol. 57, no. 2, pp. 145–147, 1976.

[63] Li, W., Ma, J., Li, J.-j., Zheng, Y.-b., and Tan, M.-s., "Measurement of virtual cathode structures in a plasma sheath caused by secondary electrons," *Physics of Plasmas*, vol. 19, p. 030704, 2012.

[64] Lichon, P. G. and Sankovic, J. M., "Development and demonstration of a 600-second mission-average i (sp) arcjet," *Journal of Propulsion and Power*, vol. 12, no. 6, pp. 1018–1025, 1996.

[65] Limpaecher, R. and MacKenzie, K., "Magnetic multipole containment of large uniform collisionless quiescent plasmas," *Review of Scientific Instruments*, vol. 44, no. 6, pp. 726–731, 1973.

[66] Manzella, D. and Hack, K., "High-power solar electric propulsion for future nasa missions," AIAA-2014-3718, 50th AIAA/ASME/SAE/ASEE Joint Propulsion Conference, Cleveland, OH, 2014.

[67] Martinez, R. A., Dao, H., and Walker, M. L., "Power deposition into the discharge channel of a hall effect thruster," *Journal of Propulsion and Power*, vol. 30, no. 1, pp. 209–220, 2013.

[68] Mazouffre, S., Echegut, P., and Dudeck, M., "A calibrated infrared imaging study on the steady state thermal behaviour of hall effect thrusters," *Plasma Sources Science and Technology*, vol. 16, no. 1, p. 13, 2007.

[69] Morozov, A. and Savel'Ev, V., "Theory of the near-wall conductivity," *Plasma Physics Reports*, vol. 27, no. 7, pp. 570–575, 2001.

[70] Mott-Smith, H. M. and Langmuir, I., "The theory of collectors in gaseous discharges," *Physical review*, vol. 28, no. 4, p. 727, 1926.

[71] Neumann, G., Bänziger, U., Kammeyer, M., and Lange, M., "Plasma-density measurements by microwave interferometry and langmuir probes in an rf discharge," *Review of scientific instruments*, vol. 64, no. 1, pp. 19–25, 1993.

[72] Oksuz, L. and Hershkowitz, N., "Plasma, presheath, collisional sheath and collisionless sheath potential profiles in weakly ionized, weakly collisional plasma," *Plasma Sources Science and Technology*, vol. 14, no. 1, p. 201, 2005.

[73] Oksuz, L. and Hershkowitz, N., "First experimental measurements of the plasma potential throughout the presheath and sheath at a boundary in a weakly collisional plasma," *Physical review letters*, vol. 89, no. 14, p. 145001, 2002.

[74] Parra, F., Ahedo, E., Fife, J., and Martinez-Sanchez, M., "A two-dimensional hybrid model of the hall thruster discharge," *Journal of Applied Physics*, vol. 100, no. 2, p. 023304, 2006.

[75] Polk, J., Kakuda, R., Anderson, J., Brophy, J., Rawlin, V., Patterson, M., Sovey, J., and Hamley, J., "Validation of the nstar ion propulsion system on the deep space one mission: overview and initial results," *AIAA paper*, vol. 99, p. 2274, 1999.

[76] Porsbjer, J., "Northern lights 02." Wikimedia Commons CCL 3.0, `https://en.wikipedia.org/wiki/File:Northern_Lights_02.jpg`, 2010. Accessed: 2015-07-08.

[77] Raitses, Y., Kaganovich, I. D., Khrabrov, A., Sydorenko, D., Fisch, N. J., and Smolyakov, A., "Effect of secondary electron emission on electron cross-field current in discharges," *Plasma Science, IEEE Transactions on*, vol. 39, no. 4, pp. 995–1006, 2011.

[78] Riemann, K.-U., "Bohm criterion and ion-acoustic sound barrier," *Physics of Fluids B: Plasma Physics*, vol. 3, p. 3331, 1991.

[79] Riemann, K.-U., "The bohm criterion and sheath formation," *Journal of Physics D: Applied Physics*, vol. 24, no. 4, p. 493, 2000.

[80] Rizopoulou, N., Robinson, A., Coppins, M., and Bacharis, M., "Electron emission in a source-collector sheath system: A kinetic study," *Physics of Plasmas (1994-present)*, vol. 21, no. 10, p. 103507, 2014.

[81] Schwager, L. A. and Birdsall, C. K., "Collector and source sheaths of a finite ion temperature plasma," *Physics of Fluids B: Plasma Physics (1989-1993)*, vol. 2, no. 5, pp. 1057–1068, 1990.

[82] Schweigert, I., Langendorf, S., Walker, M., and Keidar, M., "Sheath structure transition controlled by secondary electron emission," *Plasma Sources Science and Technology*, vol. 24, no. 2, p. 025012, 2015.

[83] Severn, G., Wang, X., Ko, E., and Hershkowitz, N., "Experimental studies of the bohm criterion in a two-ion-species plasma using laser-induced fluorescence," *Physical review letters*, vol. 90, no. 14, p. 145001, 2003.

[84] Severn, G., Wang, X., Ko, E., Hershkowitz, N., Turner, M., and McWilliams, R., "Ion flow and sheath physics studies in multiple ion species plasmas using diode laser based laser-induced fluorescence," *Thin solid films*, vol. 506, pp. 674–678, 2006.

[85] Sheehan, J. P. Ph.D. thesis, University of Wisconsin-Madison, 2012.

[86] Sheehan, J. and Hershkowitz, N., "Emissive probes," *Plasma Sources Science and Technology*, vol. 20, no. 6, p. 063001, 2011.

[87] Sheehan, J., Kaganovich, I., Wang, H., Sydorenko, D., Raitses, Y., and Hershkowitz, N., "Effects of emitted electron temperature on the plasma sheath," *Physics of Plasmas (1994-present)*, vol. 21, no. 6, p. 063502, 2014.

[88] Shih, A., Yater, J., Hor, C., and Abrams, R., "Secondary electron emission studies," *Applied surface science*, vol. 111, pp. 251–258, 1997.

[89] Sydorenko, D., Kaganovich, I., Raitses, Y., and Smolyakov, A., "Breakdown of a space charge limited regime of a sheath in a weakly collisional plasma bounded by walls with secondary electron emission," *Physical review letters*, vol. 103, no. 14, p. 145004, 2009.

[90] Takamura, S., Mizoshita, S., and Ohno, N., "Suppression of secondary electron emission from the material surfaces with grazing incident magnetic field in the plasma," 1996.

[91] Takamura, S., "Sheath formation in a plasma with energetic electrons," *Physics Letters A*, vol. 133, no. 6, pp. 312–314, 1988.

[92] Takamura, S., Ye, M., Kuwabara, T., and Ohno, N., "Heat flows through plasma sheaths," *physics of plasmas*, vol. 5, p. 2151, 1998.

[93] Teitel, A., "Solar electric propulsion could slash the price of manned missions." http://www.americaspace.com/?p=23446, 2012. Accessed: 2015-08-11.

[94] Tilford, C. R., "Sensitivity of hot cathode ionization gages," *Journal of Vacuum Science & Technology A*, vol. 3, no. 3, pp. 546–550, 1985.

[95] Tondu, T., Belhaj, M., and Inguimbert, V., "Electron-emission yield under electron impact of ceramics used as channel materials in hall-effect thrusters," *Journal of Applied Physics*, vol. 110, no. 9, p. 093301, 2011.

[96] Van Gessel, A., Carbone, E., Bruggeman, P., and Van der Mullen, J., "Laser scattering on an atmospheric pressure plasma jet: disentangling rayleigh, raman and thomson scattering," *Plasma Sources Science and Technology*, vol. 21, no. 1, p. 015003, 2012.

[97] Vaughan, J. R. M., "A new formula for secondary emission yield," *Electron Devices, IEEE Transactions on*, vol. 36, no. 9, pp. 1963–1967, 1989.

[98] Viel-Inguimbert, V. and others, "Secondary electron emission of ceramics used in the channel of spt," in *28th International Electric Propulsion Conference, Toulouse, France*, 2003.

[99] Walker, M. L. R., *Effects of facility backpressure on the performance and plume of a Hall thruster*. PhD thesis, University of Michigan, 2005.

[100] Wilbur, P. J., Rawlin, V. K., and Beattie, J., "Ion thruster development trends and status in the united states," *Journal of Propulsion and Power*, vol. 14, no. 5, pp. 708–715, 1998.

[101] Xu, K. G., *Ion Collimation and In-Channel Potential Shaping Using In-Channel Electrodes for Hall Effect Thrusters*. PhD thesis, Georgia Institute of Technology, 2012.

[102] Ye, M., Masuzaki, S., Shiraishi, K., Takamura, S., and Ohno, N., "Nonlinear interactions between high heat flux plasma and electron-emissive hot material surface," *Physics of Plasmas (1994-present)*, vol. 3, no. 1, pp. 281–292, 1996.

[103] Yendler, B., "Satellite rescue-luck or skillful application of technology," in *AIAA SPACE 2012 Conference & Exposition*, p. 5287, 2012.

[104] Zhurin, V., Kaufman, H., and Robinson, R., "Physics of closed drift thrusters," *Plasma Sources Science and Technology*, vol. 8, no. 1, p. R1, 1999.